A model-based investigation of transport pathways of thermocline waters to the ocean surface, with a focus on tropical oxygen minimum zones.

Dissertation
zur Erlangung des Doktorgrades
der Mathematisch-Naturwissenschaftlichen Fakultät
der Christian-Albrechts-Universität
zu Kiel

vorgelegt von
Mirjam Sophia Gleßmer

Kiel
2010

Referent: Prof. Dr. Andreas Oschlies

Korreferent: Prof. Dr. Carsten Eden

Tag der mündlichen Prüfung: 01.06.2010

Zum Druck genehmigt: 01.06.2001

gez. Prof. Dr. Lutz Kipp, Dekan

Die Entdeckung, dass es so einfach nicht ist, wie man gedacht hat, ist als Gewinn anzusehen.

- C.F. von Weizsäcker

Contents

Zusammenfassung **v**

Summary **vii**

1 Introduction **1**

1.1 Motivation 1
1.2 Changing climate in the Anthropocene 2
1.3 Climate change on geological timescales 6
1.4 Mechanisms involved in climate change 9
  1.4.1 Shutdown of the meridional overturning circulation 9
  1.4.2 Solubility pump 12
  1.4.3 Biological pump 13
  1.4.4 Carbonate chemistry 14
  1.4.5 Feedback mechanisms 15
1.5 Oxygen as switch for marine biogeochemistry 16
  1.5.1 Circulation in the tropical-subtropical oceans 19
1.6 Predicting the future 24
  1.6.1 Models 24
  1.6.2 Small scale processes in the real ocean 25
  1.6.3 Small scale processes in models 26
1.7 Introduction to the main chapters 27

2 Upper-ocean impacts of double-diffusive mixing **31**

2.1 Abstract 31
2.2 Introduction 32
2.3 Methods 33
  2.3.1 Model 33
  2.3.2 Double diffusion as function of the density ratio 35

2.3.3 Parameterizations 36
2.4 Model validation at the NATRE site 39
2.5 Results and discussion 41
2.5.1 Physics 41
2.5.2 Primary production and nutrient supply 46
2.5.3 Surface fluxes of CO_2 and O_2 48
2.6 Summary 52
2.7 Appendix: parameterizations of double-diffusive mixing 54
2.7.1 Parameterization LMD94 of double-diffusive mixing 54
2.7.2 Parameterization ZSH98 of double-diffusive mixing 55
2.8 Acknowledgments 57

3 Oxygen minimum zone and upwelling off Mauritania 59
3.1 Abstract 59
3.2 Introduction 60
3.3 Model and methods 62
3.3.1 Ocean general circulation model 62
3.3.2 Trajectory calculations 63
3.3.3 Tracer release experiments 63
3.3.4 Definition of regions 64
3.3.5 Comparison with observations 65
3.3.6 Upwelling transport, annual cycle and Ekman estimates . . . 67
3.4 Results 67
3.4.1 Pathways into the upwelling 67
3.4.2 Oxygen minimum zone 70
3.5 Conclusions 74
3.6 Acknowledgments 75

4 Atlantic and Pacific OMZs in models with different resolutions 77
4.1 Abstract 77
4.2 Motivation 78
4.3 Models and Methods 85
4.3.1 Models 86
4.3.2 Trajectory calculations 87
4.3.3 Tracer release experiments 89
4.3.4 How to define “the OMZ” 92

4.4 Results and discussion 94
4.4.1 On different forcing strategies 94
4.4.2 Comparison of ORCA025 and ORCA2 in the Atlantic 97
4.4.3 Comparison with the Pacific 109
4.4.4 Connection under doubling atmospheric CO_2 concentration . 114
4.5 Summary and conclusions 115
4.6 Appendix 118
4.6.1 Overview over float and tracer runs, and naming convention 118
4.6.2 Why are we not using quantitative ARIANE runs? 124
4.6.3 Figures 125
4.7 Acknowledgments 127

5 Conclusions and outlook **129**

Author contributions **135**

List of Figures **137**

List of Tables **139**

Bibliography **141**

Zusammenfassung

Numerische Ozeanmodelle sind ein Hilfsmittel, um ozeanische Prozesse und deren Wechselwirkungen mit Biogeochemie oder der Atmosphäre auf verschiedenen räumlichen und zeitlichen Skalen zu verstehen. Klimavorhersagen werden als Grundlage und als Begründung dafür verwendet, internationale Abkommen mit weitreichenden Konsequenzen für das Wohlergehen aller Menschen zu treffen. Aber Modelle, mit deren Hilfe diese Klimavorhersagen erstellt werden, beinhalten Annahmen und Ungenauigkeiten und sind daher nicht perfekt. Ziel dieser Arbeit ist es, zum Verständnis beizutragen, wie sensibel Ozeanmodelle auf die Details der Darstellung von Vermischungsprozessen und horizontaler Modellgitterauflösung reagieren, und Möglichkeiten aufzuzeigen, wie die Interpretation dieser Modelle verbessert werden kann.

Im ersten Teil dieser Arbeit wird der Einfluss der Darstellung eines bestimmten Vermischungsprozesses, der Doppeldiffusion, auf die physikalischen und biogeochemischen Eigenschaften des oberen Ozeans untersucht. Zwei Modell-Läufe, in denen Doppeldiffusion implementiert wurde, werden mit einem Standard-Lauf, der keine Doppeldiffusion enthält, verglichen. Dabei zeigt sich, dass die Einbeziehung von Doppeldiffusion die physikalischen und noch stärker die biogeochemischen Eigenschaften des oberen Ozeans verändert. Diese Veränderungen sind jedoch klein, verglichen mit den Messungenauigkeiten der Größen, gegen die die Modell-Ergebnisse verglichen werden. Die zusätzliche CO_2-Aufnahme der doppeldiffusiven Läufe entspricht ca. 7 % des anthropogenen CO_2-Signals. Obwohl nicht mit Bestimmtheit entschieden werden kann, welche der beiden Darstellungen gegebenenfalls angemessener ist, zeigt sich deutlich, dass Doppeldiffusion und deren Umsetzung in Modellen weiter untersucht werden muss.

Im zweiten und dritten Teil der Arbeit wird die Verbindung zwischen tropischen Sauerstoffminimumzonen und dem oberen Ozean untersucht. Ozeanische Sauerstoffminimumzonen sind wichtig im Kontext von Klima und Stickstoffkreislauf, weil in Sauerstoffminimumzonen viele Prozesse anders ablaufen als im Rest des Ozeans. Die Zeit, die Wasser für den Weg aus den Sauerstoffminimumzonen zum oberen Ozean braucht, bestimmt die untere Grenze der Zeitskala, auf der Rückkopplungen stattfinden können. Die Regionen, in denen das Wasser aus den Sauerstoffminimumzonen den oberen Ozean erreicht, sind die Regionen, in denen die Rückkopplungen dann stattfinden. Mit Hilfe von simulierten Float- und Tracer-Experimenten in Modellen mit horizontaler Gitterauflösung zwischen 1/12° und 2° wird gezeigt, dass Wasser aus den Sauerstoffminimumzonen den oberen Ozean in den äquatorialen und Küstenauftriebsgebieten erreicht. Im hochauflösenden Modell sind diffusive Prozesse für etwa die Hälfte des Transports verantwortlich, während die Ergebnisse des grobauflösenden Modells vor allem durch advektive Prozesse bestimmt werden. Dabei sind die räumlichen Verteilungen weitgehend unabhängig vom verwendeten Modell. Die Verbindung zwischen Sauerstoffminimumzonen und dem oberen Ozean ist im Pazifik schneller als im Atlantik, was darauf hindeutet, dass die Intensität der Sauerstoffminimumzonen hauptsächlich von anderen Prozessen als von der Ventilation abhängt. In einem “global warming”-Szenario schwächt sich die Verbindung ab.

Die Ergebnisse dieser Arbeit tragen dazu bei, den Einfluss bestimmter Modell-Konfigurationen auf die Simulationsergebnisse zu verstehen. Es werden Vorschläge gemacht, wie zukünftige Simulationen verbessert werden können.

Summary

Numerical models are a tool to better understand oceanic processes and their interaction with the atmosphere and biogeochemical processes on different temporal and spatial scales. Model predictions of future climate under different scenarios are used to formulate international protocols with far-reaching consequences for the well-being of the world's population. However, models used to produce those predictions are not perfect. This thesis aims to contribute to the understanding of how sensitive ocean models are to the representation of a small scale mixing process and to horizontal grid resolution, and how their performance could be improved.

In the first part of this thesis, the influence of the model representation of double-diffusive mixing on physical and biogeochemical upper-ocean properties is investigated. Two model runs in which double-diffusive mixing was parameterized in different ways are compared with a standard run which does not account for this process. Implementing double diffusion leads to changes in simulated physical, and even more in biogeochemical, upper-ocean properties. Changes in for example primary production are of the same order of magnitude as uncertainties in the measurements against which the model results can be compared. CO_2 uptake is enhanced by approximately $7\,\%$ of the anthropogenic CO_2 signal. Although no definite conclusion on which representation, if any, is better could be drawn, the importance of further investigating double-diffusive mixing and its implementation in models became evident.

In the second and third part, the closeness of the connection between tropical oxygen minimum zones and the surface ocean is investigated. Oceanic oxygen minimum zones are important in the context of climate and the nitrogen cycle, because they allow for very different processes than the rest of the ocean. The time it takes for water to be transported from the oxygen minimum zones to the surface ocean determines the minimum timescale of potential feedback processes. In the area where the oxygen minimum zone waters reach the mixed layer, feedback processes are likely to happen. Using float and tracer release experiments in models with horizontal resolution ranging from 1/12° to 2°, it is shown that oxygen minimum zone waters reach the surface ocean in the equatorial and coastal upwelling regions. In the high resolution model diffusive processes contribute to about half of the total transport, whereas the low resolution results are dominated by advection. Spatial distributions are largely independent of model and method used. The connection between the oxygen minimum zones and the upper ocean is faster in the Pacific than in the Atlantic Ocean, indicating that the intensity of oxygen minimum zones depends mainly on other processes than ventilation. Under a global warming scenario the connection is found to weaken, suggesting a strengthening of the oxygen minima.

Findings from this thesis contribute to understanding the impact of specific model features on the resulting simulations and give suggestions on how to improve future simulations.

Chapter 1

Introduction

1.1 Motivation

Strong changes in the climate system have been observed over the last approximately 100 years, which are attributed to the changes in radiative balance of the earth (Mitchell [1989]). Consensus has been reached over the last decades that changes in the atmospheric composition, especially an increase in greenhouse gas concentrations, have caused the observed climate change (IPCC [2007b]). Atmospheric concentrations of carbon dioxide, methane and nitrous oxide, are primarily caused by fossil fuel burning and land-use practices, and the magnitudes of their absolute change as well as their rate of change are unprecedented in the last 650 kyr[1], and arguably even 800 kyr. Concentrations of these greenhouse gases and temperature co-vary over the last 650 kyr, indicating a close relationship of the greenhouse gases with temperature. Carbon and nitrogen are elements whose biogeochemical cycles constitute greenhouse gases. Biogeochemical cycles are a composit of biological and/or chemical reactions and physical transport processes, and determine the distribution of substances in space and time. The direct influence of those cycles on climate is restricted to the concentration of greenhouse gases in the surface ocean, which are subject to exchange with the atmosphere. Indirectly, biogeochemical cycles are climate relevant because sources and sinks vary in strength. Both, the spatial distribution and the strength of sources and sinks can be influenced by climate change. For example changing oxygen concentrations can act as a switch on marine biogeochemistry. Oxygen concentrations below certain thresholds change chemical and microbial processes which affect nutrient cycling, biological produc-

---

[1] 1 kyr = 1000 years

tivity and hence marine life in the global ocean. In order to understand the system, all reactions and redistributing processes must be known. They can be investigated by measuring various parameters in situ or in laboratory experiments, and their complex interactions can be deduced with the help of numerical models.

In order to improve models of the climate system, this thesis concentrates on understanding artificial/spurious effects in ocean models, for example how model grid resolution or parameterizations of mixing processes influence the results. It is crucial to understand small-scale processes which cause mixing, and to implement them correctly in numerical models of the ocean and the atmosphere, as predictions of such models are used to formulate international protocols, intended to mitigate the severity of climate change and its impacts (Williams [2005]). In the following, a general introduction to the subject is given. First, climate change over the last approximately 100 years is presented and then set in the larger context of the last 650 kyr. Then, in Section 1.4, an overview over important processes and interactions is given. After that, the role of oxygen for biogeochemical processes is sketched in Section 1.5. Then, focussing on the ocean, in Section 1.6 technical aspects of simulating climate are described. This is followed by Section 1.7 with introductions to the three main chapters of this thesis, each proposing a small step to help predict the state and role of the ocean in changing climate.

1.2 Changing climate in the Anthropocene

On geological timescales, the most recent period in Earth's history is the Anthropocene. It spans the time between the late 18th century, when activities of humans first began to significantly and globally impact the Earth's climate and ecosystem, until today. Over this period, numerous changes in climate have been observed on regional, continental, and ocean basin scales. For example, arctic temperatures have risen and as a result arctic sea ice extent has receded. Mid- and high-latitude ocean salinity has become decreased, while in lower latitude oceans it has increased, suggesting changes in the evaporation and precipitation pattern. Aspects of extreme weather have become more extreme: more intense and longer droughts have been observed, heavy precipitation events have become more frequent over land. Cold days, cold nights and frosts have become less frequent while hot days, hot nights and heat waves have increased in frequency. Mid-latitude westerly winds have intensified since the 1960s in both hemispheres, indicating dynamical changes of atmospheric circulation.

Changes in the atmospheric abundance of greenhouse gases and aerosols, in solar radiation and in land surface properties alter the energy balance of the climate system. The global atmospheric concentrations of carbon dioxide, methane and nitrous oxide have increased markedly as a result of human activities since 1750, such as fossil fuel burning and land use changes, and now far exceed pre-industrial values determined from ice cores spanning many thousands of years (IPCC [2007b], see Figure 1.1).

In terms of contribution to the greenhouse effect, carbon dioxide is the most important anthropogenically influenced greenhouse gas. The atmospheric concentration of carbon dioxide has increased from a pre-industrial value of about 280 ppm[2] to 385 ppm in 2008 (Allison et al. [2009]), thereby exceeding by far the natural range over the last 650 kyr, which ranged from 180 ppm to 300 ppm as determined from ice cores, and potentially higher than at any time during the last 3-20 million years (Allison et al. [2009]). The second most important anthropogenic greenhouse gas is methane. Its atmospheric concentration has increased from a pre-industrial value of about 715 ppb[3] to 1800 ppb in 2009 (Allison et al. [2009]), also exceeding by far the natural range of the last 650 kyr (320 to 790 ppb). The concentration of the next most important greenhouse gas, nitrous oxide, increased from a pre-industrial value of about 270 ppb to 319 ppb in 2005. The increase of the atmospheric concentration of these greenhouse gases since the pre-industrial period is caused primarily by fossil fuel use combined with land-use change and agriculture (IPCC [2007b]). The combined radiative forcing due to increases in atmospheric concentrations of carbon dioxide, methane, and nitrous oxide is $+2.30\pm0.23$ W/m^2. Its rate of increase during the industrial era is very likely to have been unprecedented in more than 10 kyr. The carbon dioxide radiative forcing increased by 20 % from 1995 to 2005, the largest change for any decade in at least the last 200 yr.

Eleven of the twelve years from 1995 to 2006 fall among the twelve warmest years since 1850, when the instrumental record of global surface temperature started. The linear warming trend over the last 50 years ($+0.13\pm0.3$ K per decade) is nearly twice that observed over the last 100 years (see Figure 1.2). Observations since 1961 show that the ocean has been absorbing more than 80 % of the heat added to the climate system, leading to an increase of the global average ocean temperature

---

[2] ppm = parts per million = 10^{-6}

[3] ppb = parts per billion = 10^{-3} ppm = 10^{-9}

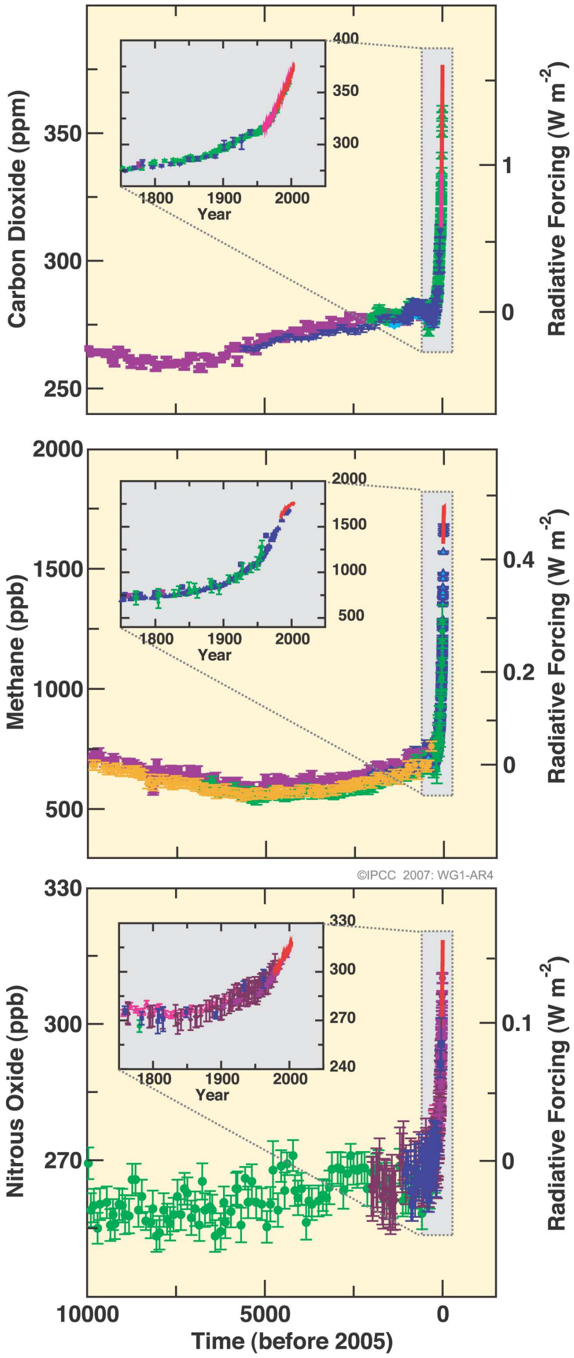

Figure 1.1: Atmospheric concentrations of carbon dioxide, methane and nitrous oxide over the last 10,000 years (large panels) and since 1750 (inset panels). Measurements are shown from ice cores (symbols with different colours represent different studies) and atmospheric samples (red lines). The corresponding radiative forcings are shown on the right hand axes of the large panels. Figure taken from IPCC [2007b], Figure SPM.1.

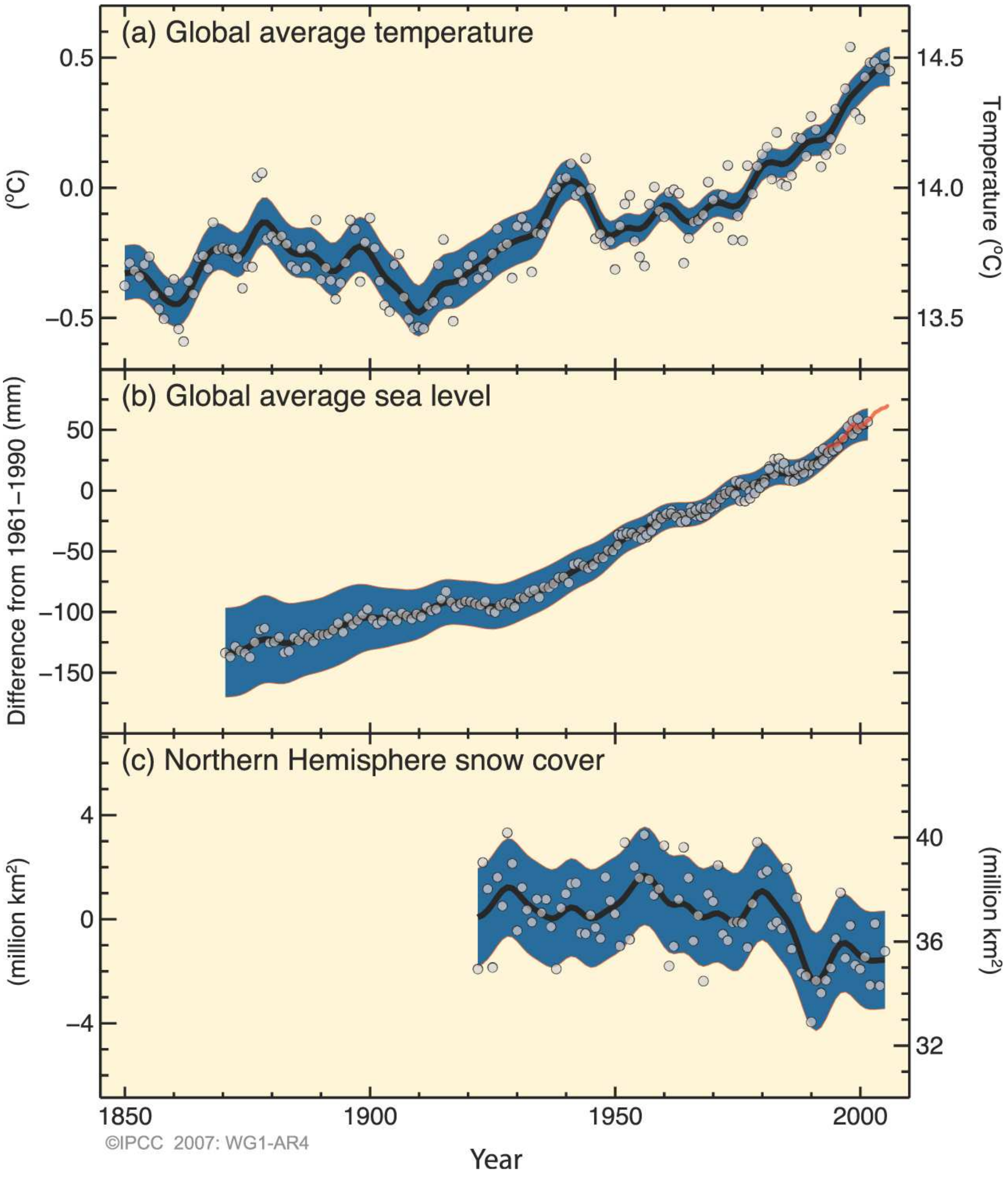

Figure 1.2: Observed changes in (a) global average surface temperature, (b) global average sea level from tide gauge (blue) and satellite (red) data and (c) Northern Hemisphere snow cover for March-April. All changes are relative to corresponding averages for the period 1961 – 1990. Smoothed curves (black) represent decadal average values while circles show yearly values. The shaded areas are the uncertainty intervals estimated from a comprehensive analysis of known uncertainties (a and b) and from the time series (c). Figure taken from IPCC [2007b], figure SPM.3.

down to depths of at least 3000 m, and global ocean surface temperature reached the warmest ever recorded for each of June, July and August 2009 (Allison et al. [2009]). The resulting thermal expansion of seawater contributes to sea-level rise, as does the widespread decrease in mountain glaciers and ice caps on both hemispheres as well as losses from the ice sheets of Greenland and Antarctica. Allison et al. [2009] suggest that sea-level rise until 2100 is likely to be at least twice as large as that presented by IPCC [2007b].

1.3 Climate change on geological timescales

Changes in the climate system of the same order of those occurring over the last approximately 100 years change the ecosystem and are a threat to the existence of many species of animals and plants. From paleo-records, past climate changes have been reconstructed, giving an insight into the order of magnitude of the impact changing climate can have. In the geological past, periods with very low oceanic oxygen concentrations have occurred, always linked to big changes in the oceanic nitrogen cycle (Jones and Jenkins [2001]) and consequently in the ecosystem.

Direct instrumental records of global temperature exist since approximately the 1850s, although longer records have been kept in some regions. The longest continuous measurement of atmospheric carbon dioxide concentration, the Keeling Curve measured at Mauna Loa, Hawaii, starts in 1958. So how do we know about temperatures, carbon dioxide concentrations, etc. before then?

Paleo-climatic data provides us with information about climatic conditions over interannual to millennial time scales in the past. Records of proxies, e.g. variables like isotope ratios which allow for the reconstruction of other, climate relevant, variables like ocean temperature and salinity, atmospheric composition and others can be reconstructed. Thus they can be used to help understand past climates and the mechanisms that led to large changes in the climate system.

Tree rings, corals, varved sediments, cave deposits and ice cores all show (if undisturbed) laminar growth, and therefore events can be dated back to individual years or even seasons. From individual layers that can be dated to a certain period, growth/population dynamics of plankton, insects, and trees for example can be related to properties like temperature and salinity, as can oxygen isotope ratios in coral/foraminiferal calcite shells or ratios of different elements. Past changes in global atmospheric composition are known from ice cores (650 kyr to present), where air trapped in the ice as well as the ice itself can be analyzed. Absolute age of rocks and other geological features can be obtained by radiometric dating, a technique based on a comparison between the observed abundance of a naturally occurring isotope and its decay products, using known decay rates. Several of these proxies combined increase security of the estimate and can help disentangle past climates and climate changes.

Some events that forced big changes in the climate system in the past are well known or can be reconstructed with great confidence. Time series of astronomically driven insolation changes due to eccentricity, axial tilt, and precession of the Earth's orbit, so-called Milankovitch cycles, are well known. Their quasi-periodicities agree well with climatic variations if feedback mechanisms described in Section 1.4 are accounted for. Past solar and volcanic eruptions can also be deduced from paleo-proxies. From recent volcanic eruptions (e.g. Mount Pinatubo in 1991), the effect of abrupt inputs of large amounts of carbon dioxide and aerosols into the atmosphere on global climate are well documented.

An example of the effects that climate change can have on the marine oxygen cycle and consequently on life on Earth is the end-Permian (251 Myr[4] ago), when the biggest mass extinction of the past 600 Myr occurred, killing up to 95 % of all species on Earth. As shown by Benton and Twitchett [2003], widespread benthic anoxic ocean conditions, coinciding with high temperatures and CO_2 levels, caused by either an asteroid impact or mass volcanism, can be deduced from paleo-records. They conclude that the melting of gas hydrates led to an ever-worsening positive-feedback loop, the "runaway greenhouse". There does not seem to be a scientific consensus on what prevented the runaway greenhouse from evaporating all greenhouse gases like on Venus, but one explanation might be albedo changes caused by volcanism, leading to cooling and stopping the feedback loop.

During the Cretaceous (145.5 - 65.5 Ma), series of oceanic anoxic events (OAE), covering whole ocean basins to the global ocean, have occurred. During those OAE, atmospheric CO_2 levels were much higher and the climate much warmer than at the intermediate stages.

In the Quaternary (2.6 Ma to present), the nitrogen cycle responded quickly and strongly to glacial-interglacial climate changes, with major consequences for oceanic productivity and potential contributions to climate change feedbacks via altering the partiton of CO_2 between the ocean and atmosphere (Altabet [2001]).

---

[4] Myr = million years

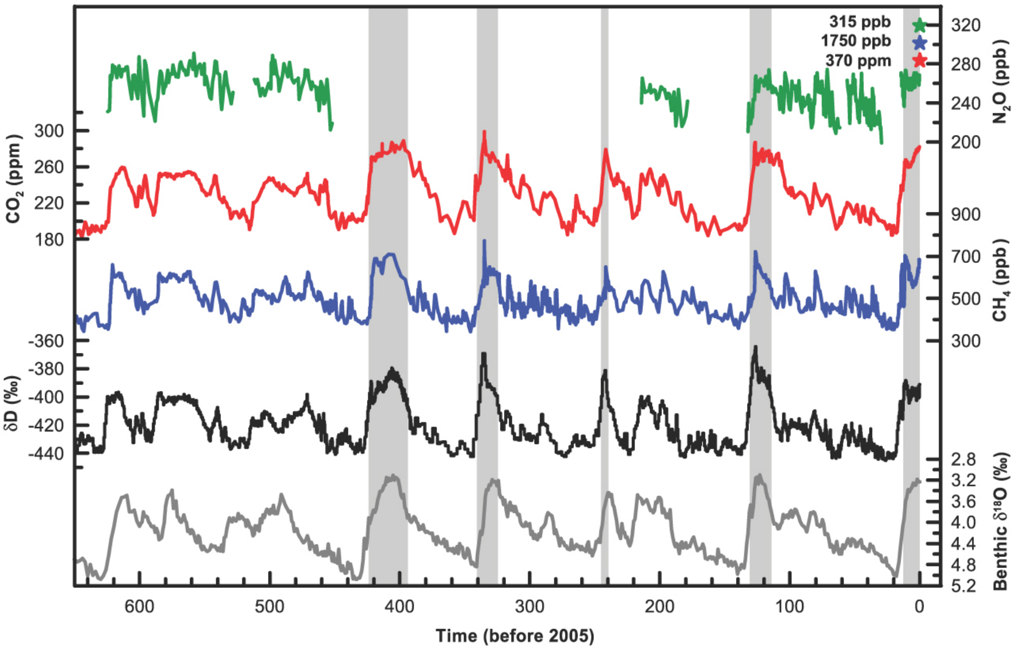

Figure 1.3: Variations of deuterium (δD, a stable isotope of hydrogen; black), a proxy for local temperature, and the atmospheric concentrations of the greenhouse gases carbon dioxide (CO_2; red), methane (CH_4; blue), and nitrous oxide (N_2O; green) derived from air trapped within ice cores from Antarctica and from recent atmospheric measurements. The stars and labels indicate atmospheric concentrations at year 2000. The unit of the time axis is [kyr]. The shading indicates the last interglacial warm periods. Interglacial periods also existed prior to 450 kyr, but these were apparently colder than the typical interglacials of the latest Quaternary. The length of the current interglacial is not unusual in the context of the last 650 kyr. The stack of 57 globally distributed benthic δ^{18}O marine records (dark grey), a proxy for global ice volume fluctuations, is displayed for comparison with the ice core data. Downward trends in the benthic δ^{18}O curve reflect increasing ice volumes on land. Figure taken from Jansen et al. [2007], Figure 6-3, more details and references therein.

Although, as described above, events like volcanic eruptions and astronomically driven insolation changes can trigger climate changes, a lot of other processes are involved in actually changing the climate.

Ice core records indicate greenhouse gases to co-vary with antarctic temperature over glacial-interglacial cycles, suggesting a close link between natural atmospheric greenhouse gas variations and temperature (see Figure 1.3). Variations in CO_2 over the last 420 kyr broadly lagged antarctic temperature, typically by several centuries to a millennium (Jansen et al. [2007]).

Many processes that could potentially regulate atmospheric CO_2 on glacial-interglacial time scales have been identified. However, the existing proxy data with which to test hypotheses are relatively scarce, uncertain, and their interpretation is partly conflicting (Jansen et al. [2007]).

1.4 Mechanisms involved in climate change

Most explanations favor changes in oceanic processes as the cause of low glacial CO_2 concentrations. The ocean is by far the largest reservoir of fast-exchanging carbon (<1 kyr), and terrestrial changes cannot explain the low glacial values of atmospheric CO_2, because terrestrial storage of carbon was also low at the Last Glacial Maximum. On glacial-interglacial time scales, atmospheric CO_2 is mainly governed by the interplay between air-sea exchange, ocean circulation, marine biological activity, ocean-sediment interactions, and seawater carbonate chemistry.

1.4.1 Shutdown of the meridional overturning circulation

The most profound way in which the ocean, whose heat capacity is 1000 times larger than that of the atmosphere, could alter the climate without involving biogeochemistry is a reorganization or complete collapse of the meridional overturning circulation (MOC), which determines the meridional transport of heat, energy and tracers like salt and nutrients within the ocean. The MOC is driven by the joint effort of thermohaline forcing, i.e. the density change caused by fluxes of heat and water through the sea surface, and by turbulent mixing, i.e. the interior mixing of heat and salt: The thermohaline forcing involves the “pulling” of the whole conveyor belt (See Figure 1.4) by the formation North Atlantic deep water (NADW), which pulls warmer and saltier water from lower latitudes northward when it sinks. This water cools, its density increases, it starts to form new NADW and sink (Broecker [1987]; Rahmstorf [2003]). On the other end of the conveyor, the cold water has to be mixed upward again, before it can close to the surface drift back to the North Atlantic, thereby closing the cycle.

Evidence of collapses of the MOC, so-called Heinrich events, exist for at least 12 different occasions during the last glacial: rock fragments that fell out of melting icebergs when they were drifting southward can be found over wide regions of the North Atlantic ocean. The input of freshwater from those melting icebergs is a mechanism that could potentially explain the shutdown of the MOC: by freshening the North

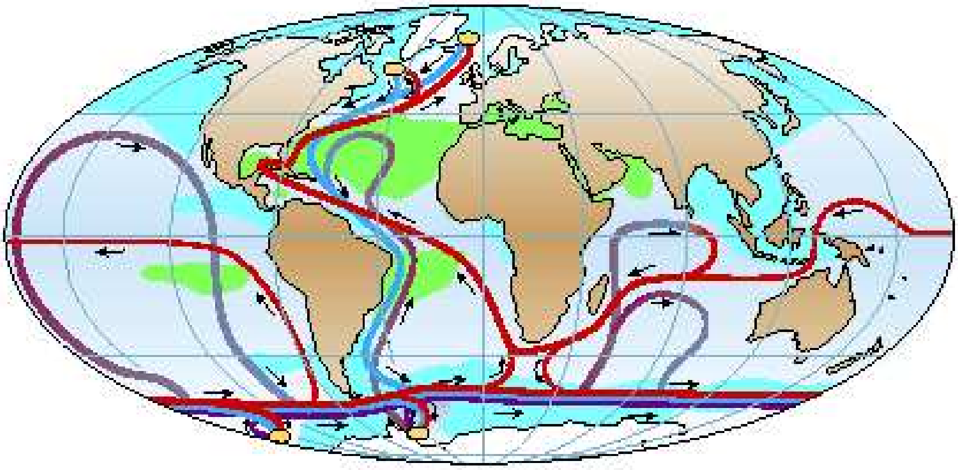

Figure 1.4: Simplified cartoon of the global thermohaline circulation (sometimes called "conveyor belt"). Near-surface waters (red lines) flow towards three main deep-water formation regions (yellow ovals) - in the northern North Atlantic, the Ross Sea and the Weddell Sea - and recirculate at depth (deep currents shown in blue, bottom currents in purple; green shading indicates areas of high surface salinity, blue shading indicates low surface salinity). Figure taken from Rahmstorf [2002], box 1.

Atlantic ocean, densities of the surface waters decrease and hence inhibit the formation of NADW. When the MOC is shut down, heat transport between the hemispheres is strongly disturbed, leading to an interhemispheric see-saw effect. Three modes of the Atlantic circulation have existed during the last glacial(Broecker et al. [1985], see Figure 1.5): The prevailing cold mode, warm (Dansgaard-Oeschger) and "off" (Heinrich). They occurred with a strikingly regular cycle every 1470 yr (see Figure 1.6). However, it remains unclear what triggered those events. The closest lunar cycle of 1,800 yr cannot be reconciled with these events (Rahmstorf [2003]). The possibility of such a behavior of the MOC as response to increased greenhouse gas concentrations has been shown in coupled ocean-atmosphere models as response to freshwater forcing (Clark et al. [2002]).

But the influence of the ocean on climate reaches much further than only transporting heat from the equator poleward. Of the 315 billion tons of carbon that are estimated to have been released to the atmosphere through burning of fossil fuels and cement production between 1751 and 2004 (Marland et al. [2007]), about 1/3 to 1/2 has been taken up by the oceans (Siegenthaler and Sarmiento [1993]).

Storage of carbon in, and release of carbon from the ocean happens through

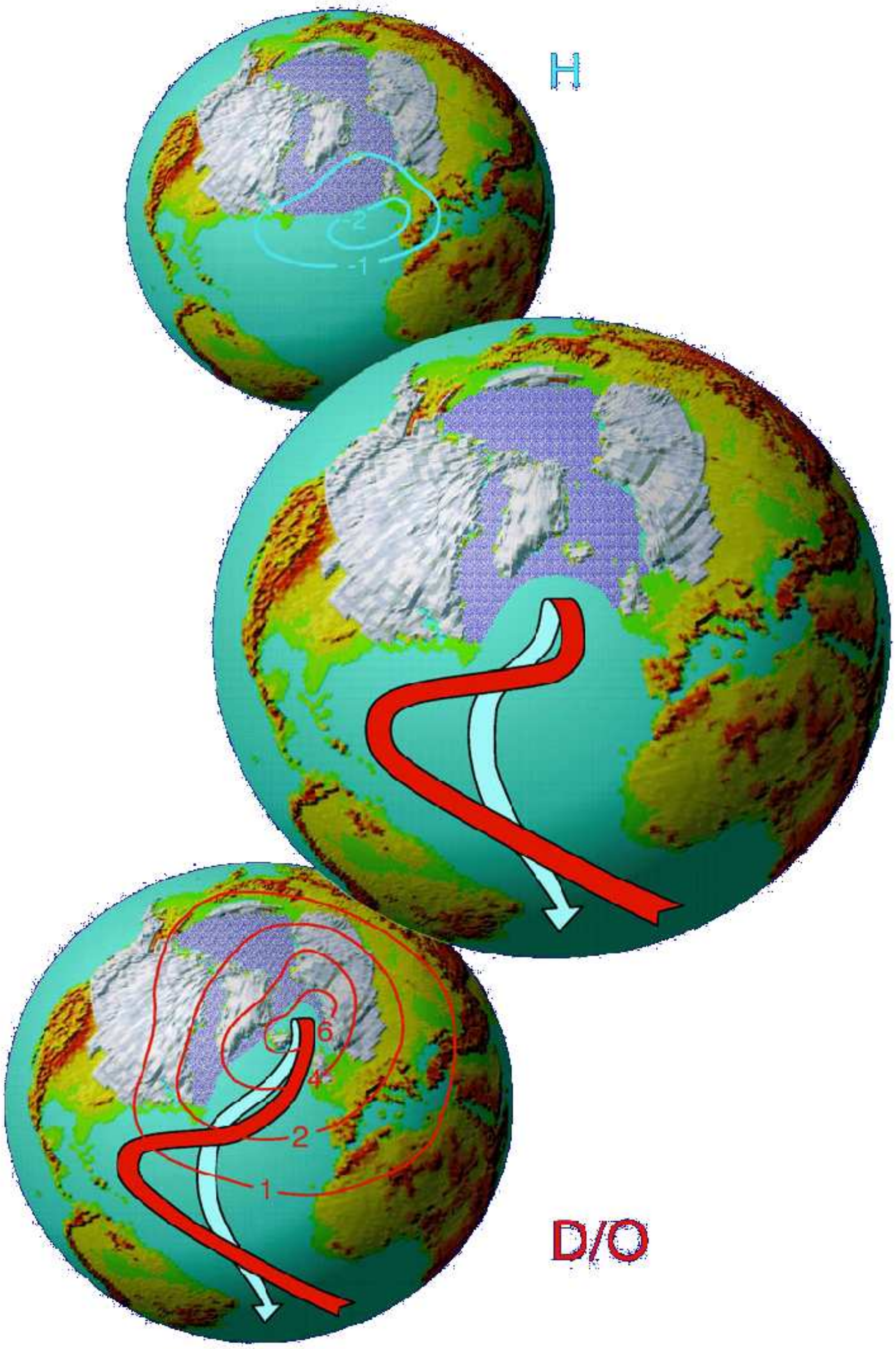

Figure 1.5: Schematic of three circulation modes of the glacial Atlantic: the prevailing cold mode (center), the warm mode associated with Dansgaard-Oeschger events (lower) and the “off” mode occurring after Heinrich events (upper globe). Figure from Rahmstorf [2006], Figure 14.

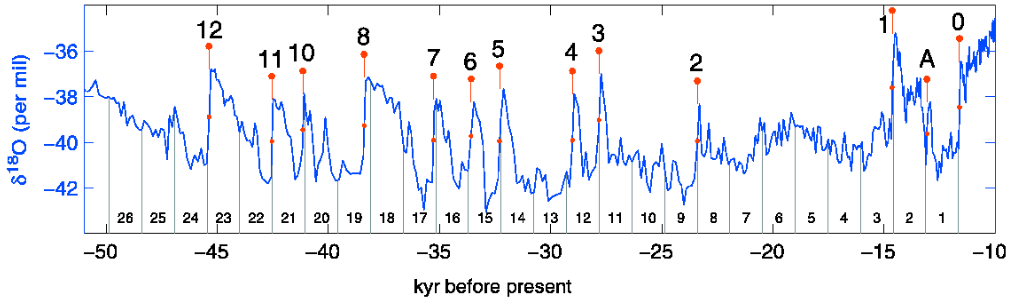

Figure 1.6: Climate record for the second half of the last glacial. Dansgaard-Oeschger (DO) warming events found by an objective detection algorithm (see Rahmstorf [2003]) are labeled with red flags. The grey vertical lines show 1,470-year spacing, small numbers at the bottom count the number of 1,470-year periods from DO event 0 (Younger Dryas). Figure from Rahmstorf [2003], Figure 1.

different processes. Using physical processes only, one model to explain the redistribution of carbon throughout the ocean and the atmosphere is the so-called "solubility pump". A more complex model, incorporating biochemical processes, is the biological pump. If geological processes and feedback mechanisms are also included, complexity increases further. This is described in the following.

1.4.2 Solubility pump

Exchange of gases between the ocean and the atmosphere is driven by differences of partial pressure between the atmosphere and the ocean surface. With lower atmospheric than oceanic carbon dioxide partial pressure, the ocean outgases carbon dioxide to the atmosphere and vice versa. Carbon dioxide solubility is a function of temperature, salinity, air pressure, and other factors, with temperature and salinity being the most important ones. The lower the temperature, the higher the solubility of CO_2 in seawater. As ocean temperature decreases, more CO_2 can dissolve in water and hence be drawn from the atmosphere. The effect of ocean salinity is opposite to that of temperature: the higher its salinity, the less CO_2 dissolved in water.

Exchange of CO_2 between atmosphere and ocean would reach equilibrium within 6-12 months, depending on the depth of the surface mixed layer, should no processes redistributing carbon in the ocean exist. CO_2 of the surface ocean is continuously reset by its interaction with the deep ocean reservoir of inorganic carbon, which is 25 times larger than the atmospheric and surface ocean reservoirs combined. As described above, global ocean circulation draws down water masses keeping them away from contact with the atmosphere for long times. Of the oceanic CO_2 sinks, the North Atlantic is the most important one (Takahashi et al. [1997]; Sabine et al. [2004]) and water masses subducted here are likely not in touch with the atmosphere again for several hundreds of years (See Figure 1.4). Antarctic bottom water that sink even deeper and - being colder and fresher - should dissolve CO_2 better, if only temperature and salinity influenced solubility. However, in case of the Antarctic bottom water solubility is primarily influenced by the Revelle factor, the ratio between dissolved inorganic carbon and alkalinity, inhibiting further uptake of CO_2.

1.4.3 Biological pump

The biological pump describes the biologically affected parts of the oceanic carbon cycle (see Figure 1.7). Photosynthesis reduces the partial pressure of carbon dioxide in the upper ocean, allowing the ocean to take up more CO_2 from the atmosphere than a hypothetical abiotic ocean would (Oschlies and Kähler [2004]). The net effect on the ocean's carbon inventory, and hence in the partition between ocean and atmosphere, is only achieved because photosynthesis and respiration do not balance locally.

Nutrients such as nitrate and phosphate, as well as iron and other micronutrients, are supplied to the surface ocean by rivers and dust. In the well-lit upper ocean, the euphotic zone, photosynthesis in phytoplankton converts carbon dioxide to organic compounds, and bacteria convert otherwise not biologically available dissolved elementary nitrogen into ammonia. Phytoplankton gets then eaten by zooplankton, and the nutrients are recycled through several steps of the food chain, called trophic levels. Dead material gets partly taken up again by other organisms, and partly sinks out of the upper ocean. On its way down, dead material is remineralized, i.e. organic molecules are transformed back to inorganic forms like nitrate and phosphate. Dead material that falls to the sea floor before being remineralized can also be sedimented. Ocean circulation and mixing act on all these processes. Of these, the process most often mentioned in connection with the biological pump is upwelling, i.e. the transport of nutrient-rich water from depth back to the euphotic zone, which closes the cycle of the biological pump.

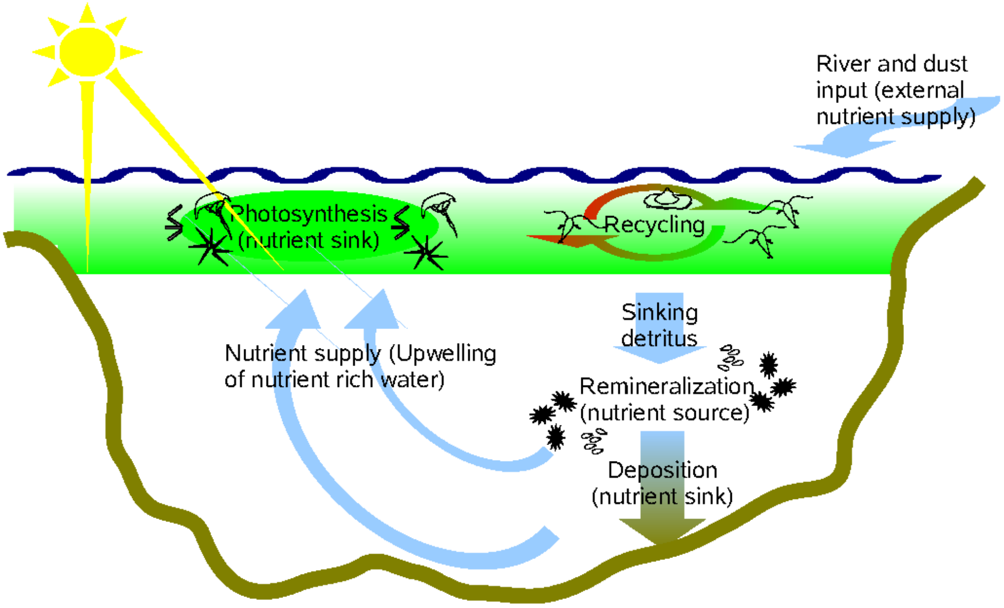

Figure 1.7: Schematic illustration of the biological pump.

1.4.4 Carbonate chemistry

Another factor complicating the carbon cycle is the chemical reactivity of carbon dioxide in water. At typical oceanic conditions, dissolved inorganic carbon (DIC) occurs predominantly (up to 91 %) as the bicarbonate ion (HCO_3^-) in the ocean, as up to 8 % as the carbonate ion (CO_3^{2-}) and up to 1 % as physically dissolved CO_2. Only the CO_2-fraction of the carbonate species can directly exchange with the atmosphere. The proportion of the different carbonate species depends on factors such as the alkalinity of the water, which in turn depends on the total amount of dissolved carbonate species (Revelle factor). For a further increase of atmospheric CO_2 concentrations of 100 ppm (i.e. from 370 ppm to 470 ppm) the CO_2 uptake by the ocean is reduced by 40 % compared to during the first 100 ppm increase from 280 ppm to 380 ppm since the start of industrialization.

Some marine organisms have calcite shells ($CaCO_3^{2-}$). Shallow waters are usually supersaturated in calcite, so as these marine organisms die, they sediment without dissolving. With increasing depth, the corresponding calcite saturation of seawater decreases and the shells start to dissolve. From a certain depth downward, the rate of dissolution increases quickly. Below the carbonate compensation depth (CCD), on average in 4,5 km depth, all calcite being supplied is directly dissolved, such that no calcite is deposited.

The depth of the CCD depends on the chemical composition of the seawater and its temperature. Hence, it is not constant over time and was globally much shallower for example in the Cretaceous through to Eocene. If the atmospheric concentration of carbon dioxide continues to increase, the CCD can be expected to rise, along with the ocean's acidity.

1.4.5 Feedback mechanisms

Climatically induced changes can have strong impact on for example element cycling, some of which act as positive and negative feedbacks in the coupled atmosphere-ocean-biogeochemistry system. The combination of positive and negative feedbacks determines the stability of the biogeochemistry-climate-system. These feedbacks act on very different spacial and temporal scales.

An example for a fast acting, positive feedback loop is the albedo feedback: Sea ice is covered with snow. As snow is white, it has a high albedo, which means that most of the solar radiation is reflected and only very little of the energy is absorbed. Once snow starts to melt, the puddles on the ice are darker than the snow, hence have a lower albedo, hence absorb more energy. When eventually the ice is completely molten, the darker ocean absorbs even more heat. Hence melting ice causes even more ice to melt.

Another example for a positive feedback is the phosphorous cycle feedback. Suboxic oxygen conditions lead to the benthic release of phosphate and iron from the organic-rich sediments (Bruland et al. [2005], see also Figure 1.8), which in turn sustains higher primary production. Higher production leads to more dead material sinking down from the surface ocean, consuming oxygen when being remineralized, leading to lower oxygen concentrations which closes the loop.

An example for a negative feedback is the nitrogen cycle feedback. Under hypoxic conditions, nitrate concentrations are lowered via enhanced denitrification and the anaerobic oxidation of ammonium. This leads to lower productivity. A lower subsurface oxygen demand does not help sustain the low oxygen values and if the supply of oxygenated water remains constant, oxygen values in the region are going to increase. However, this negative feedback can be offset by nitrogen fixation, but is also affected by the availability of other nutrients, thereby linking this feedback loop to for example the phosphorus cycle feedback.

A feedback on a very long time scale involving not only the ocean, but also the Earth's crust, is the chemical weathering of rocks that make up the Earth's crust,

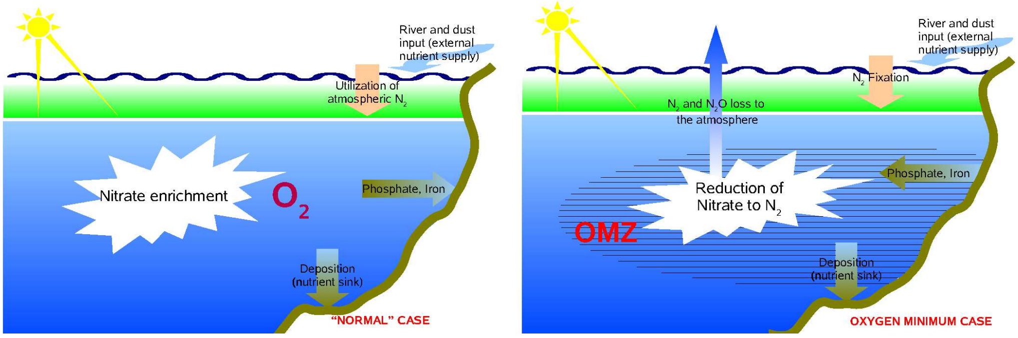

Figure 1.8: Schematic illustration of the biological pump under normal oxygen conditions (left) and low oxygen conditions (right).

which controls CO_2 levels on time scales of millions of years. When atmospheric CO_2 levels are high, the climate is hot and wet, which enhances the breakdown of silicate rocks which changes ocean alkalinity. CO_2 then is drawn from the atmosphere into the ocean and incorporated into calcium carbonate minerals, which are eventually sedimented. When then the atmospheric CO_2 concentrations is lower, the climate is colder and dryer, hence weathering slows down and less CO_2 is removed from the atmosphere.

1.5 Oxygen as switch for marine biogeochemistry

Oceanic oxygen concentrations act as a switch on marine biogeochemistry. For oxygen concentrations below certain thresholds, chemical and microbial processes radically different from those in the rest of the world's oceans start to operate. The oceanic production and destruction of climate relevant trace gases like methane and nitrous oxide and indirectly also carbon dioxide, and as a result the oceanic uptake and release of those trace gases as well as the availability of nutrients, depend on the oceanic oxygen levels. Relatively small zones with oxygen levels below the threshold, so called oxygen minimum zones (OMZs), can therefore have a big impact on nutrient budgets, biological productivity and the cycles of nitrogen and carbon. Classical denitrification (microbially facilitated process of dissimilatory nitrate reduction that may ultimately produce molecular nitrogen (N_2) through a series of intermediate gaseous nitrogen oxide products) and anaerobic oxidation of ammonium coupled to the reduction of nitrite with production of N_2 (ANAMMOX, Kuypers et al. [2005]) lead to the "loss" of biologically available nitrogen from the ocean to the atmosphere. Within hypoxic OMZs (oxygen concentration below $5\,\mu$mol/l) which cover

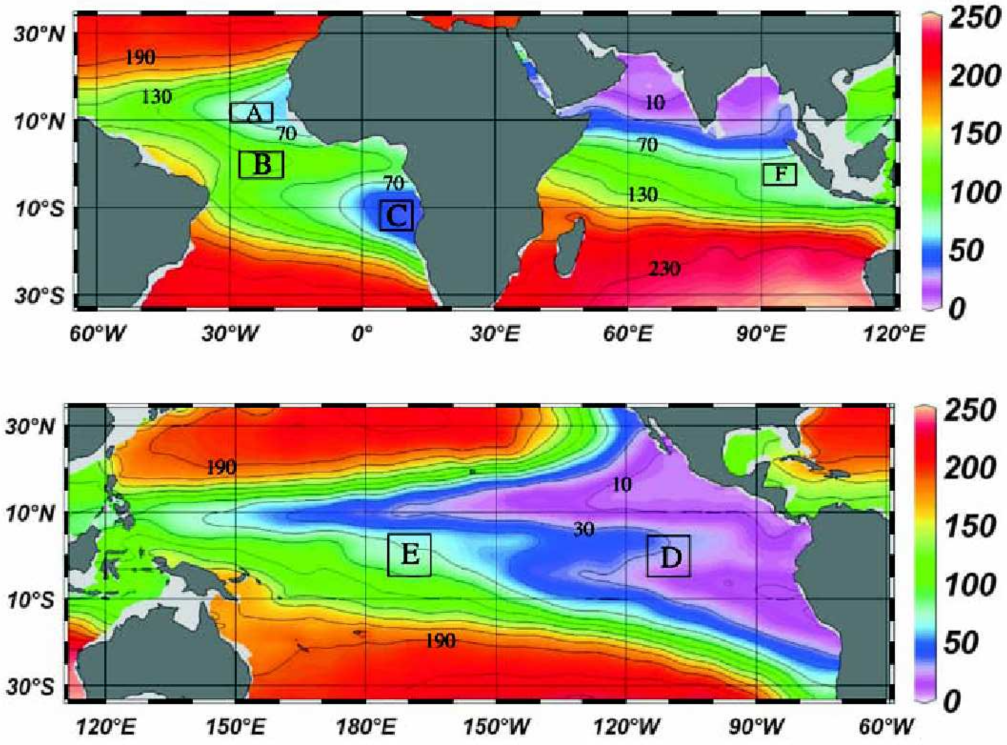

Figure 1.9: Climatological mean WOA05 (Garcia et al. [2006]) dissolved oxygen concentrations (μmol/kg shown in color) at 400 m depth contoured at 20 μmol/kg intervals from 10 μmol/kg to 230 μmol/kg (black lines). Areas A to F are enclosed by black boxes and referred to again in Figure 1.10. Figure taken from Stramma et al. [2008b], Figure 1.

only approximately 0.1 % of the ocean volume, 30-50 % of the fixed nitrogen loss in the ocean occurs (Codispoti et al. [2001]; Gruber and Sarmiento [1997]). Small changes in the extent of OMZs can therefore have a large influence on global nitrogen cycling.

In today's oceans, only the Pacific and Indian Ocean reach oxygen concentrations below the detection limit. Atlantic oxygen values are typically above 40 μmol/kg (See Figure 1.9), only for fall 2008 values below 40 μmol/kg have been reported in the core of the North Atlantic OMZ (Stramma et al. [2009]) But throughout the ocean oxygen concentrations are expected to decrease with global warming (Bopp et al. [2002]; Matear and Hirst [2003]), which was recently supported by observational results (Stramma et al. [2008b], see Figure 1.10). Warming itself influences solubility of O_2 and can explain 25 % of the observed O_2 decline.

Atlantic and Pacific OMZs are located in "shadow zones" (Luyten et al. [1983]; Sverdrup [1938]; Wyrtki [1962], see Figure 1.11)) with little advective ventilation

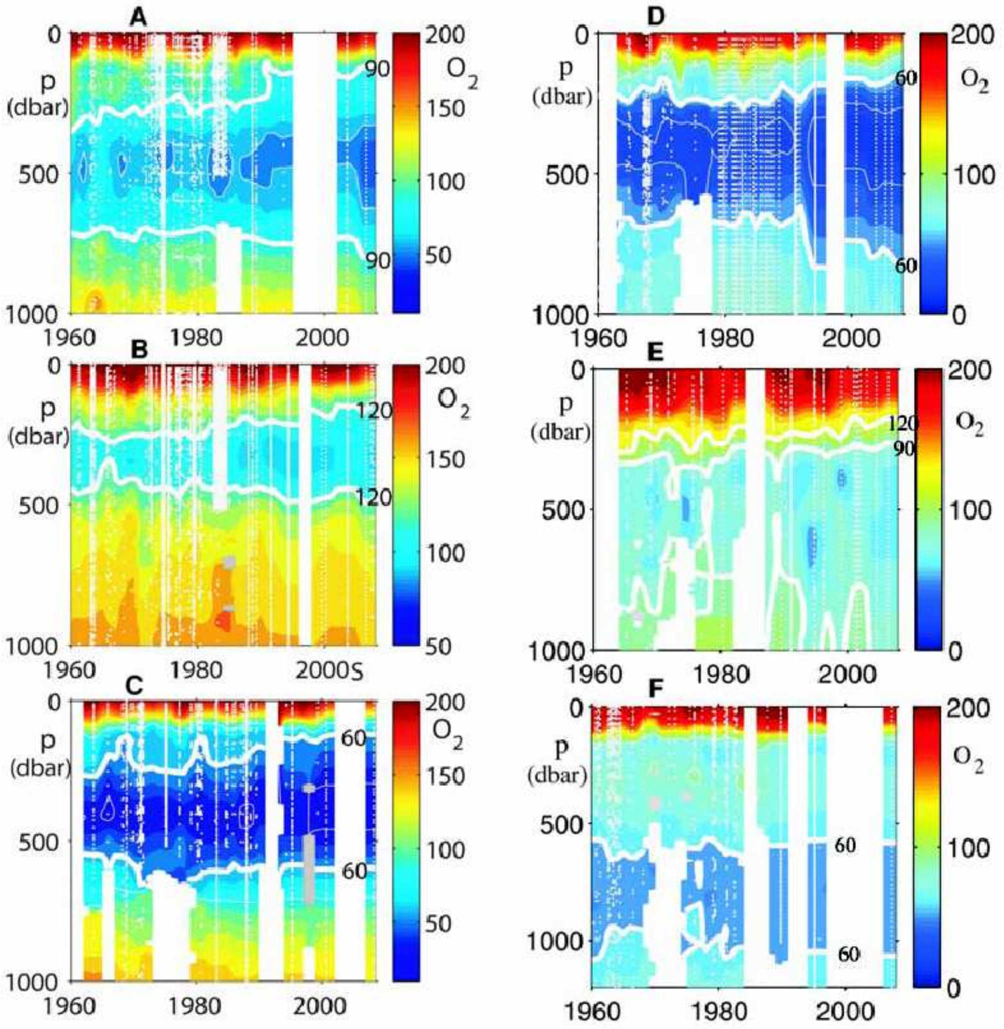

Figure 1.10: Dissolved oxygen concentration (μmol/kg shown in color) maps versus time (1960 – 2008) and pressure (1 dbar ∼ 1 m) with sample locations (white dots). (A) The eastern tropical North Atlantic (10°N to 14°N, 20°W to 30°W), contoured at 90 mmol/kg (thick white line). (B) The central equatorial Atlantic (3°S to 3°N, 28°W to 18°W), contoured at 120 mmol/kg (thick white line). (C) The eastern tropical South Atlantic at (14°S to 8°S, 4°E to 12°E), contoured at 60 μmol/kg (thick white line). (D) The eastern equatorial Pacific Ocean (5°S to 5°N, 105°W to 115°W), contoured at 60 μmol/kg (thick white line). (E) The central equatorial Pacific Ocean (5°S to 5°N, 165°W to 175°W), contoured at 90 μmol/k and 120 μmol/kg (thick white lines). (F) The eastern equatorial Indian Ocean (5°S to 0°S, 90°E to 98°E), contoured at 60 μmol/kg (thick white line). Figure taken from Stramma et al. [2008b], Figure 2.

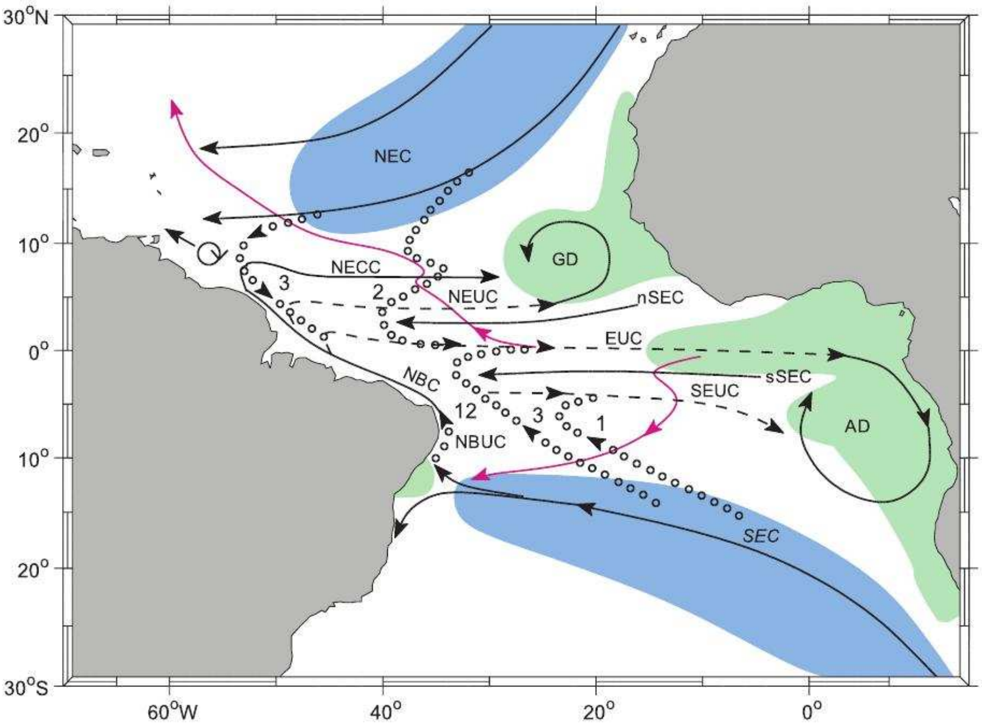

Figure 1.11: Schematic representation of the Atlantic subtropical cell (STC) circulation with subduction (blue) and upwelling (green) zones that participate in the STC. Current branches participating in STC flows are NEC, SEC = North and South Equatorial Current; NECC = North Equatorial Countercurrent; EUC = Equatorial Undercurrent; NEUC, SEUC = North and South Equatorial Undercurrent; NBC, NBUC = North Brazil Current and Undercurrent; GD, AD = Guinea and Angola domes. Interior equatorward thermocline pathways dotted, transport estimates marked for interior and western boundary pathways; surface poleward pathways for the central basin marked by thin, magenta line. Figure taken from Schott et al. [2004], Plate 3.

where old waters can stay for a long time with little or no new oxygen being supplied. They are also in close vicinity to the highly productive upwelling areas at the eastern boundary and the equator, where degrading of dead organic material uses up oxygen.

1.5.1 Circulation in the tropical-subtropical oceans

The location and strength of OMZs depends on both physical and biogeochemical processes. Of the physical processes, especially the shallow overturning circulation of the tropical oceans and the equatorial current system, sketched in Figure 1.11, are important in determining where ventilation is sluggish enough to allow for very old waters that are associated with subtropical OMZs.

In the Atlantic and Pacific oceans, shallow wind-driven overturning cells confined to the upper 500 m exist. Those so-called subtropical cells (STCs, McCreary and Lu [1994]) connect through equatorward thermocline and poleward surface flow (Schott et al. [2004]) the subtropical subduction regions of both hemispheres to the eastern equatorial upwelling regions (and the eastern boundary upwelling systems in both oceans as well as the Costa Rica dome in the Pacific, the Guinea and Angola dome in the Atlantic Ocean). The STCs hence provide the cool subsurface water that is required to maintain the tropical thermocline. Models and observations show that wind-driven changes in STC strength modulate the supply of cold subtropical waters to the equatorial upwelling in the Pacific (McPhaden and Zhang [2002]; Capotondi et al. [2005]) and Atlantic Ocean (Kröger et al. [2005]).

The strength of the STCs in the Atlantic and Pacific Ocean is influenced by interocean circulations. In the Atlantic Ocean, the STCs are overlaid with the MOC which transports 15 Sv (Ganachaud and Wunsch [2000]), and in the Pacific with the Indonesian Throughflow with transports of 10 Sv - 15 Sv (Sloyan et al. [2003]). Those transports of warm water northwards over the equator interact with the STCs and lead in both cases to stronger southern than northern STCs.

Additionally to being influenced by interocean circulations, STCs also interact with the equatorial current system, where many zonal current bands in the thermocline and sub-thermocline layers exist (See Figure 1.12 for a repeatedly measured velocity section across the equator at 35°W (after Schott et al. [2003]), and Figure 1.13 for the same section from output of the models used in Chapter 4, averaged over the years in which the section was measured.). The structure of the equatorial current system is very similar in the Atlantic and Pacific Ocean, therefore in the following the Atlantic is used to illustrate the structure, and only points where differences to the Pacific exist are highlighted.

Because of the strong density stratification in the equatorial region, wind-driven motion is confined to the mixed layer and the upper thermocline. The North and South Equatorial Current (NEC and SEC, respectively) are the surface current bands furthest away from the equator. They are shallow, less than 200 m deep, westward bands which are part of the equatorward limb of the wind-driven subtropical gyres. The North Equatorial Countercurrent (NECC) is centered between

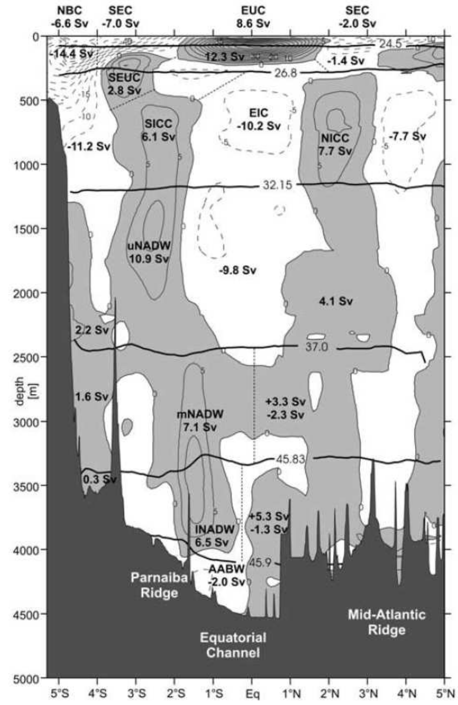

Figure 1.12: Mean zonal current distribution across 35°W from the 13 sections, with transports (in Sv = $10^6\,\mathrm{m^3s^{-1}}$) of the different current branches marked. Figure taken from Schott et al. [2003], Figure 2.

3°N and 10°N in regions of low windspeed underneath the Intertropical Convergence Zone between the NEC and SEC, where during northern hemisphere summer the extensions of the southeast trade winds cause eastward surface flow.

At the equator, the Equatorial Undercurrent (EUC) exists above 200 m (Schott et al. [2003]). The pressure gradient, caused by the warm pool with high sea surface hight and deep thermocline in the west, leads to eastward flow, which is centered on the equator by the Coriolis force, and mainly fed by southern hemisphere sources (Metcalf and Stalcup [1967]).

In the subsurface layers between 50 m and 300 m, off-equatorial undercurrents (North and South Equatorial Undercurrent, NEUC and SEUC, in the Atlantic, and Northern and Southern Subsurface Countercurrent, NSCC and SSCC, in the Pacific) feed the domes and eastern upwelling systems. In the system of current bands between 4° and 8° off the equator, exchange between the different current bands is commonly taking place, and the current system contributes to the coastal and equatorial upwelling described above (Hüttl-Kabus and Böning [2008]). Those

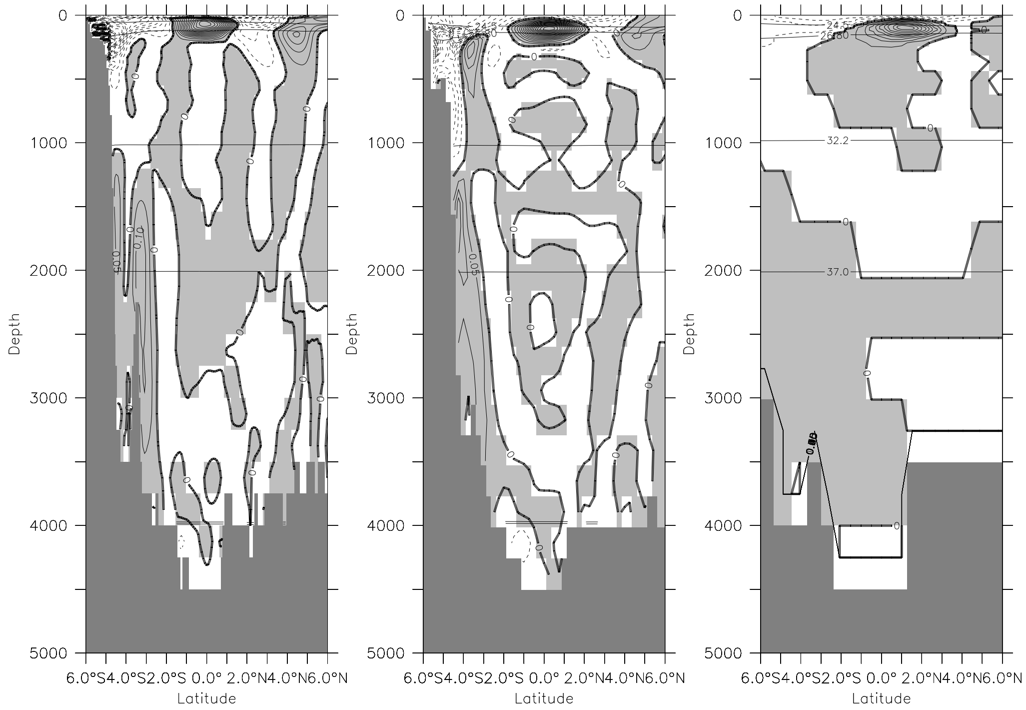

A: FLAME

B: ORCA025

C: ORCA2

Figure 1.13: Mean modelled zonal current distribution across 35°W from FLAME (Panel A), ORCA025 (Panel B) and ORCA2 (Panel C).

currents can be seen as a deep, off-equatorial branch of the STCs (Schott et al. [2004]).

Inside the STCs, two equatorward subsurface pathways exist (Malanotte-Rizzoli et al. [2000]). They carry thermocline water to the equator either in western boundary currents after circulating across the basin in the Subtropical Gyres ("western boundary exchange window") or directly in the ocean interior ("interior exchange window").

The theory of the "ventilated thermocline" (Luyten et al. [1983]) describes how divergent or convergent wind stress (Ekman pumping) can subduct water to intermediate depths, resulting in temperature transfer to, and circulation at, those depths, which agree well with observed oceanic temperature and circulation. However, the ventilated thermocline model only describes a wind-driven circulation and neglects other processes that generate large-scale temperature gradients in the ocean like for example the MOC. Zero viscosity is assumed and the seasonal cycle is neglected. Also, the western boundary currents needed to close the model lie effectively outside the theory. From the theory, "shadow zones" can be deducted. Shadow zones are regions bound by contours of potential vorticity emerging from

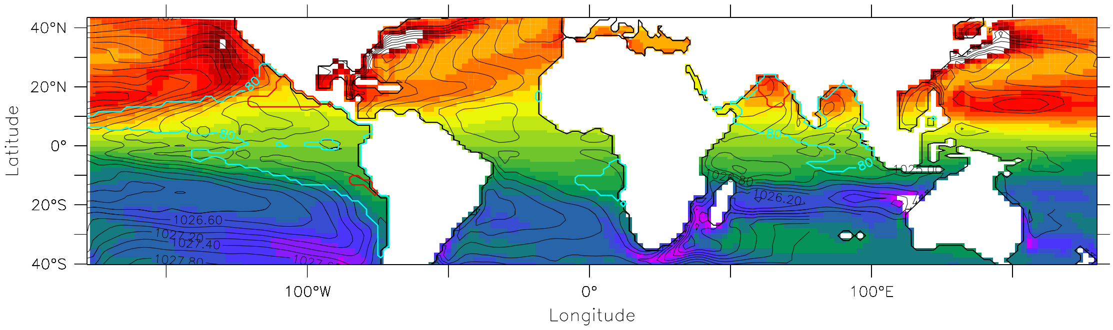

A: PV at 200m ORCA2

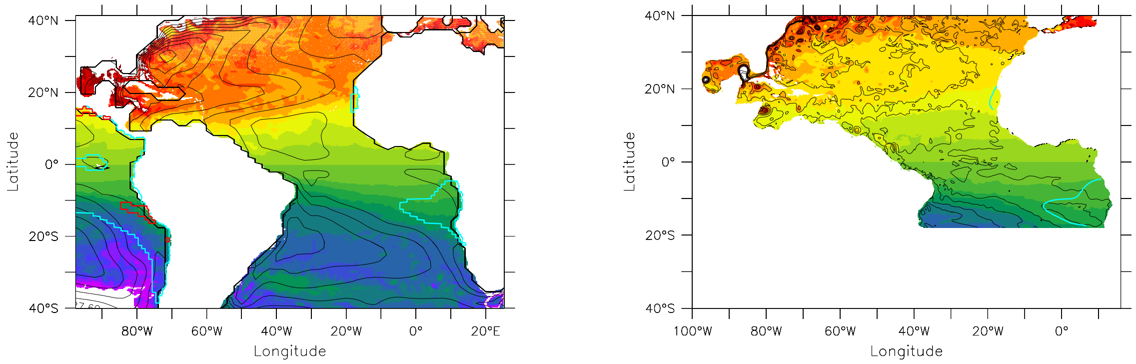

B: PV at 200m ORCA025

C: PV at 200m FLAME

Figure 1.14: Panel A, B and C show potential vorticity at 200 m depth for ORCA2, ORCA025 and FLAME on January 15th, respectively. Colorscale ranging from $-10\times10^{-10}\,\mathrm{m}^{-1}\mathrm{s}^{-1}$ in purple to $10\times10^{-10}\,\mathrm{m}^{-1}\mathrm{s}^{-1}$ in red. Black contours indicate density, light blue contours are 80 μmol/l and red contours 10 μmol/l WOA05 oxygen concentration at that depth.

meridional boundaries. These regions are either uniform in potential vorticity or stagnant.

The "shadow zones" can be seen in model output, too. Figure 1.14 shows potential vorticity at 200 m depth for January 15th for the three models used in Chapter 4: ORCA2 with a 2°, ORCA025 with 1/4° and FLAME with 1/12° horizontal resolution. Black contours show density at 200 m depth: In the shadow zone region, investigations based on z-levels are appropriate because isopycnals are approximately horizontal. Overlaid on the potential vorticity are oxygen concentration contours, showing that in the case of both the Atlantic and the Pacific Ocean OMZs shadow zones and OMZs are located in the same regions.

1.6 Predicting the future

The oceanic oxygen levels are determined both by physical and biogeochemical processes. Circulation and mixing transport oxygen from the surface layers where it is exchanged with the atmosphere and produced by photosynthesis into the ocean interior. Throughout the ocean, oxygen is consumed by the remineralization of organic matter, which is sinking down from the surface ocean. Consequences of changes to the system and feedbacks within have not completely been predicted yet, and the relative importance of the physical and biogeochemical processes is still largely unknown. This thesis concentrates on physical processes in the attempt to understand the arguably more simple physical system first (Flynn [2005]), while always keeping in mind that biological processes may play a similar or even bigger role in the final solution.

1.6.1 Models

Physical processes responsible for the distribution of oxygen and other substances in the ocean are advection and diffusion. The distinction between advection and diffusion depends on the scales in question. In the Navier-Stokes equations, a set of differential equations describing the motion of a fluid, diffusion is only pure molecular diffusion, while all other transport processes are due to explicitly described advection. In numerical ocean models, the Navier-Stokes equations are discretized and solved on a grid. If we were able to resolve all scales and knew the correct initial conditions and forcings, we could describe the state of the ocean at any time anywhere. However, it is technically not possible to solve all temporal and spatial scales, and cheaper, especially for long runs of climate models, to go to even coarser resolutions than what would be the finest scale technically possible. Due to capacity constraints of computing facilities, grid points typically have a horizontal spacing between 1/10th of a degree or less in regional models, and 2 degrees or more in coupled climate models. Vertical resolution thereby typically ranges from some 10 m in the upper ocean to several 100 m near the bottom. In those ocean models, every process on scales smaller than the grid spacing or faster than the time step is not explicitly resolved any more and must be parameterized.

In ocean circulation models, it has been shown that higher horizontal resolution leads to more realistic representation of the mean circulation, heat budgets, sea surface height, mixed layer depth and western boundary currents (Oschlies [2002];

Hurlburt and Hogan [2000]). However, there is currently no consensus on the optimal way to divide computer resources among higher resolution (which allows for better simulations), greater number of ensemble members (better statistical estimate of uncertainty) and inclusion of a more complete set of processes (e.g. carbon feedbacks, atmosphere chemistry interactions) (see Randall et al. [2007]).

1.6.2 Small scale processes in the real ocean

While larger-scale motions in the ocean are thought to be largely known both from direct measurements and from ocean model results, mixing in the ocean is still poorly understood. Even the order of magnitude of turbulent diffusion is still being discussed.

While in the ocean a strong meridional overturning circulation (MOC, see Figure 1.15) exists, the density stratification below the thermocline is stable almost everywhere (Wunsch and Ferrari [2004]). Both the MOC and the stable stratification can only be maintained by small scale mixing processes balancing the turbulent downward mixing of heat by a mean vertical current (See Figure 1.15). The required mixing has been estimated from observations of oceanic temperature, salinity, oxygen and carbon-14 by Munk [1966]. However, his global value of required diffusion of approximately $1 \times 10^{-4}\,\mathrm{m}^2/\mathrm{s}$ cannot easily be reconciled with physical considerations of mixing processes.

Measurements of turbulence in the ocean typically lead to diapycnal diffusivities which are much lower than Munk's hypothised value. Ledwell et al. [1993] for example found a diapycnal eddy diffusivity of $(1.1 \pm 0.2) \times 10^{-5}\,\mathrm{m}^2/\mathrm{s}$ in the North Atlantic Tracer Release Experiment. These and other open-ocean experiments indicate that turbulent mixing is mainly driven by the breaking of internal waves and shear instability at boundaries and, to a smaller extent, by double diffusion (Gregg [1987]).

Only combined with localized hot spots of mixing from where water masses, but not turbulence, get exported into the interior ocean, those very low values of mixing in the interior can explain the observed tracer fields (Munk and Wunsch [1998]). Mixing due to breaking of internal waves or by shear at oceanic boundaries like along continental slopes, above seamounts and mid-ocean ridges, at fronts, and in the mixed layer at the sea surface has been shown to provide these hot spots, reaching values of turbulent diffusivity of $1 \times 10^{-3}\,\mathrm{m}^2/\mathrm{s}$ (Polzin et al. [1997]; Kunze and Toole [1997]; Garabato et al. [2004]).

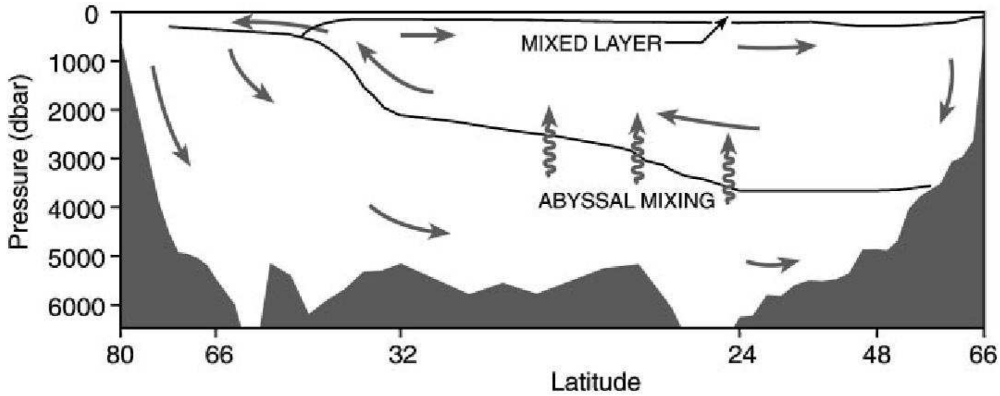

Figure 1.15: Schematic circulation showing division into gross meridional circulations in the upper and lower oceans. Relative volumes are approximately correct. Upper volume is strongly mixed in the near-surface regions. Lower one is mixed primarily at the edges and over rough interior topography. There is probably a range of densities at intermediate depths where fluid is mixed both at the sea surface and through abyssal processes in unknown proportions. Figure taken from Wunsch and Ferrari [2004], Figure 4.

1.6.3 Small scale processes in models

Depending on the horizontal and vertical model resolution, many processes can not be explicitly represented (See for example Figure 1.13 for an example how three different model resolution represent the measured section shown in Figure 1.12). Eddies, oceanic vortices with a diameter in the range of 1-100 km, are important sub-gridscale feature effecting mixing that, depending on the resolution of the model grid, often have to be parameterized. They transport among other things heat, salt, nutrients, trace gases and momentum over large distances and contain a significant share of the kinetic energy of the ocean (Wunsch and Ferrari [2004]). Mixing due to eddies is explicitly modelled in eddy-resolving models, whereas in coarse-resolution models this mixing has to be added artificially, for example in form of a parameterization of subgrid-scale mesoscale eddy mixing on isopycnal surfaces as suggested by Gent and McWilliams [1990]. However, there are other processes which are less well understood and whose importance is not yet known, for example double diffusion. Understanding of mixing processes like for example double diffusion is important in order to understand the state of the ocean. Intensified salt-fingering, in more detail described in Chapter 2, can for example reduce widely acknowledged climate change fingerprints, potentially leading to underestimates of oceanic changes in studies that do not include double diffusive mixing (Johnson and Kearney [2009]).

Most models incorporate only turbulence generated by shear instabilities, as diapycnal mixing is a subgrid-scale process requiring parameterization (Gregg [1987]). Simulated heat transport and MOC in ocean models are very sensitive to the diapycnal diffusivity used (Bryan [1987]; Zhang et al. [1999]), as is the nutrient supply to the upper ocean (Oschlies et al. [2003]).

In numerical ocean models, additional technical difficulties occur. For example, diapycnal mixing in ocean models is not exclusively determined by the explicit parameterization of diffusion, but also by numerically induced diffusion (Griffies et al. [2000b]). Diffusion can be introduced by discretization errors, particularly of the advection terms, and may cause unrealistically high diapycnal mixing. Implicit diffusion in models has only recently come into focus and is hard to quantify (Getzlaff [2008]).

Mixing depends on both the energy input into the ocean by winds and the density stratification of the ocean, both of which are expected to change in the future. Wind speeds are likely further to increase (IPCC [2007a]), thereby supplying more energy to the upper ocean, warmer temperatures and an intensified hydrological cycle are thought to stabilize the density stratification of the ocean. This will impact not only mixing but also oxygen distribution, and influence processes linked to the oxygen concentration, potentially affecting climate.

1.7 Introduction to the main chapters

The main aim of this thesis is to contribute to the understanding of the impact of the representation of small scale mixing processes in ocean models on the simulation of the ocean. In Chapter 2, the simulated impact of a specific diapycnal mixing process, double-diffusive mixing, on physical and biogeochemical upper ocean properties is shown. Double-diffusive mixing is not considered in most parameterizations of diapycnal mixing commonly used in ocean models. However, if stratification changes with global warming, double-diffusive mixing processes can gain importance as the stratification is thought to become more favorable for double diffusion, and at the same time more gravitationally stable, thereby hindering mechanical mixing processes. Double-diffusive mixing therefore may become an important process for supplying nutrients to the upper ocean (as it is already today in certain regions like for example the subtropical oceans), as well as releasing trace gases to the atmosphere. A good understanding of double-diffusive mixing and the effects of the inclusion of its parameterization in ocean models is therefore important. In this chapter, two parameterizations of double-diffusive mixing are implemented in a global ocean model with a $1^\circ \times 1^\circ$ horizontal resolution, and those two model runs are compared with a conventional non-double-diffusive run in order to determine the possible improvement made by implementing those parameterizations.

In Chapter 3, the supply of OMZ waters to the coastal upwelling off Mauritania is investigated using a high resolution (1/12°) North Atlantic model. Understanding the North Atlantic OMZ is interesting for several reasons, although oxygen concentrations are high compared to other subtropical OMZs and lie well above critical thresholds for the nitrogen cycle. One motivation for investigating this OMZ is that with the measured declining trends in oxygen concentrations, understanding this OMZ can help understand what determines oxygen concentrations in OMZs and why they differ between the different OMZs. In addition this OMZ and its connection with the upwelling off Mauritania are currently in the focus of extensive measuring campaigns, concentrating on biogeochemistry and mixing, and recently in 2008 a tracer release experiment was carried out. Soon a large amount of observational data will become available enabling the direct comparison with results presented in this study. Although in our model only about 1 % of the upwelling waters originates in the OMZ, 71 % of the OMZ waters reach the mixed layer in the coastal upwelling. Particle tracking, a method commonly used to determine pathways of watermasses by accounting only for advection, is compared with a modelled tracer release experiment in this region: In the model, the tracer reaches the mixed layer about twice as fast as the floats. After 6 years, 7 % of the simulated floats have reached the mixed layer as compared to 14 % of the tracer.

As described above, in models the distinction between advection and diffusion depends on the model resolution. Everything that can be resolved is typically called advection, while the rest is called diffusion. The finer the resolution, the more mixing processes are explicitly resolved. A coarser resolution therefore requires more parameterizations of processes formerly resolved, and thereby introduces additional uncertainties. However, the coarser the resolution the less computationally expensive the model. For long model integrations as required for climate simulations, only coarse resolutions are feasible. In Chapter 4, the connection of the Atlantic and Pacific OMZs to the upper ocean is investigated in a range of general ocean circulation models varying horizontal resolutions from high resolution (1/12°) to eddy-permitting (1/4°) to the typical resolution of coupled climate models (2°), using float and tracer release experiments. Counter-intuitively, the variability of the amount of tracer released in the Atlantic and Pacific OMZs reaching the mixed layer within 20 years is found to be quite large. Not only in the eddy-permitting ORCA025 model runs, but also in the coarse resolution ORCA2, even in climatologically forced parts of the run. This suggests that the system is much less simple than is commonly thought. Water from the Pacific OMZ reaches the mixed layer faster than water from the Atlantic OMZ. The interannual variability of the connection between the OMZs and the upper ocean is found to be surprisingly large. The regional distribution of where floats and tracer released in the OMZ is robust over the different experiments, but mechanisms determining the interannual variability are not necessarily the same, neither between different OMZs nor different models. Investigation of a coupled atmosphere-ocean model global warming run shows that the connection between the OMZs and the mixed layer is much weaker than in a present day simulation of the same model.

In Chapter 5, the results of Chapter 2, Chapter 3 and Chapter 4 are summarized. Conclusions are drawn and combinedly discussed, and an outlook into future work is given.

Chapter 2

Simulated impact of double-diffusive mixing on physical and biogeochemical upper ocean properties

This chapter is a reprint of the paper "Simulated impact of double-diffusive mixing on physical and biogeochemical upper-ocean properties" published in the Journal of Geophysical Research, reproduced by permission of American Geophysical Union.

Citation: Glessmer, M. S., A. Oschlies, and A. Yool (2008), Simulated impact of double-diffusive mixing on physical and biogeochemical upper ocean properties, J. Geophys. Res., 113, C08029, doi:10.1029/2007JC004455.

2.1 Abstract

A global ocean circulation model coupled with a simple marine ecosystem model including the biogeochemical cycles and air-sea fluxes of oxygen and carbon dioxide is used to investigate the impact of double-diffusive mixing on upper-ocean physical and biogeochemical properties. By comparing results for two different parameterizations of double-diffusive mixing, we also examine the sensitivity of our estimates to the particular representation of this process in general circulation models. Differences between the two parameterizations considered turn out to be much smaller than the difference with respect to a model run without double-diffusive mixing. For both parameterizations, the impact on upper-ocean temperatures and

salinities is relatively small ($\pm 1°C$, ± 0.25 psu regionally and 0.04°C, 0.01 psu as global rms difference over the top 50 m) and changes in surface heat flux amount to $0.05\,\mathrm{W\,m^{-2}}$ globally. However, primary production and export production in the oligotrophic subtropics are found to increase by up to 80 % and 120 %, respectively, when double diffusion is switched on in the model. Double-diffusive nutrient supply generates an additional oceanic carbon uptake of about $0.4\,\mathrm{g\,C\,m^{-2}\,yr^{-1}}$, amounting to $0.14\,\mathrm{Gt\,C\,yr^{-1}}$ globally.

2.2 Introduction

Developing an accurate description of mixing in general, and of vertical or diapycnal mixing in particular, is one of the major challenges of current state-of-the-art ocean and climate models [Griffies et al., 2000a]. Processes that generate diapycnal mixing in the stratified ocean interior include the breaking of internal waves, Kelvin-Helmholtz shear instabilities, and double diffusion. Here, we focus on double-diffusive mixing and attempt to quantitatively estimate its impact on upper ocean physics and biogeochemistry.

Double-diffusive mixing is caused by different molecular diffusivities of heat and salt. Early realizations of the potential importance of such differences include the studies of Jevons [1857] and Stommel's 'perpetual salt fountain' [Stommel et al., 1956]. In sea water, the molecular diffusion of heat is much faster, roughly by a factor 100, than that of salt [Zhang et al., 1998]. Under suitable conditions, the faster erosion of temperature gradients compared to salinity gradients on molecular scales can then generate static instabilities and subsequent macroscopic turbulence and mixing.

Double diffusion has been measured in various regions of the ocean as, for example, the lower boundary of the Mediterranean Outflow west of Gibraltar [Zenk, 1970], the western tropical North Atlantic [Schmitt, 1987], or the Arctic [Rudels et al., 1999; Timmermans et al., 2004].

You [2002] deduced from the World Ocean Atlas [Levitus, 1994] that as much as 44 % of the ocean volume satisfies the necessary conditions for double diffusion. By affecting vertical temperature and salinity profiles, double-diffusive mixing can lead to changes in surface heat fluxes and sea ice thermodynamics, possibly impacting on water mass formation and ocean dynamics. Additionally, double diffusion can act as to reduce anomalies in spiciness and thereby attenuate their possible climatic impacts [Johnson, 2006].

Double-diffusive mixing is of particular interest for estimates of upper-ocean nutrient supply to the subtropical gyres. In a regional modeling study, Oschlies et al. [2003] found that salt-finger induced mixing (parameterized after Zhang et al. [1998]) generated nutrient fluxes comparable to those associated with mechanically-induced turbulence or with mesoscale eddies. Applying the same mixing parameterization to hydrographic measurements in the subtropical North Atlantic, Dietze et al. [2004] inferred that nutrient transport into the nutrient-consuming surface layer by salt fingering was more than fivefold higher than transport due to internal-wave induced turbulence.

The aim of the present paper is to give a first quantitative estimate of the global impact of double diffusion on upper ocean properties. As a complete mechanistic understanding of the amount of macroscopic mixing generated by double diffusion is not yet available, we employ two different empirical parameterizations of double-diffusive mixing. These are introduced into a global general circulation model coupled with a simple nutrient-phytoplankton-zooplankton-detritus (NPZD) ecosystem model together with the biogeochemical cycles of carbon and oxygen, including air-sea gas exchange. The paper is organized as follows: In the following section we present the model used in this study and describe the different parameterizations of double-diffusive mixing. In section 2.4, the model results are validated against measurements. Model results are presented and discussed in section 2.5.1 with a focus on physics, in section 2.5.2 with focus on biogeochemistry and in 2.5.3 with a focus on air-sea fluxes of CO_2 and O_2 . The last section summarizes and discusses our conclusions and in an appendix the parameterizations of double-diffusive mixing used in this study are presented in more detail.

2.3 Methods

2.3.1 Model

The model used in this study is the Ocean Circulation and Climate Advanced Modelling Project (OCCAM) [Coward and de Cuevas, 2005; Sinha and Yool, 2006], a primitive equation finite difference ocean general circulation model based on the Geophysical Fluid Dynamics Laboratory's Modular Ocean Model (MOM) version of the Bryan-Cox-Semtner ocean model, here used in a 1° by 1° horizontal resolution.

In the vertical there are 66 depth levels, 14 in the top 100 m and 29 in the uppermost 500 m. The maximum depth is 6470 m, and seafloor grid cells assume a fractional size to better represent bathymetry. The sea-ice model is described in detail in Aksenov [2002], its thermodynamics are based on Semtner [1976], and the dynamics on the elastic-viscous-plastic rheology of Hunke and Dukowicz [1997]. OCCAM is forced by surface fluxes of radiative, sensible and latent heat, surface wind stresses, evaporation and precipitation, with a weak relaxation (relaxation time is 30 days) to Levitus monthly sea surface salinity. Relaxing sea surface salinity might act to spuriously sustain the near surface salinity gradient which is being eroded by salt fingering, thereby leading to an overestimation of the salt fingering process, and vice versa in the diffusive layering case. However, comparison of E-P between the control run and the double-diffusive runs discussed below suggests that this effect is very small. The surface fluxes are computed from bulk formulae that take into account the model's actual sea surface temperature and sea ice cover, with atmospheric conditions taken from the 6-hourly NCEP reanalysis products [Large et al., 1997]. Thus, the model can simulate some feedback between the ocean surface and the atmospheric boundary layer and is able to maintain both realistic surface fluxes and sea-surface temperatures.

The biological model is based on the nitrogen-based pelagic ecosystem model of Oschlies [2001] to which carbon and oxygen cycles have been added [Sinha and Yool, 2006; Orr et al., 1999; Najjar and Orr, 1999]. Initial data for nitrate and oxygen were taken from the January fields of the World Ocean Atlas (2001) [Conkright et al., 2002], initial fields for dissolved inorganic carbon (DIC) and alkalinity were derived from GLODAP [Key et al., 2004; Yool and Sinha, 2006]. The oceanic DIC field represents the pre-industrial carbon cycle, with the estimated anthropogenic CO_2 subtracted from the total measured GLODAP DIC data [Key et al., 2004]. Pre-industrial carbon simulations were used here to avoid a long, transient simulation under anthropogenic CO_2 forcing.

Experiments

Three runs were carried out: a "control" run without double diffusion, a run "LMD94" with double diffusion parameterized after Large, McWilliams, and Doney [1994], and a run "ZSH98" with double diffusion parameterized after Zhang, Schmitt, and Huang [1998].

In all experiments, non double-diffusive vertical mixing is parameterized by the K-profile parameterization (KPP, K is the diffusion coefficient) after Large et al. [1994], and described as the superposition of several processes. A background value of $0.1 \times 10^{-4}\,\mathrm{m}^2\,\mathrm{s}^{-1}$, representing the mixing due to internal wave activity, is enhanced depending on the local Richardson number (to represent resolved vertical shear) and on surface wind and buoyancy forcing in the mixed layer. All experiments started from the same spun-up state of the physical model corresponding to 2 January 1989. Then, biogeochemical fields were initialized as described above and the experiments were integrated in coupled biogeochemical-physical mode for 16 model years each. While this is not sufficient to reach steady state for the biogeochemical tracers, drifts in the upper ocean properties were everywhere small compared to the seasonal cycle (averaged annual drift in nitrate is 3.9% of the amplitude of the seasonal cycle, 0.1% for DIC and 1.8% for phytoplankton). The model experiments only differ in whether or not double diffusion is switched on and, if it is, which of the two parameterizations of double-diffusive mixing is used.

2.3.2 Double Diffusion as Function of the Density Ratio

In both parameterizations used here, double-diffusive mixing is parameterized as a function of the density ratio $R_\rho = \frac{\alpha T_Z}{\beta S_Z}$ with thermal expansion coefficient $\alpha = -\frac{1}{\rho}\frac{\delta\rho}{\delta T}$, haline contraction coefficient $\beta = \frac{1}{\rho}\frac{\delta\rho}{\delta S}$, and vertical temperature and salinity gradients $T_Z = \frac{\delta T}{\delta Z}$ and $S_Z = \frac{\delta S}{\delta Z}$, respectively. The density ratio is a measure of the stability of stratification. It describes the relative contributions of the vertical temperature and salinity gradients to the density stratification. The density ratio allows to distinguish different regimes. Two of these are of interest to this study, namely diffusive layering and salt fingering.

Diffusive layering can occur when relatively cold and fresh water overlies warm and salty water, i.e., when the stratification is stable in density ($\alpha T_Z > \beta S_Z$), stable in salt and unstable in temperature ($T_Z < 0$, $S_Z < 0$), hence for a density ratio $0 < R_\rho < 1$. As the molecular diffusivity of salt is about a factor of 100 less than that of temperature, the cold and fresh water directly above the interface will warm faster than it becomes fresh (T and S changes are compared with respect to their impacts on density, αT and βS). Therefore it becomes less dense and rises to a level of its own density. Directly below the interface, the warm and salty water will cool, but largely maintain its salinity, thereby becoming denser. The water will eventually sink to its corresponding density level. As a result, vertical property gradients at the interface are increased.

Salt fingering can occur when relatively warm, salty water overlies colder and fresher water, i.e. when the stratification is stable in density, stable in temperature and unstable in salinity ($\alpha T_Z > 0$, $\beta S_Z > 0$ and $\alpha T_Z > \beta S_Z$). The water above the interface will cool, while largely maintaining its salinity. Thus, it will become denser than the surrounding water and therefore sink until it reaches a level of its own density. The same will happen directly below the interface: water will warm, but remain essentially as fresh as before and hence rise to a level of its own density. These movements occur in long, narrow 'fingers' - that have more or less the scale of human fingers - and the process is accordingly called 'salt fingering'. The net effect of salt fingering is the downward transport of salt across isopycnals and a macroscopic upgradient density flux. The energy required for the mixing is taken out of the salinity stratification. Salt is mixed more effectively than temperature, hence the resulting macroscopic diffusivity of salt is bigger than that of temperature.

Both double-diffusive mixing processes generate so-called staircases in temperature and salinity profiles: nearly homogeneous layers of several meters thickness are separated by thin interfaces with large gradients in both temperature and salinity. These staircases cannot be resolved by the vertical grid of the current model.

2.3.3 Parameterizations

In this Section, the parameterizations are introduced very briefly, for more detail see Figure 2.1 and Appendix 2.7.

Parameterization LMD94 of Double Diffusive Mixing

Double-diffusive mixing is parameterized after Large et al. [1994] in the following way:

(i) Salt Fingering Regime

$$K_s = K_f[1 - (\frac{R_\rho - 1}{R_\rho^0 - 1})^2]^p \text{ for } 1 < R_\rho < R_\rho^0 \tag{2.1}$$

$$K_s = 0.0 \text{ for } R_\rho \geq R_\rho^0 \tag{2.2}$$

$$K_\theta = 0.7 K_s \tag{2.3}$$

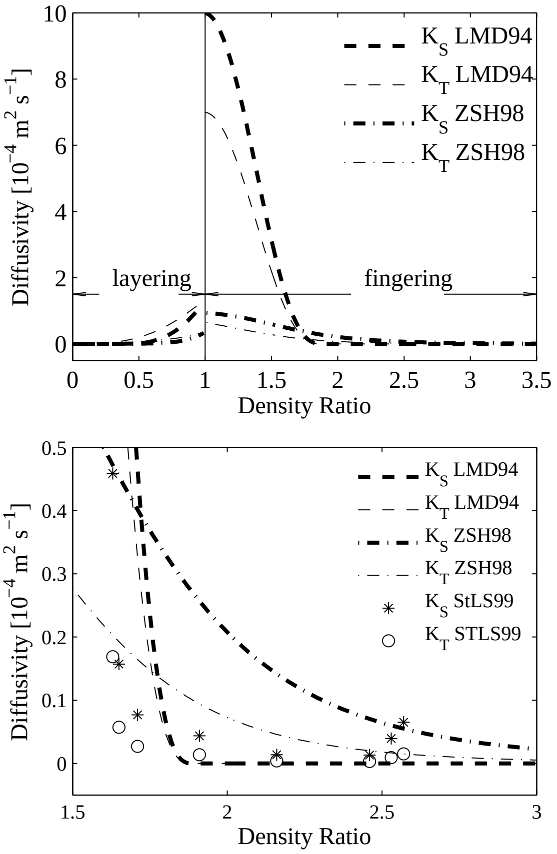

Figure 2.1: Top: Diffusivities due to double diffusion, K$_T$ for temperature and K$_S$ for salinity, as a function of the density ratio $R_\rho = \frac{\alpha T_Z}{\beta S_Z}$. A density ratio between 0 and 1 delineates the diffusive layering regime, a density ratio between 1 and 100 (the ratio of the respective molecular diffusivities of temperature and salinity) the salt fingering regime. In the presence of internal waves, salt finger growth rates can lead to significant salt fingering only for density ratios of O(1). The two parameterizations are LMD94 after Large, McWilliams, and Doney [1994], and ZSH98 after Zhang, Schmitt, and Huang [1998]. Bottom: Extract of the upper panel with a reduced range of density ratios. StLS99 are estimates made in the NATRE experiment described in St. Laurent and Schmitt [1999], K$_S$ and K$_T$ correspond to k$_s$*P$^{(f)}$ and k$_\theta$*P$^{(f)}$ in their notation, respectively, see Section 2.4.

where R_ρ is the density ratio described above, K_s is the diffusivity of salt due to double-diffusive mixing, K_θ is the diffusivity of potential temperature due to double-diffusive mixing, $K_f = 10 \times 10^{-4}\,\mathrm{m}^2\,\mathrm{s}^{-1}$ is the maximum of the diffusivity due to salt fingering, $R_\rho^0 = 1.9$ is the critical density ratio above which mixing due to double diffusion is assumed to be not effective, and $p = 3$.

(ii) Diffusive Layering Regime

$$K_\theta = 0.909 \times exp(4.6 \times exp[-0.54(R_\rho^{-1} - 1)])\nu \tag{2.4}$$

with the molecular viscosity $\nu = 1.5 \times 10^{-6}\,\mathrm{m}^2\,\mathrm{s}^{-1}$. The diffusivity of salt is

$$K_s = K_\theta(1.85 - 0.85R_\rho^{-1})R_\rho \text{ for } 0.5 \leq R_\rho < 1 \tag{2.5}$$

$$K_s = K_\theta 0.15R_\rho \text{ for } R_\rho < 0.5 \tag{2.6}$$

Parameterization ZSH98 of Double-Diffusive Mixing

Double diffusive mixing is parameterized after Zhang et al. [1998] as follows:

(i) Salt Fingering Regime

$$K_S = \frac{R*}{1 + (\frac{R_\rho}{R_c})^n} + K^\infty \tag{2.7}$$

$$K_T = \frac{0.7R*}{R_\rho(1 + (\frac{R_\rho}{R_c})^n)} + K^\infty \quad , \tag{2.8}$$

using $n = 6$, background diffusivity $K^\infty = 5 \times 10^{-6}\,\mathrm{m}^2\,\mathrm{s}^{-1}$, $R* = 10 \times 10^{-4}\,\mathrm{m}^2\,\mathrm{s}^{-1}$, and a critical density ratio $R_c = 1.7$.

(ii) Diffusive Layering Regime

Double-diffusive mixing in the diffusive layering regime is parameterized after Kelley [1990] as:

$$K_T = CRa^{1/3}k_t + K^\infty \tag{2.9}$$

$$K_S = R_F R_\rho(K_T - K^\infty) + K^\infty, \tag{2.10}$$

with the molecular diffusivity of temperature $k_t = 1.4 \times 10^{-7}\,m^2\,s^{-1}$ and

$$C = 0.0032 \times exp(4.8{R_\rho}^{0.72}) \tag{2.11}$$

$$Ra = 0.25 \times 10^9 {R_\rho}^{-1.1} \tag{2.12}$$

$$R_F = \frac{\frac{1}{R_\rho} + 1.4(\frac{1}{R_\rho} - 1)^{3/2}}{1 + 14(\frac{1}{R_\rho} - 1)^{3/2}}. \tag{2.13}$$

In this study, the constant K^∞ is replaced with the value calculated locally from the superposition of internal wave activity, static instability and local shear instability (described above).

2.4 Model Validation at the NATRE site

During the North Atlantic Tracer Release Experiment (NATRE) in 1992, microstructure measurements were taken in an area moderately favorable for salt fingering (approximately 26-31°W, 24-28°N [St. Laurent and Schmitt, 1999]). It was found that mixing by 'ordinary' turbulence was sufficiently strong to prevent the formation of thermohaline staircases. However, optical shadowgraph profiles showed evidence of salt fingers. Considering density ratio and Richardson number, St. Laurent and Schmitt [1999] computed the respective diffusivities of temperature and salt for this moderately salt-finger favorable regime. These were split up into one part due to 'normal' turbulence and a second part due to salt-finger induced mixing, according to

$$K_\theta = P^{(t)} K_0^{(t)} + P^{(f)} K_\theta^{(f)} \tag{2.14}$$

$$K_s = P^{(t)} K_0^{(t)} + P^{(f)} K_s^{(f)} \tag{2.15}$$

with weighting factors $P^{(t)}$ and $P^{(f)}$ for the relative influence of normal mixing and of salt fingering, $P^{(t)} + P^{(f)} = 1$. $K_0^{(t)}$ is the diffusivity estimated by assuming that the observed microstructure is caused entirely by normal mixing, $K_\theta^{(f)}$ and $K_s^{(f)}$ are the diffusivities for temperature and salinity, respectively, estimated by assuming that the microstructure is caused entirely by double diffusion. Since the model simply adds 'normal' and double-diffusive mixing coefficients, we accordingly compare the effective observed $P^{(t)} K_0^{(t)}$ with the model's normal diffusivity, and the observed $P^{(f)} K_{\theta/s}^{(f)}$ with the model's double diffusive mixing coefficients (see Figure 2.1, lower panel, for $P^{(f)} K_{\theta/s}^{(f)}$ as a function of the density ratio). While

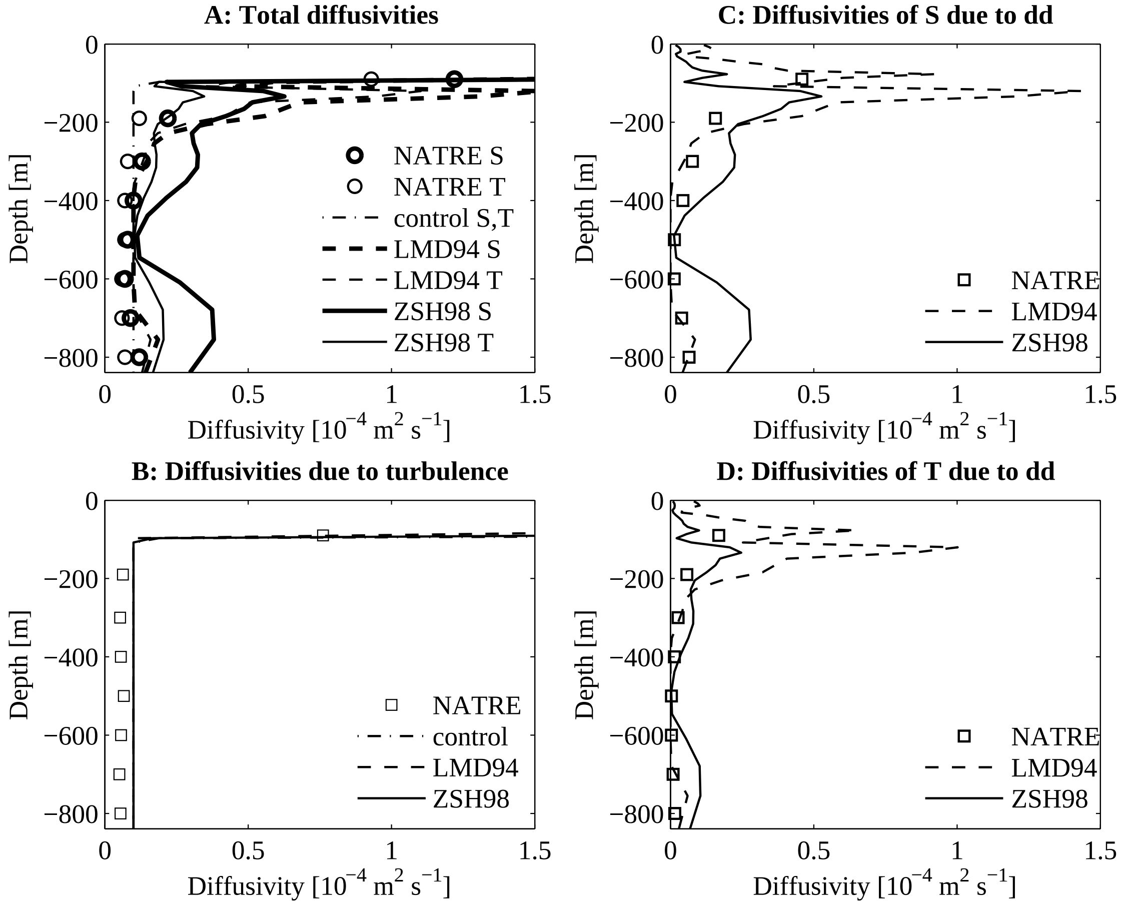

Figure 2.2: Diffusivities at the NATRE site and the respective contributions of normal turbulence and double diffusion. A: Total diffusivities. B: Diffusivities due to turbulence. C: Diffusivities of salinity due to double diffusion. D: Diffusivities of temperature due to double diffusion. NATRE denotes the diffusivities as determined at NATRE, LMD94 and ZSH98 are the parameterizations as described above.

observations were taken in April 1992, we chose to take model results of April 2004 for this comparison, as the model was started only in 1989 from a spun-up state of a model integration without double diffusion, and we wanted to give the model fields as much time as possible to adjust to the new mixing parameterization. However, comparison with other model years yielded similar results (not shown).

As shown by Figure 2.2, the model runs all overestimate the total diffusivities, more so for the diffusivity of salinity than for the diffusivity of temperature. This already happens for the control run which, in depths greater than the mixed layer depths (in this case approximately 100 m), only uses the background value of $0.1 \times 10^{-4}\,\mathrm{m}^2\,\mathrm{s}^{-1}$ (see Figure 2.2 B). Consequently, the double-diffusive runs with additional diffusivities due to double diffusion, overestimate the diffusivities obtained at the NATRE experiment even more (see Figure 2.2 A).

Still, the general shape of the diffusivity profile is reproduced by the model: all three runs show enhanced mixing in the mixed layer, and the double-diffusive runs show increasing diffusivities below a minimum at about 500 m. Model run LMD94 has the upper peak in diffusivities due to double diffusion for salinity and temperature too deep in the water column, and it overestimates diffusivities below 600 m and underestimates in between. Run ZSH98 fits observed diffusivities well in the lower part and underestimates the upper peak (see Figure 2.2 C and D).

Differences between the modeled and the measured diffusivities are caused both by an imperfect parameterization of (double-diffusive) mixing as well as by difficulties of the model to reproduce the temperature and salinity stratification.

Applying the parameterizations LMD94 and ZSH98 to the density ratios measured at NATRE (instead of the density ratios simulated by the model) yield root-mean-square deviations from the observational estimates of the double-diffusive parts of the diffusivities of $0.5\times10^{-4}\mathrm{m}^2\,\mathrm{s}^{-1}$ (K_S LMD94), $0.2\times10^{-4}\mathrm{m}^2\,\mathrm{s}^{-1}$ (K_S ZSH98), $0.4\times10^{-4}\mathrm{m}^2\,\mathrm{s}^{-1}$ (K_T LMD94), and $0.1\times10^{-4}\mathrm{m}^2\,\mathrm{s}^{-1}$ (K_T ZSH98), respectively. This suggests a slight advantage of the ZSH98 parameterization. The difference between the total diffusivities of T and S compared as above are $0.1 \times 10^{-4} m^2\, s^{-1}$ for both parameterizations (computed all for the eight measurements in the depth range 90 m to 800 m). In comparison with NATRE data, ZSH98 does a better job in reproducing the diffusivity profiles (see Figure 2.2).

2.5 Results and discussion

2.5.1 Physics

In this Section, changes between the double-diffusive runs and the control run are investigated with focus on physical upper ocean quantities that are potentially relevant for climate models. The regions in which double-diffusive mixing occurs in the model match those derived from observations described above: The model correctly reproduces salt fingering below, and the diffusive layering above, the Mediterranean outflow (see Figure 2.3). However, especially for the salt fingering regime, the extent of regions in which double-diffusive mixing is active differs between the runs - LMD94 cuts off at a lower density ratio than ZSH98, hence ZSH98 tends to display double diffusion at larger regions.

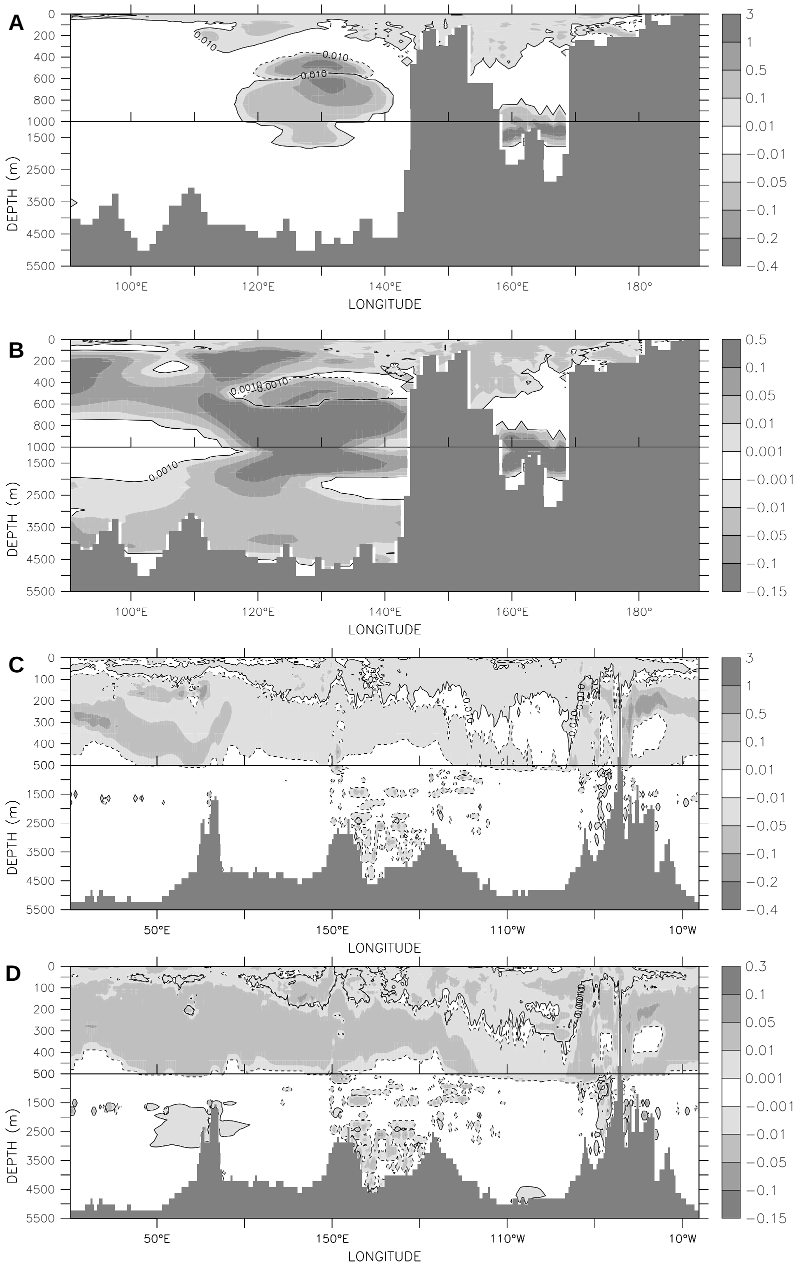

Figure 2.3: Differences between the diffusivity of salt and the diffusivity of temperature in $cm^2\,s^{-1}$ for the year 2004 for a north-south section (Panel A and B) and a section at 60°S (Panel C and D), both sections shown in Figure 2.5, Panel A, for LMD94 (Panels A and C) and ZSH98 (Panels B and D). Contours are drawn at 0.01 $cm^2\,s^{-1}$ (LMD94, solid), -0.01 $cm^2\,s^{-1}$ (LMD94, dashed), 0.001 $cm^2\,s^{-1}$ (ZSH98, solid), -0.001 $cm^2\,s^{-1}$ (ZSH98, dashed).

In the pycnocline, salt fingering is generally strongest in subtropical regions, and diffusive layering is strongest in seasonally ice covered areas, again in agreement with observations.

In the upper ocean, the spatial patterns of the different regimes show some annual cycle, particularly close to the seasonally varying sea ice edge which tends to separate diffusive layering and salt fingering regimes. The regions with most active near-surface salt fingering also move with the seasons from one winter hemisphere to the other. At a given station located in the subtropical salt-fingering regime, double-diffusive mixing usually sets in at the bottom of the mixed layer in autumn when the winter mixed layer is about to reach its maximum depth. Over the next few months the region over which double diffusion is active spreads both upwards and downwards until a maximum intensity and a maximum vertical extent of double-diffusive mixing are reached. The depth of maximum salt fingering in spring is typically a couple of tens to a hundred meters deeper than the depth at which double diffusion set in in autumn. The annual cycle of diffusivities at a typical subtropical site (the NATRE region) is shown in Figure 2.4.

As a result of the annual cycle in salt fingering, the impact of double diffusion on air-sea heat fluxes is largest at the end of winter. Although the intensity of double diffusive mixing usually reaches its maximum only later in the year, this maximum occurs well below the surface mixed layer and thus does not have immediate contact with the atmosphere. Consequently, the impact of double diffusion on surface fluxes (not only of heat but also of gases, see below) is generally bigger in the respective winter hemisphere than in the summer hemisphere (Figure 2.5). Typical values for the zonally and seasonally averaged changes in the simulated surface heat flux due to double diffusion are $0.1\,\mathrm{W\,m^{-2}}$ in the winter hemisphere and an order of magnitude less in the summer hemisphere.

Local effects of double diffusion on surface heat fluxes through changes in SST are in the range of $\pm\, 30\,\mathrm{W\,m^{-2}}$. The maximum values are reached only at a few isolated grid points in the Bering Strait and at the ice edge near Antarctica, and result from small changes in the ice coverage mentioned above. As shown in Figure 2.5, systematic larger-scale impacts occur in the subtropical and the subpolar regions prone to near-surface salt-finger activity: As salt fingers transport both heat and salt downwards, the sea surface is cooled and the heat loss to the atmosphere is reduced, enhancing the large-scale net heat flux into the ocean by typically 0.05 to $0.1\,\mathrm{W\,m^{-2}}$. Somewhat larger changes are found in the Gulf Stream and Kuroshio

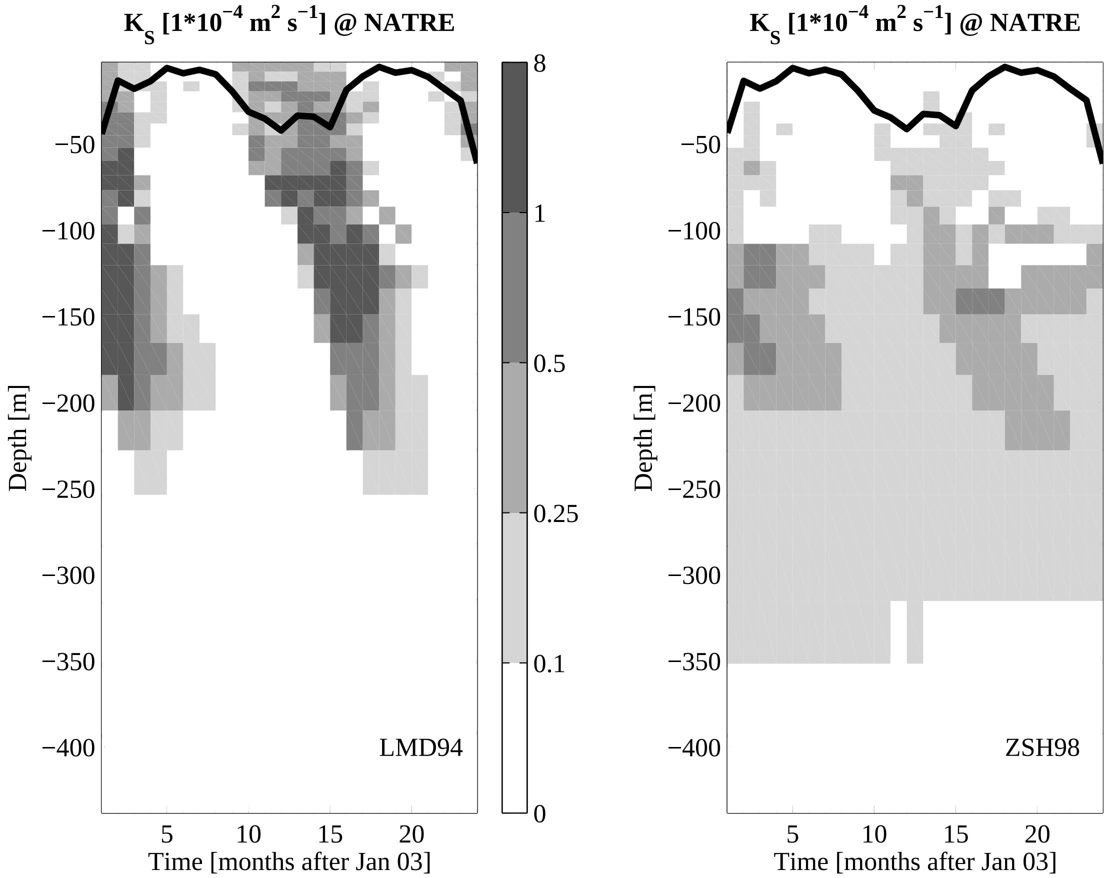

Figure 2.4: Annual cycle of diffusivities [10^{-4}m^2 s^{-1}] against depth [m] at the NATRE site. Red line indicates the monthly mean mixed layer depth as given by KPP.

regions, with magnitude ± 10 W m^{-2} for run ZSH98 and ± 5 W m^{-2} for run LMD94 (± depending on the side of the front). In these areas of strong lateral gradients in SST, even small changes in circulation patterns can have a large local effect on air-sea heat fluxes. Given that typical surface heat fluxes in these western boundary-current regions can reach several hundred W m^{-2}, the modifications induced by double diffusion are relatively small.

The locally enhanced impacts of double-diffusion on air-sea heat exchange in the southern part of the Indian Ocean result from a small phase shift in a slowly moving wave, probably related to an interaction of basin scale atmospheric forcing with eastern boundary processes (Birol and Morrow [2001]).

Near-surface double diffusion also affects sea surface salinity, although this effect may be underestimated in the model because of the sea surface salinity relaxation

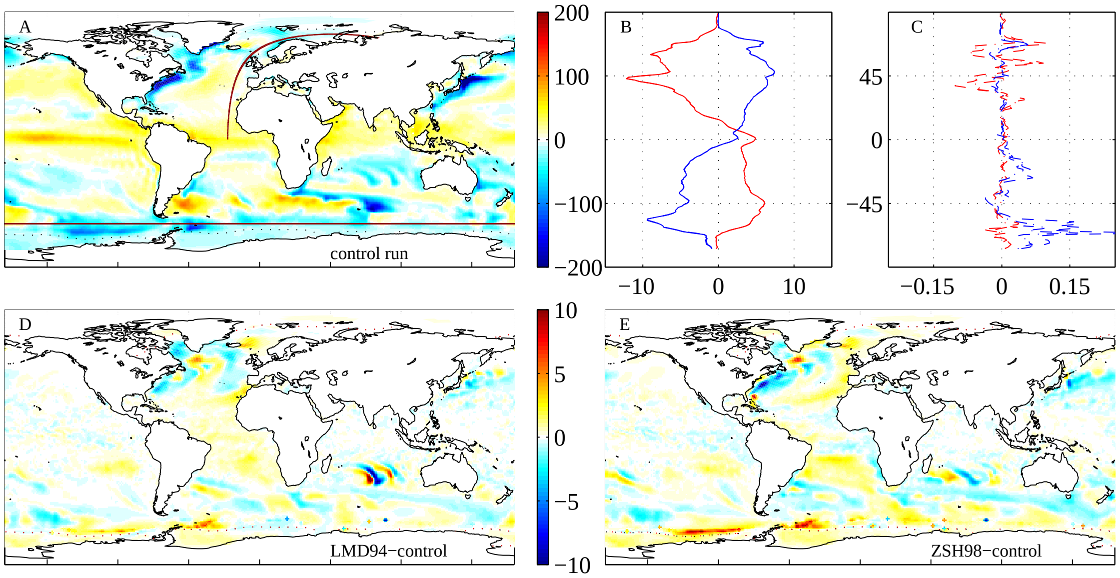

Figure 2.5: Simulated annual mean air-to-sea heat flux and contour of 90 % sea-ice coverage (dotted line) of the control run (Panel A, drawn in red are the sections which are shown in Figure 2.3). Zonal mean heat flux for January to March (red) and July to August (blue) for the control run (Panel B). Difference of the zonal mean heat flux for January to March (red) and July to August (blue) for control-LMD94 (dashed line) and control-ZSH98 (dashed-dotted line) (Panel C). Difference between the double-diffusive runs and the control run (LMD94-control: Panel D, ZSH98-control: Panel E) in heat fluxes and contour of 90 % ice coverage in the control run (black dotted line) and in the double-diffusive run (red dotted line). All plots in $[W\,m^{-2}]$.

mentioned above. Changes between the runs are mainly a freshening of the sea surface for the double-diffusive runs, resulting from the net downward flux of salt by double diffusion. Via the surface salinity relaxation condition, this leads to a decreased freshwater flux into the ocean. Run LMD94 receives about 21 mm yr^{-1} less freshwater in the annual mean 2004 than the control run. For ZSH98 the decrease is approximately 42 mm yr^{-1}. For reference, the control run receives 611 mm yr^{-1} freshwater, thereof 225.3 mm yr^{-1} via the sea surface salinity (SSS) relaxation.

Changes in the modeled sea-ice fields are potentially important because they may have a big impact on the modeled surface albedo and surface heat fluxes. Our experiments show that changes in ice fields due to double diffusion are very small, the ice cover is enhanced compared to the control run (average increase over the simulated year 2004: ZSH98 southern hemisphere 0.8 %, northern hemisphere 0.1 %; LMD94 southern hemisphere 0.3 %, northern hemisphere 0.1 %).

For completeness we note that in our model runs, the inclusion of double diffusion has little impact on the depth of the surface mixed layers, with changes always far smaller than the thickness of a grid box. Furthermore, double diffusion has no significant impact on the mean circulation, including the meridional overturning circulation, within the 16 years we ran our models for. For a complete assessment of large-scale circulation changes much longer runs would be required.

2.5.2 Primary production and nutrient supply

In general, relative changes due to double diffusion are much larger for the simulated biogeochemical properties compared to the physical properties discussed above. Simulated primary production is enhanced by double-diffusive mixing in most regions. The strongest increase in regional primary production by more than 120 % for ZSH98 and 80 % for LMD94 can be found in the subtropical Atlantic, where double-diffusive mixing acts strongly at the depth of the nutricline (Figure 2.7).

Nitrate supply into the upper 127 m occurs mainly around 40°N and 40°S and in upwelling areas. In low-latitude and Southern-Ocean upwelling areas, this happens partly via vertical advection whereas the largest part of the supply in mid latitudes is due to convection in autumn and winter. The largest changes between the double-diffusive runs and the control run occur in the Atlantic at 20°N and between 10 and 30°S, and at 20°S off South America in the Pacific. In these regions, double diffusion alters the stratification such that convection becomes slightly deeper than in the control run.

Surface nitrate concentrations of the normal run overall compare well with nitrate documented in World Ocean Atlas by Levitus [1994]. However, the model tends to underestimate concentrations in the subtropics and tropics. These are the regions where double diffusion brings up nutrients into the eutrophic zone, however not enough to match the world ocean atlas (at least not at the surface). The model overestimates nitrate concentrations in the Arctic, but this feature is overemphazized by the map projection.

On the global average, nitrate supply into the upper 127 m increases by 0.001 mol N $\mathrm{m^{-2}\,yr^{-1}}$ on switching from the control run to experiment LMD94, and 0.006 mol N $\mathrm{m^{-2}\,yr^{-1}}$ when switching from control to experiment ZSH98. In both cases, most of this additional supply occurs in mid latitudes. These results are consistent with those reported by Oschlies et al. [2003], who found typical fluxes of 0.03 mol N $\mathrm{m^{-2}\,yr^{-1}}$ due to salt fingering instabilities in the subtropical North At-

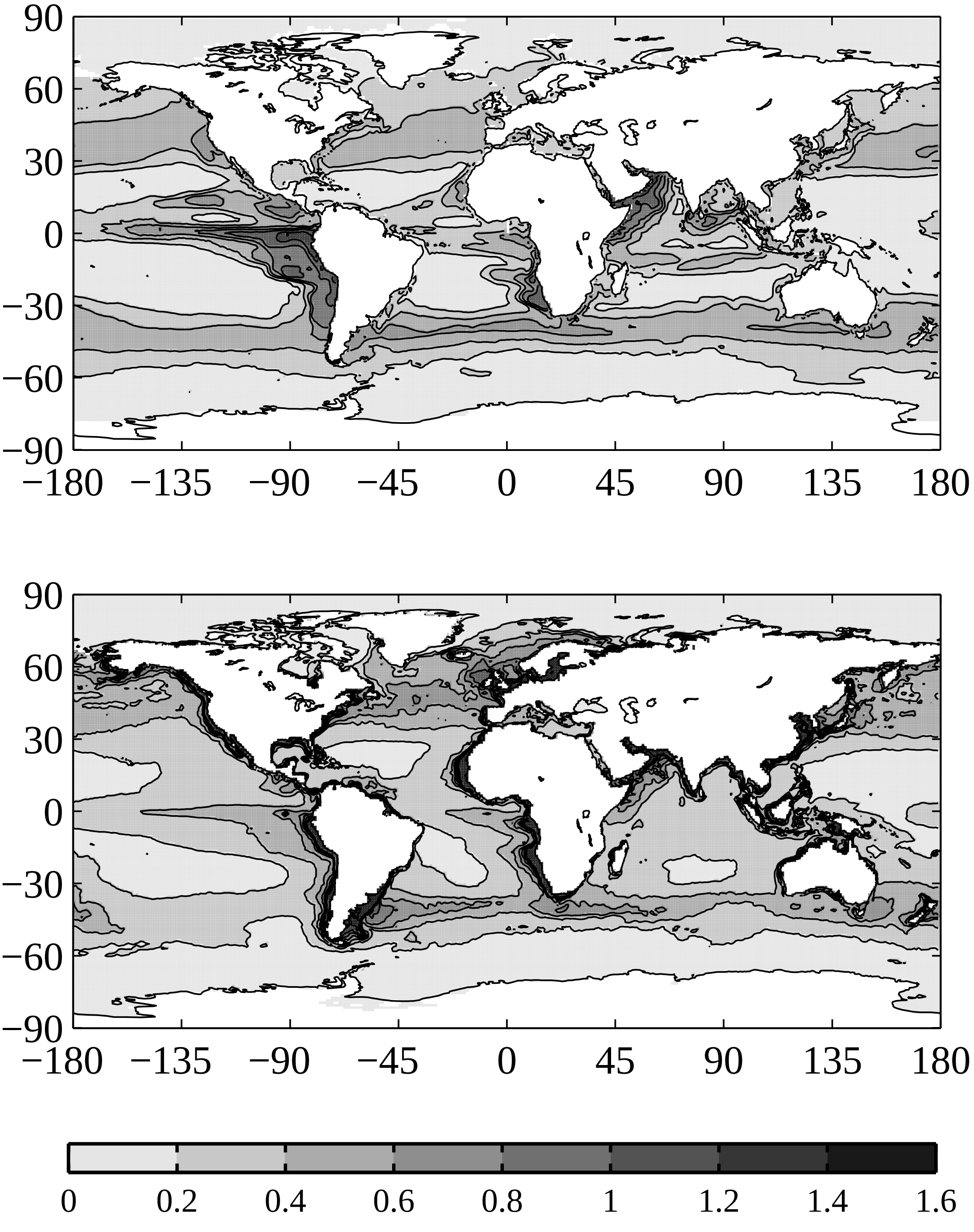

Figure 2.6: Comparison of annual mean integrated production [$\mathrm{g\,C\,m^{-2}\,d^{-1}}$] as modeled in the reference run (upper panel) and annual mean integrated production after Behrenfeld and Falkowski [1997] (lower panel).

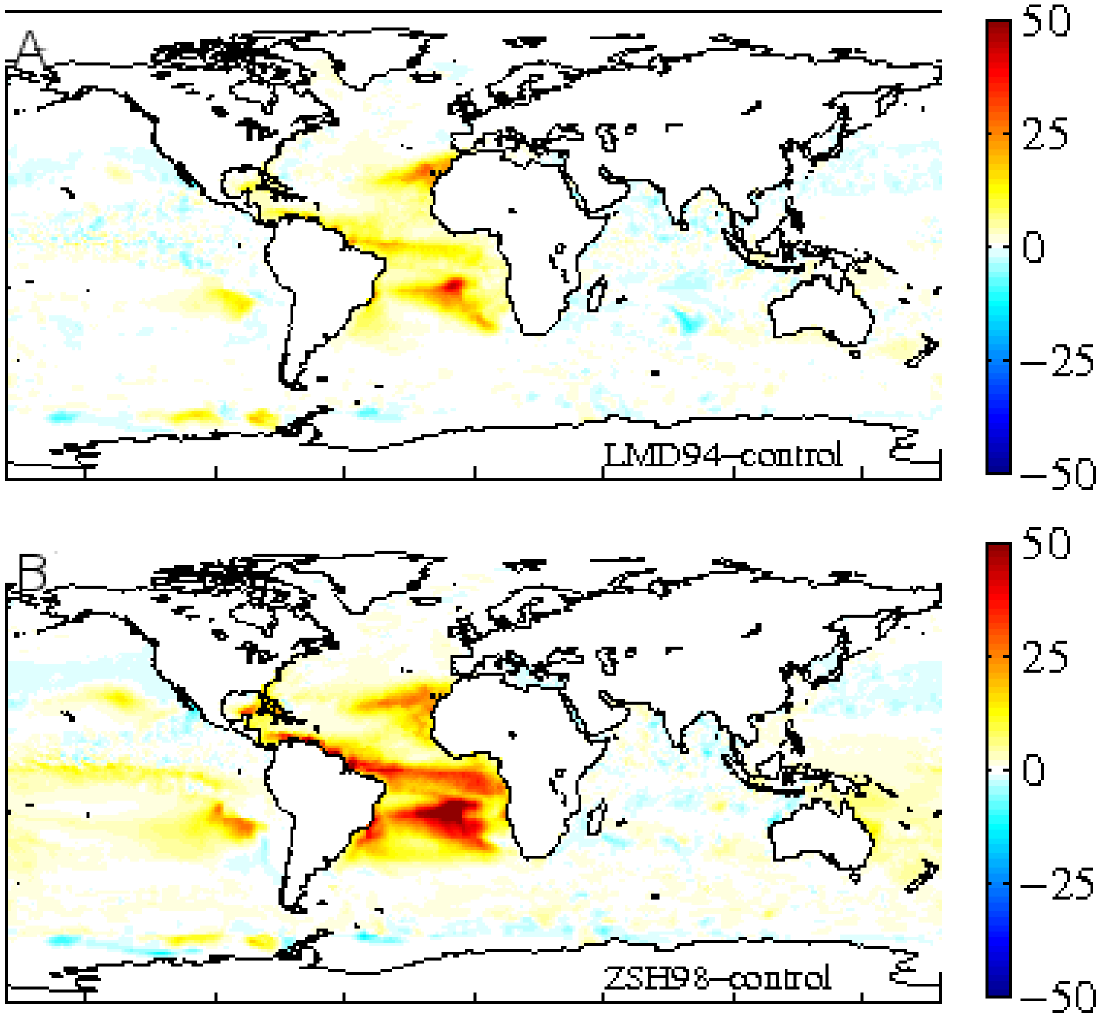

Figure 2.7: Difference between the double-diffusive runs and the control run (LMD94-control: Panel A, ZSH98-control: Panel B) in production. All plots in [$\mathrm{g\,C\,m^{-2}\,yr^{-1}}$].

lantic. For the same region, our experiments yield $0.02\,\mathrm{mol\,N\,m^{-2}\,yr^{-1}}$ more uptake for MD94 and $0.04\,\mathrm{mol\,N\,m^{-2}\,yr^{-1}}$ for ZSH98.

2.5.3 Surface fluxes of CO_2 and O_2

After less than two decades of spin up, the model's oceanic carbon inventory is not in complete equilibrium, and the ocean is outgassing CO_2 to the atmosphere (kept at constant, pre-industrial pCO_2 of 278 ppm). The annual CO_2 sea-to-air flux for the control run is $8.3\,\mathrm{g\,C\,m^{-2}\,yr^{-1}}$, whereas for the double-diffusive runs outgassing is reduced to $7.9\,\mathrm{g\,C\,m^{-2}\,yr^{-1}}$. Initially we suspected that the additional CO_2 up-

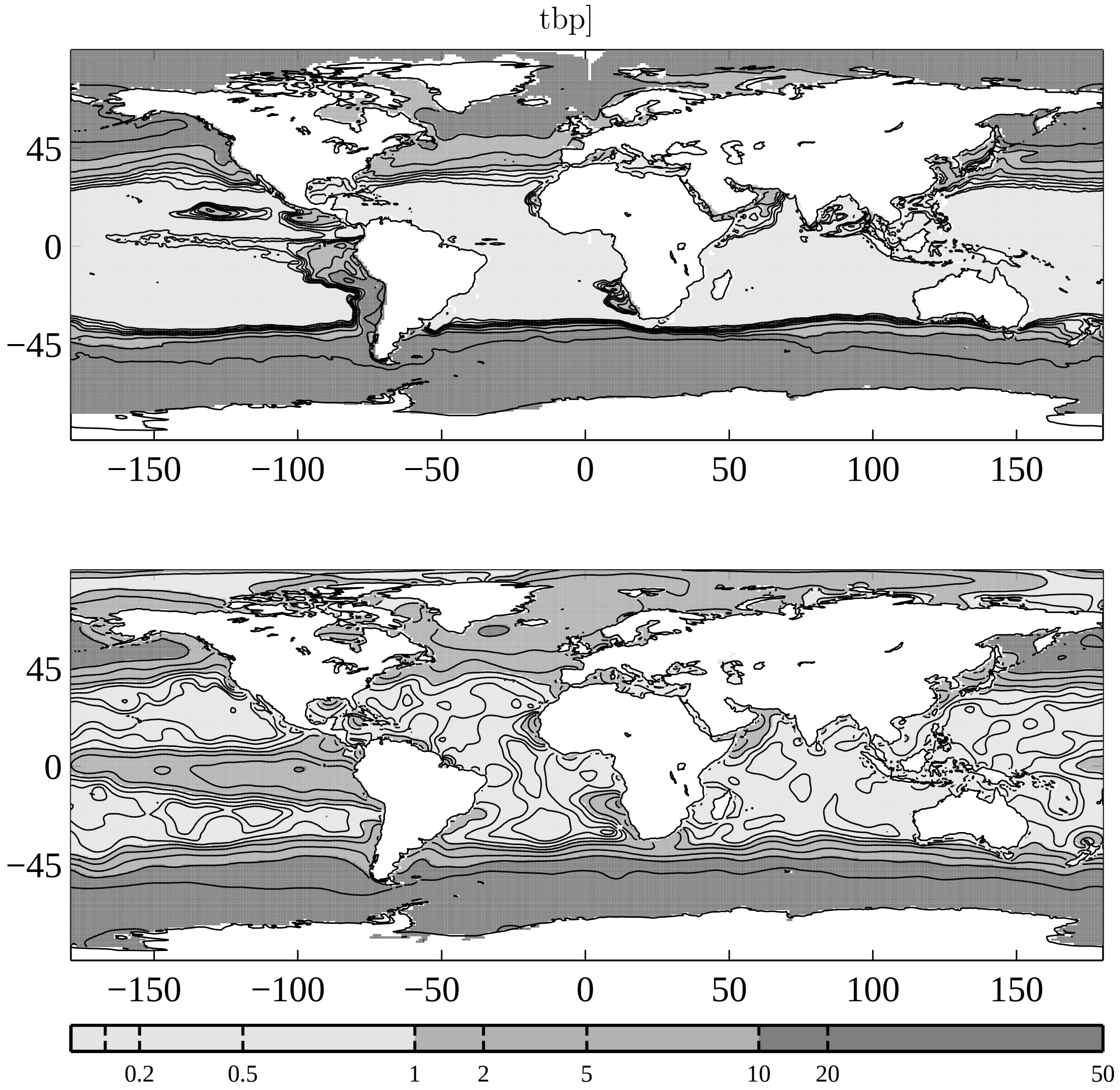

Figure 2.8: Comparison of nitrate [mmol N m^{-3}] in the control run (upper panel) and in World Ocean Atlas by Levitus [1994] (lower panel).

take in the double diffusive run was occurring in the subtropics, where primary production is enhanced by double-diffusive mixing and where surface temperatures are reduced by the action of double diffusion. Thus, both enhanced biotic uptake of CO_2 and the enhanced gas solubility in colder surface waters act to increase oceanic CO_2 uptake. However, as shown in Figure 2.9, the double diffusive runs instead show enhanced outgassing in the subtropics. To understand this unexpected behavior, we investigate the changes in oceanic pCO_2 as a function of temperature, salinity, the DIC concentration and alkalinity. Total pCO_2 changes are partitioned into contributions from changes in surface salinity, temperature and DIC according

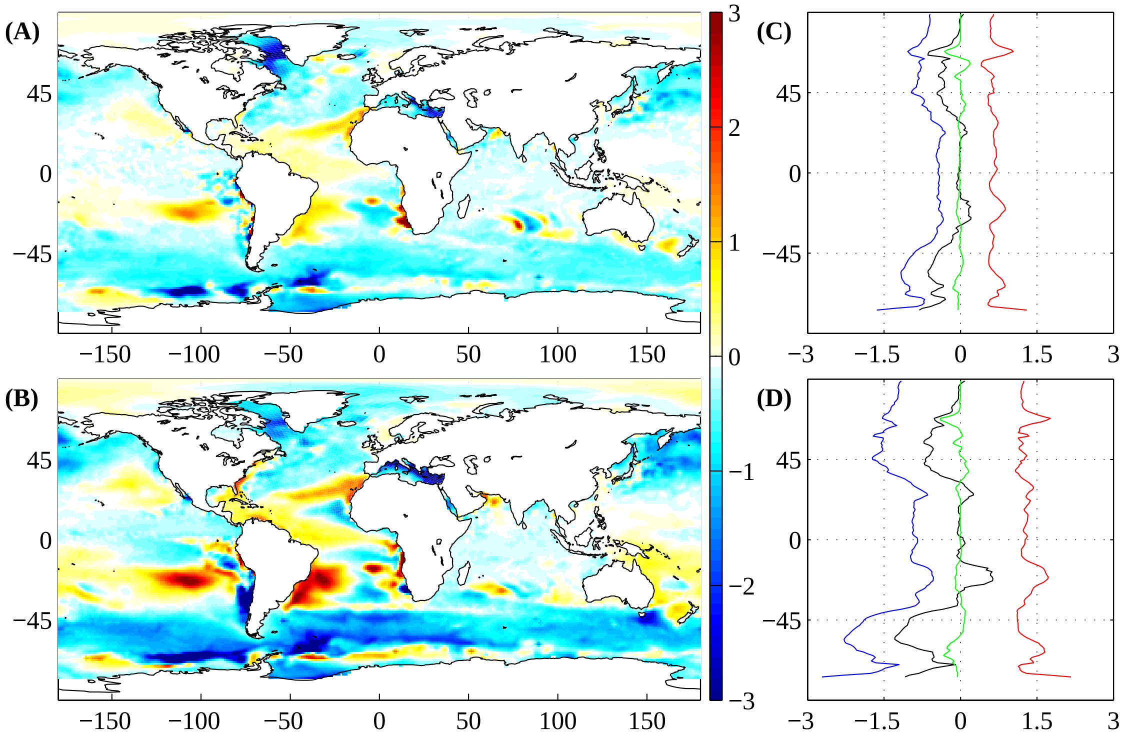

Figure 2.9: Differences in simulated surface pCO$_2$ between double-diffusive run and control run (Plot A: LMD94-control. Plot B: ZSH98-control) and zonal mean of the partitions of the influence of T, S and DIC to the total pCO$_2$ difference calculated from $\Delta pCO_2 = \frac{\delta pCO_2}{\delta S}\Delta S + \frac{\delta pCO_2}{\delta T}\Delta T + \frac{\delta pCO_2}{\delta DIC}\Delta DIC + o(\Delta^2)$ after Eden and Oschlies [2006]. Black line: ΔpCO_2, green line: $\frac{\delta pCO_2}{\delta T}\Delta T$, red line: $\frac{\delta pCO_2}{\delta S}\Delta S$ and blue line: $\frac{\delta pCO_2}{\delta DIC}\Delta DIC$ for LMD94-control (plot C) and ZSH98-control (plot D).

to

$$\Delta pCO_2 = \frac{\delta pCO_2}{\delta S}\Delta S + \frac{\delta pCO_2}{\delta T}\Delta T + \frac{\delta pCO_2}{\delta DIC}\Delta DIC + o(\Delta^2). \tag{2.16}$$

where ΔpCO_2, ΔS, ΔT and ΔDIC represent the difference of pCO$_2$, surface salinity, surface temperature, and surface DIC between double diffusive run and control run, respectively, and $o(\Delta^2)$ represents terms of second and higher orders in the perturbed quantities. The partial derivatives are taken as $\frac{\delta pCO_2}{\delta T} \approx 10\,\mathrm{ppm\,K^{-1}}$, $\frac{\delta pCO_2}{\delta DIC} \approx 1\,\mathrm{ppm\,mmol^{-1}\,m^3}$ and $\frac{\delta pCO_2}{\delta S} \approx$ -60 ppm psu^{-1} (e.g., Eden and Oschlies [2006]). The differences in surface temperature between the double diffusive runs and the control run vary regionally. In the zonal mean, the strongest feature are a cooling at about 60°N/S, a cooling around 20°N/S and a warming at about 45°N/S. However, these changes in surface temperature have only a relatively small effect on changes in pCO_2. As shown in Figure 2.9, the changes in pCO_2 due to changes in salinity and DIC are much larger, and rather than oscillating around zero they are distinctly positive for salinity and distinctly negative for DIC. Sea surface salinity is lower almost everywhere in the double diffusive runs than in the control run. A lower salinity, in the model, corresponds to lower alkalinity and hence higher pCO_2.

In our model, the negative ΔS is mirrored in the P-E relaxation: Restoring SSS to Levitus leads to artificial changes in P-E in response to double-diffusive mixing, whereas such a feedback does not exist in reality. Less freshwater (equivalent to more salt) is added to the double diffusive runs compared to the control run. Thereby restoring SSSs weakens differences in SSS (which translate to differences in alkalinity) between the runs. This challenges the ΔpCO_2 derived in this study. If it was not for the relaxation, ΔS would be bigger than it is now, therefore the influence of the difference in salinity (and alkalinity) might be even larger compared to the other two terms, and the model ocean might release even more CO_2 to the atmosphere once double-diffusive mixing is accounted for. Additionally restoring prevents the salinity stratification from erosion by double-diffusive fluxes and thereby tampers with the double-diffusive potential of the stratification. The SSS relaxation influences alkalinity even though in this model alkalinity is a prognostic tracer, only linked to salinity through the P-E fluxes, because the relaxation is achieved through surface freshwater fluxes.

ΔDIC is negative almost everywhere, too. Because pCO_2 decreases with decreasing DIC, the changes in surface DIC and surface salinity tend to oppose each other. Compared to the effects of salinity changes, changes in the photosynthetical drawdown of DIC are small in the subtropics. On the other hand, the subpolar and polar decreases of pCO_2 in the double-diffusive runs are mostly due to the changes in surface DIC. As in the subtropics, salinity changes act to counteract the ΔDIC-related pCO_2 reduction but, in contrast to the subtropics, has a smaller magnitude (see Figure 2.9).

Annual O_2 air-sea fluxes of our model runs compare well with those simulated by Bopp et al. [2002]. Oceanic O_2 uptake is reduced almost everywhere in the double diffusive runs compared to the control run (approximately $0.2\,\mathrm{mol\,m^{-2}\,yr^{-1}}$) despite lower SSTs which should lead to more O_2 being taken up. This can be explained by the higher biological productivity (more photosynthesis, hence more production of O_2) In contrast to CO_2, oxygen does not react with seawater, but instead dissolves in it. As such, it is unaffected by changes in surface alkalinity and carbonate chemistry, although there is a small salinity effect on oxygen saturation.

2.6 Summary

Two different parameterizations of double-diffusive mixing, ZDH98 and LMD94, have been applied to a global ocean ecosystem-circulation model. Both parameterizations formulate double-diffusive mixing in terms of the density ratio, although mixing intensities and the ranges of relevant density ratios differ considerably (Figure 2.1). When applied to density ratios measured at NATRE, modeled diffusivities are closer to observational estimates for ZSH98 than for LMD94. This suggests that ZSH98 is a more realistic description of double diffusive mixing than is LMD94.

A recent update of the LMD94 parameterization [Danabasoglu et al., 2006], which uses a higher cut-off density ratio and a lower maximum diffusivity, produces diffusivities closer to those of ZSH98. We did not include this update in our intercomparison directed at the sensitivity of model results to different parameterizations because the updated parameterization appears to lie between LMD94 and ZSH98.

Differences between the double-diffusive runs and the control run are almost always larger for ZSH98 than for LMD94. This happens because ZSH98 applies the parameterization of double diffusion to a larger range of density ratios than LMD94 does and hence simulates non-zero salt-finger-related diffusivities over larger parts of the ocean (Figure 2.3). The fact that diffusivities of LMD94 are up to a factor 10 higher than ZSH98 for density ratios close to 1 has only limited effect in the current model. This might be related to the still relatively coarse vertical grid that does not resolve sharp vertical property gradients and may hence influence how often situations with a density ratio close to 1 occur.

The results of our study suggest only limited effect of double diffusion on physical upper ocean properties, though our decadal-scale simulations do not enable us to rule out longer-term changes in the ocean circulation as have been reported for some models [Merryfield et al., 1999; Zhang and Schmitt, 2000]. In our model, the changes in heat fluxes between the double-diffusive runs and the control run turn out to be more than an order of magnitude smaller than the fluxes associated with the current anthropogenic greenhouse effect which are thought to be of the order of $2.5\,\mathrm{W\,m^{-2}}$ [Soon et al., 2000]. The most dramatic effects of including double diffusive mixing were found for the marine biology and biogeochemistry. Primary production shows regional enhancements by some 100% over large areas of the oligotrophic subtropical gyres. Global enhancement is much smaller, about 1% for LMD94 and 3% for ZSH98, because the large relative enhancement takes place mostly in low-productivity regions. Simulated CO_2 uptake of the ocean is enhanced by about $0.14\,\mathrm{Gt\,C\,yr^{-1}}$ in the double diffusive runs. This is about 7 % of the anthropogenic CO_2 signal (which is approximately $2\,\mathrm{Gt\,C\,yr^{-1}}$ according to Sarmiento and Sundquist [1992]; Takahashi et al. [2002]).

The climate sensitivity of double-diffusive mixing differs from that of ‘ordinary’ mixing processes as, for example, mixing due to internal waves. Whereas in the case of ‘ordinary’ mixing processes the intensity of mixing depends on the stability of the density stratification, double-diffusive mixing is thought to be a function of the density ratio, i.e., of the relative contributions of the vertical temperature and salinity gradients to the vertical density profile. As it is likely that global warming will lead to changes in the proportion of ‘ordinary’ mixing to double-diffusive mixing [Oschlies et al., 2003], estimates of future climate change will benefit from a better quantitative understanding of double-diffusive mixing.

Although this modeling study cannot yield a definite conclusion about which parameterization is more realistic, the influence of double-diffusive mixing on upper-ocean properties should be kept in mind (if not accounted for) in long climate-study runs. The main result of this study is that our mechanistic understanding of mixing processes, and their parameterizations in ocean circulation models, are not yet satisfactory. Implementing a small-scale and supposedly unimportant mixing process showed that tiny changes in mixing can have global impacts, particularly on the upper ocean biology which reacts in a highly non-linear way to changes in nutrient supply. A better understanding of mixing processes (including, but not limited to, double diffusion) is important in order for models to accurately simulate real-world behavior – including that caused by anthropogenically-driven climate change.

2.7 Appendix: Parameterizations of Double-Diffusive Mixing

2.7.1 Parameterization LMD94 of Double-Diffusive Mixing

Double-Diffusive Mixing in the Salt Fingering Regime

Double-diffusive mixing in the salt fingering regime is parameterized following an analysis of limited observational data by Schmitt [1981, 1988]. Mixing is found to be at background levels (about $10^{-5}\,\mathrm{m^2\,s^{-1}}$) for $R_\rho > 1.9$, then rapidly increasing near $R_\rho = 1.7$ and to be large for $R_\rho < 1.5$ (about $10^{-3}\,\mathrm{m^2\,s^{-1}}$). Mixing of temperature is found to behave in a similar fashion, but to be less intense at the same density ratio. A curve fit leads to the following equations

$$K_s = K_f[1 - (\frac{R_\rho - 1}{R_\rho^0 - 1})^2]^p \text{ for } 1 < R_\rho < R_\rho^0 \tag{2.17}$$

$$K_s = 0.0 \text{ for } R_\rho \geq R_\rho^0 \tag{2.18}$$

$$K_\theta = 0.7 K_s \tag{2.19}$$

where K_s is the diffusivity of salinity due to double-diffusive mixing, K_θ is the diffusivity of potential temperature due to double-diffusive mixing, K_f=10*$10^{-4}\,\mathrm{m^2\,s^{-1}}$ is the maximum of the diffusivity due to salt fingering, $R_\rho^0 = 1.9$ is the critical density ratio above which mixing due to double diffusion is assumed to be not effective any more, and $p = 3$. The diffusivity of salt is computed indirectly by applying a laboratory flux law to observed salinity steps in staircase regions and then dividing by the mean salinity gradient. However, laboratory flux laws are not necessarily valid in the open ocean because of, for example, background internal wave fields which are present in the ocean but difficult to reproduce in the laboratory [Gargett, 1989; Kelley et al., 2003].

Double-Diffusive Mixing in the Diffusive Layering Regime

Double-diffusive mixing of temperature in the diffusive layering regime is parameterized after Large et al. [1994] as

$$K_\theta = 0.909 * exp(4.6 * exp[-0.54(R_\rho^{-1} - 1)])\nu \tag{2.20}$$

with the molecular viscosity $\nu = 1.5{*}10^{-6}\,\mathrm{m^2\,s^{-1}}$. The diffusivity of salt is

$$K_s = K_\theta(1.85 - 0.85R_\rho^{-1})R_\rho \text{ for } 0.5 \leq R_\rho < 1 \tag{2.21}$$

$$K_s = K_\theta 0.15R_\rho \text{ for } R_\rho < 0.5 \tag{2.22}$$

This parameterization goes back to tank experiments and theoretical considerations as well as dimensional arguments [Turner, 1965; Fedorov, 1988; Marmorino and Caldwell, 1978; Huppert, 1971]. According to Large et al. [1994], the sequence of subroutine calls in the model code was such that double diffusion was called before the mixed layer mixing was calculated. The order of calls was changed here, such that double diffusion is now called at the end. Therefore the "normal" mixing can be clearly distinguished from the additional mixing due to double diffusion.

2.7.2 Parameterization ZSH98 of Double-Diffusive Mixing

Double-Diffusive Mixing in the Salt Fingering Regime

The effective diffusivities for temperature and salinity, R_T and R_S, are parameterized by Zhang et al. [1998], as:

$$K_S = \frac{R*}{1 + (\frac{R_\rho}{R_c})^n)} + K^\infty \tag{2.23}$$

$$K_T = \frac{0.7R*}{R_\rho(1 + (\frac{R_\rho}{R_c})^n)} + K^\infty \tag{2.24}$$

This parameterization is quoted from Schmitt [1981] who used the slightly different relation $K_T = \frac{0.7}{R_\rho}R_K$, with R* = $10{\times}10^{-4}\,\mathrm{m^2\,s^{-1}}$. In the present study we will employ the Zhang et al. [1998] parameterization, using different values than originally proposed by Schmitt [1981], "reflecting improved understanding of fluxes in the thermohaline staircases observed in the C-SALT program" [Schmitt, 1988]: $n = 6$, background diffusivity $K^\infty = 5 \times 10^{-6}\,\mathrm{m^2\,s^{-1}}$ and a critical density ratio $R_c = 1.7$. The intensity of salt-finger convection is described as a strong function of R_ρ. This formulation of the diffusivities was chosen because of the simple specification of a cut-off R_ρ and the ability to make the cut-off as sharp as desired (by increasing n). This pragmatic parameterization has "no theoretical basis whatsoever" [Schmitt, 1981], it only allows to reproduce the apparent dependence of the diffusivities on R_ρ suggested by the application of laboratory flux laws to oceanic fine structure data.

Double-Diffusive Mixing in the Diffusive Layering Regime

Double-diffusive mixing in the diffusive layering regime is parameterized after Kelley [1990]. K_T and K_S are described as:

$$K_T = CRa^{1/3}k_t \tag{2.25}$$

$$K_S = R_F R_\rho K_T \tag{2.26}$$

with the molecular diffusivity of temperature $k_t = 1.4\,\times\,10^{-7}\,\mathrm{m}^2\,\mathrm{s}^{-1}$ and

$$C = 0.0032 \times exp(4.8{R_\rho}^{0.72}) \tag{2.27}$$

$$Ra = 0.25 \times 10^9 {R_\rho}^{-1.1} \tag{2.28}$$

$$R_F = \frac{\frac{1}{R_\rho} + 1.4(\frac{1}{R_\rho} - 1)^{3/2}}{1 + 14(\frac{1}{R_\rho} - 1)^{3/2}}. \tag{2.29}$$

This is the same as used by Kelley [1984], apart from new formulations of C and R_F which were fitted to the whole collection of laboratory measurements available at that time. Zhang et al. [1998] included diffusivities unrelated to double-diffusive mixing, K^∞ to the formulation above, modifying equations 2.25 and 2.26 to

$$K_T = CRa^{1/3}k_t + K^\infty \tag{2.30}$$

$$K_S = R_F R_\rho (K_T - K^\infty) + K^\infty, \tag{2.31}$$

but as they did not use a turbulence model, they approximated the diffusivity caused by processes not related to double diffusion as $K^\infty = 0.3 \times 10^{-4}\,\mathrm{m}^2\,\mathrm{s}^{-1}$. In this study, the constant K^∞ is replaced with the value calculated from the superposition of internal wave activity, static instability and local shear instability (described above). Zhang et al. [1998] apply double-diffusive mixing only where the magnitude of the vertical temperature gradient $T_Z = \frac{\delta T}{\delta Z}$ is larger than a critical value $T_{Z,C} = 25 \times 10^{-4\circ}\,\mathrm{C}\,\mathrm{m}^{-1}$ to restrict double-diffusive mixing to the thermocline. This restriction is not applied in the present study.

2.8 Acknowledgments

We are grateful to Bablu Sinha for assistance with nutrient transport diagnostics and for operational assistance with OCCAM. We would like to thank two anonymous reviewers for their constructive comments who helped to improve the manuscript. And we would like to thank the German National Academic Foundation for funding parts of this study, and the National Oceanography Centre, Southampton, for hosting MSG and for computer resources. Financial support by the Deutsche Forschungsgemeinschaft through SFB 460 is acknowledged.

Chapter 3

Contribution of oxygen minimum zone waters to the coastal upwelling off Mauritania

This chapter is a reprint of the paper "Contribution of oxygen minimum zone waters to the coastal upwelling off Mauritania" published in Progress in Oceanography. Author's rights without the need to obtain specific permission from Elsevier include the right to include the journal article, in full or in part, in a thesis or dissertation[1]*)*

Citation: Glessmer, M. S., C. Eden, and A. Oschlies (2009), Contribution of oxygen minimum zone waters to the coastal upwelling off Mauritania, Progr. Oceanogr., 83, 143–150, doi:10.1016/j.pocean.2009.07.015.

3.1 Abstract

The coastal upwelling off Mauritania and its connection with the oxygen minimum zone (OMZ) in the tropical Atlantic is investigated in an eddy-resolving general circulation model. Two main supply routes for the upwelling are identified. First a southern eastward pathway crossing 23°W between 3°N and 10°N related to the equatorial zonal current system supplies up to 50 % of the water upwelled in winter, and about 30 % in summer. Second, another eastward pathway crossing 23°W further north between 28°N and 38°N supplies 35 % of the upwelled water in spring compared to 25 % during the rest of the year. Most of the water of the northern pathway is entrained into the mixed layer already before reaching the upwelling

---

[1] http://www.elsevier.com/wps/find/authorsview.authors/copyright as of 12.08.2009

region. Only the southern pathway contributes not recently ventilated waters to the upwelling. The connection with the OMZ is very weak, only about 1 % of the upwelling waters originate here. On the other hand, if water from the OMZ reaches the surface mixed layer within six years, this mostly (71 %) happens in the upwelling region.

3.2 Introduction

A main feature of today's marine oxygen fields is the presence of extended oxygen minimum zones (OMZs) in the eastern tropical oceans. These areas can be of biogeochemical relevance whenever oxygen levels become low enough to allow for anaerobic conversion of fixed nitrogen, a major nutrient essential for biological production, into gaseous nitrogen not accessible to most organisms (Bange et al. [2005]). In consequence, waters emerging from OMZs may exhibit low nitrate-to-phosphate (NO_3^-:PO_4^{3-}) ratios and high concentrations of nitrous oxide (N_2O) as well as of methane (CH_4), gases which have similar relevance for climate change as carbon dioxide (CO_2) (IPCC [2007a]). Large variations in oceanic oxygen concentrations coinciding with changes in the marine nitrogen cycle have been seen in the past (Jones and Jenkins [2001]). Climate models predict an expansion of OMZs as well as an overall decline of the dissolved marine oxygen inventory with global warming (Bopp et al. [2002]; Matear and Hirst [2003]), which was recently supported by observational results (Stramma et al. [2008b]). Additionally to their impact on the nitrogen cycle, low oxygen values provide a hostile environment for many organisms like fish or marine mammals.

Oceanic concentrations of dissolved oxygen depend on both physical and biogeochemical processes. The strength of the oxygen minimum depends on the dynamic balance of the downward flux of organic detritus, its remineralization and the intensity of lateral and vertical mixing and advection, i.e. on the history and residence time of the water mass. In the tropical oceans, OMZs are located in regions with little advective ventilation, often called 'shadow zones' (Luyten et al. [1983]; Sverdrup [1938]; Wyrtki [1962]). These happen to be typically located below highly productive coastal upwelling regions, along the eastern boundaries of the subtropical oceans. Eastern boundary upwelling systems are driven by equatorward coastal winds and the resulting westward, i.e. offshore, Ekman transport. Nutrient-rich waters are upwelled and allow for high productivity when reaching the euphotic zone. High productivity in turn generates enhanced amounts of organic material, part of which sinks downward as detritus and is decomposed by bacteria. In the latter process oxygen is consumed. Together with the slow advective ventilations of the 'shadow zones', this explains why OMZs are typically located underneath regions of high biological productivity associated with eastern boundary upwelling regions.

The proximity of the oxygen minimum zone to coastal upwelling regions makes it possible that upwelling regions are dynamically linked to the oxygen minimum zone (Canfield [2006]). This seems to be supported by measured tracer concentrations: N_2O and CH_4, which are believed to be preferentially formed in the OMZ, show high concentrations along the coastal upwelling regions, and lower concentrations further offshore (Kock et al. [2008a,b]). This suggests the existence of a direct transport from the OMZ to the coastal upwelling.

For an assessment of possible physical-biogeochemical feedbacks in the climate system associated with upwelling regions connecting OMZs and the mixed layer, it is essential to understand what the typical residence time of water in the OMZ is (hence how fast climate induced changes can be processed by the OMZ) and where and on what time scales OMZ water (along with the possibly altered NO_3^-:PO_4^{3-} ratios and the newly formed greenhouse gases like N_2O) reaches the mixed layer and the euphotic zone, and hence starts to interact with the biology and the atmosphere.

In this study we concentrate on the upwelling off Northwest Africa which is the southern part of the Canary Current upwelling system, the least studied and probably the most complex (Tomczak and Godfrey [2003]) of the four major eastern boundary upwelling systems, which are the California, Peru, Benguela and Canary Current upwelling systems. Note that the Arabian Sea features a periodic upwelling system related to the Indian Monsoon. The upwelling off the coasts of Mauritania and Senegal has been studied by e.g. Hughes and Burton [1974]; Jones and Folkard [1970]; Mittelstaedt [1983, 1991] and Wooster et al. [1976], and has recently come into focus again (Elmoussaoui et al. [2005]; Ould-Dedah et al. [1999]; Pastor et al. [2008]) and is investigated in this study by means of a high-resolution numerical model. Although oxygen levels in the OMZ off West Africa are still well above the thresholds for the onset of anaerobic consumption of fixed nitrogen (Paulmier and Ruiz-Pino [2008]), oxygen concentrations have declined during the past decades (Stramma et al. [2008b]) and are expected to expand substantially during this century (Oschlies et al. [2008]).

A good overview of the northwest African upwelling is given in Mittelstaedt [1991]. The upwelling off Mauritania is being described as a wind driven upwelling system restricted to a narrow strip along the coast. It can be separated into two regimes: south of approximately 20°N upwelling is most pronounced during winter and spring, whereas upwelling north of 20°N occurs all year round with a maximum intensity in summer and early fall. The upwelling system is influenced by the Canary Current system offshore, which modulates the water supplied by the tropical circulation. North of the transition between the regimes, a significant amount of the upwelled water is North Atlantic Central Water (NACW), whereas south of the transition an important constituent is the less saline South Atlantic Central Water (SACW). Both pathways into the upwelling supply subsurface waters from layers shallower that 300m.

This paper is organized as follows: In the next Section, the model and methods are presented along with the definition of the respective OMZ and upwelling regions used in the present study as well as a brief evaluation. Pathways into the upwelling are investigated in Section 3.4.1, followed by a discussion on the connection with the OMZ in Section 3.4.2. Section 3.5 summarizes the results.

3.3 Model and methods

3.3.1 Ocean general circulation model

For this study, an isotropic 1/12° version of the FLAME model (based on GFDL MOM-2.1 code (Pacanowski [1995]) is used in a regional North Atlantic setup, reaching from 20°S to 70°N. The model domain is bounded by land in the east and west, northern and southern boundaries are treated following the open boundary formulations by Stevens [1990]. The eastern Mediterranean Sea is represented by a restoring zone. Vertically, the model domain is divided into 45 z-levels, with level thicknesses ranging from 10m in the uppermost 50 m to 250 m for the grid boxes deeper than 2250 m. The maximum depth is 5500 m. Horizontal resolution ranges from ca. 5 km in high latitudes to ca. 9 km in the region of interest. Vertical mixing is parameterized by the turbulent kinetic energy based closure of Gaspar et al. [1990].

After a climatological spinup of 10 years, the model is run for 5 years under monthly climatological forcing. Sensitivity runs with daily forcing have been performed and found to produce similar results in terms of ventilation rates of the

OMZ and of the upwelling region. For a more detailed model description see Eden [2006].

3.3.2 Trajectory calculations

In a trajectory study of the model's circulation field (described in Section 3.4.1 and 3.4.2), the flow field is assumed to consist of particles, in the following called floats, each associated with the same volume of water. The trajectory of a float is calculated from the instantaneous three-dimensional Eulerian velocity field of the model, $\vec{v}$, by numerical integration over the differential equation $\mathrm{d}\vec{x}/\mathrm{dt} = \vec{v}$, with the float position $\vec{x}$ (Döös [1995]). For all calculations, velocities defined on the model grid are linearly interpolated in space and time onto the float position.

Trajectories are calculated both online (i.e. during the model run) and offline (reading in velocity fields from archived model output) as well as forward and (in case of the offline runs) backward in time. Calculating trajectories offline is computationally much cheaper than running the whole model; calculating backward in time presents the opportunity of finding source regions of special water masses. In this paper we concentrate on floats that have been integrated offline using velocity field snapshots taken every 3 days from a climatological run. We have performed up to 30 years of integration, by repeated use of snapshots from a single climatological year. Comparison with climatological online calculations as well as on- and offline calculations using daily forced velocity fields have shown very little difference, justifying our procedure in agreement with previous studies (Böning and Cox [1988]). Additionally, tests with twice or half as many as the 10000 floats used here yielded very similar results.

3.3.3 Tracer release experiments

While the model floats follow the advective velocity field, but do not experience subgrid-scale diffusive mixing, a simulated tracer distribution is determined by both. In a simulated tracer release experiment, an additional passive dye tracer is integrated during the model integration, thereby being advected and diffused following the same numerical algorithms as temperature and salinity. The tracer is passive in the sense that it has no effect on either density or any other model quantity. The passive tracer is initialized with the value 1 in a certain region and with 0 everywhere else. Note that these extreme tracer gradients at the boundaries initially lead to very high mixing, however they are diminished within a few time steps.

In comparison to floats, tracer release experiments have the advantage that they represent exactly the same transport processes that act on all other model tracers. We deduce the time and location where the tracer gets in contact with the atmosphere by assuming that the tracer is destroyed on entering the mixed layer. This is represented in the model by setting the tracer concentration to zero in the uppermost layer of the model at every time step.

3.3.4 Definition of regions

Three regions, 'the upwelling off Mauritania', 'the OMZ' and 'the 23°W-box' are defined for practical purposes in the present study. They are shown in Fig. 3.1, and will be described in the following. Both the definition of the OMZ and the upwelling box include 'dry' land grid points, which are not taken into consideration in the ocean model.

An important choice for our model analysis is the location of the coastal upwelling box called 'the upwelling off Mauritania'. It is well known that the characteristics of the upwelled water masses change sharply at approximately 20-21°N from oxygen-deficient South Atlantic Central Water (SACW) to well ventilated North Atlantic Central Water (NACW) Hughes and Burton [1974]; Jones and Folkard [1970]; Mittelstaedt [1983, 1991]; Ould-Dedah et al. [1999]; Pastor et al. [2008]; Wooster et al. [1976]). North of the 20°N boundary, the upwelling is drawn from NACW carried towards the African coast with the Azores current and further alongshore with the Canary Current (Elmoussaoui et al. [2005]; Mittelstaedt [1991]). We define 'the upwelling off Mauritania' as the box 16-18°W and 12-24°N to include the regions of strongest vertical model velocities in the coastal upwelling and contributions of SACW and NACW at the same time.

In the experiments analyzed below, 10000 floats deployed in this box were released uniformly distributed at 50m depth. This depth was chosen to be below the surface mixed layer at all times but still shallow enough to experience the high velocities of the coastal upwelling. Floats were released on January 15th, April 15th, July 15th and October 15th, in order to represent the annual cycle of the upwelling. Additional sensitivity experiments that released floats every day, every week or every month did not significantly change our results.

The second region discussed is the OMZ located in the shadow zone (Luyten et al. [1983]). Observations indicate that the offshore extent of the OMZ incorporates a rather large area from the northern rim of the equatorial current system at about 10°N to the Cape Verde Frontal Zone at 16°-20°N (Karstensen et al. [2008]; Stramma et al. [2008a]). In a model simulation with embedded biogeochemistry (Eden [2006]), the OMZ is located in a similar area with, however, lower oxygen content compared to the observations (see Fig. 3.1). Note that too low oxygen concentrations in OMZs are a well known feature of biogeochemical models (Meissner et al. [2005]) and might point towards a common model bias, which is however beyond the scope of the present study. Note also that the low oxygen waters within the OMZ are not well separated from the broad coastal upwelling region extending from 10° to 20°-21°N (e.g. Jones and Folkard [1970]; Pastor et al. [2008]), hampering a precise geographical definition of the OMZ in both model and the observations. However, here we have tried to define the location of the OMZ as well as possible and in particular consistent with the model simulation in order to elucidate the ecological significance of the OMZ.

We define the OMZ as a rectangular box at 17-20°W, 12-17°N, 200-300m depth in which 10000 floats were uniformly distributed. This box was chosen on the basis of a model run with embedded biogeochemistry including oxygen (Eden [2006]; Eden and Oschlies [2006]) and it represents the average position of the core of the OMZ in that model. In the case of the forward trajectories started in the OMZ, only one run started on January 15th is discussed here in detail. Apart from a temporal offset, other runs with other release times showed similar results and will therefore not be considered separately.

The third region is 'the 23°W-box'. It consists of the 23°W-section in the west, land in the east and meridional limits at 0°N and 38°N. The section at 23°W was chosen for comparability with measurements from the literature and the northern and southern sections closing the box were chosen north of the northernmost and south of the southernmost backward trajectories of floats released in the upwelling off Mauritania crossing the 23°W section within 30 years.

3.3.5 Comparison with observations

Model results have been compared with observations in previous studies (see above), in particular for the region of interest by Stramma et al. [2005] and Hormann and Brandt [2007]. However, estimates of the coastal upwelling off North-

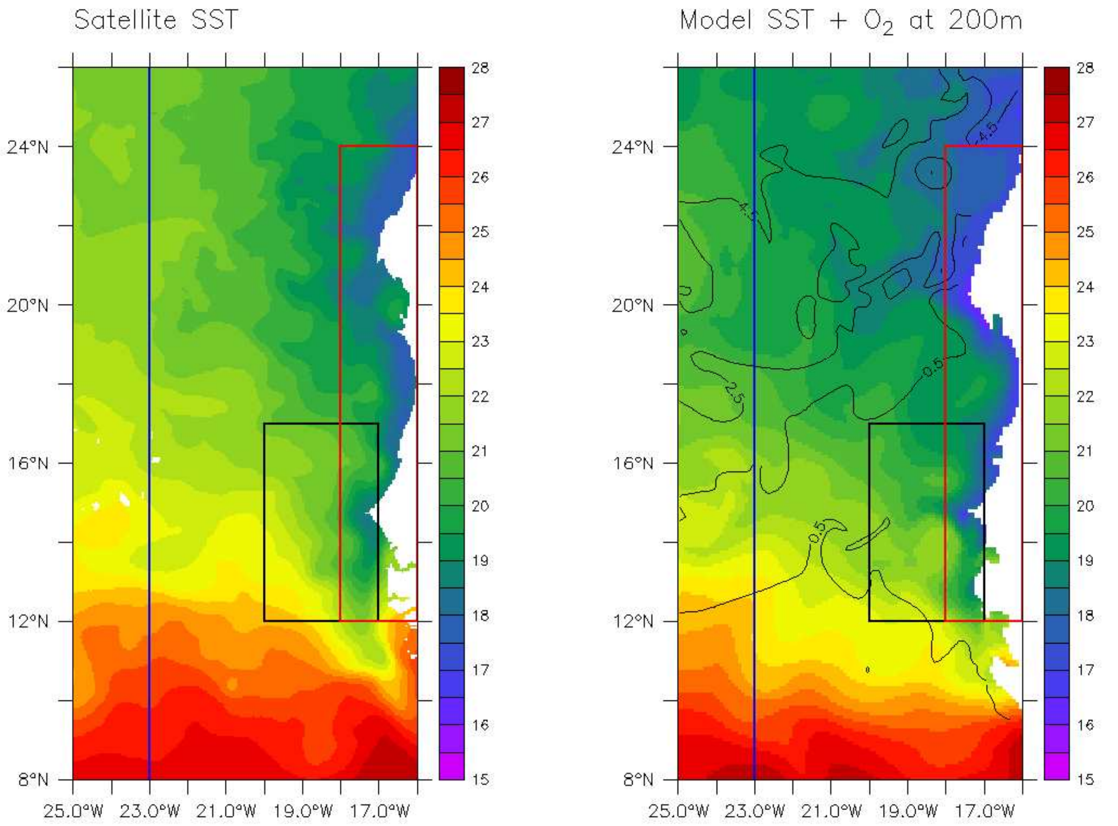

Figure 3.1: Sea Surface Temperature (SST) snapshots derived from satellite data (OSTIA data product, see text for details) for February 10th, 2007 (left panel) and modelled for February, 11th, of a climatological year (right panel). The modelled SST is overlayed with oxygen contours in 200 m depth (in [ml/l], after Eden and Oschlies [2006]). The black box denotes the area between approximately 200 m and 300 m depth in which all wet points are called 'oxygen minimum zone', the wet points inside the red box are called 'the upwelling off Mauritania' and the blue line is the section at 23°W which is part of the '23°W box' bounded at 38°N in the north and 0°N in the south.

west Africa based on hydrographic measurements are sparse and validation of the model in the upwelling region itself can only be done with nonhydrographic measurements.

Fig. 3.1 shows a snapshot of the sea surface temperature (SST) from the model compared with a satellite-based estimate of the Operational Sea Surface Temperature and Sea Ice Analysis (OSTIA) of NCOF1 showing a typical upwelling situation. The modelled SST and the satellite-based SST show good agreement both in the displayed temperature range and in the position of isotherms. Complete agreement of both snapshots can of course not be expected because of differences in mesoscale variability. Shown is February 11th of a climatological model year and a snapshot of the actual SST for February 10th 2007. The good qualitative agreement indicates that upwelling dynamics causing the displayed temperature distributions are well represented in the model.

Overlying the modelled SST field, contours of the dissolved oxygen concentration simulated by the same model at 200m depth are shown (Eden [2006]). The black box denotes the OMZ region between approximately 200 and 300m depth.

3.3.6 Upwelling transport, annual cycle and comparison with Ekman estimates

Upwelling into the region off West Africa is thought to be mainly wind-driven (Mittelstaedt [1983]), and classical linear Ekman theory can be used to compute the upwelling transport from the wind stress curl. However, the actual upwelling transport in the model is calculated using two different approximations. One is to look at the vertical advective transport through the 50m depth horizon in the 'upwelling region'. The other method computes, at each time step and lateral position, the maximum vertical velocity for each water column. These maximum velocities are then averaged in time. Note, that the depth at which the vertical velocity is maximal varies with time but is close to the surface in any case, such that it captures the maximum upwelling. The seasonal variations of both estimates of the modeled upwelling transport agree well with the one predicted from the curl of the wind stress following Ekman theory (Fig. 3.2).

Upwelling transports are largest in late winter and spring and lowest in late summer (Mittelstaedt [1991]). Theoretical upwelling transports are consistently higher than modelled ones, however this agrees with observations (Dever et al. [2006] and references therein) which show that the full transport predicted by Ekman theory only occurs offshore of a certain water depth because of the interaction of the surface and bottom boundary layer, and also depends on the local stratification.

3.4 Results

3.4.1 Pathways into the upwelling

Studying supply routes into the upwelling off Mauritania by the Lagrangian approach described in Section 3.3.2 helps to distinguish source regions and hence

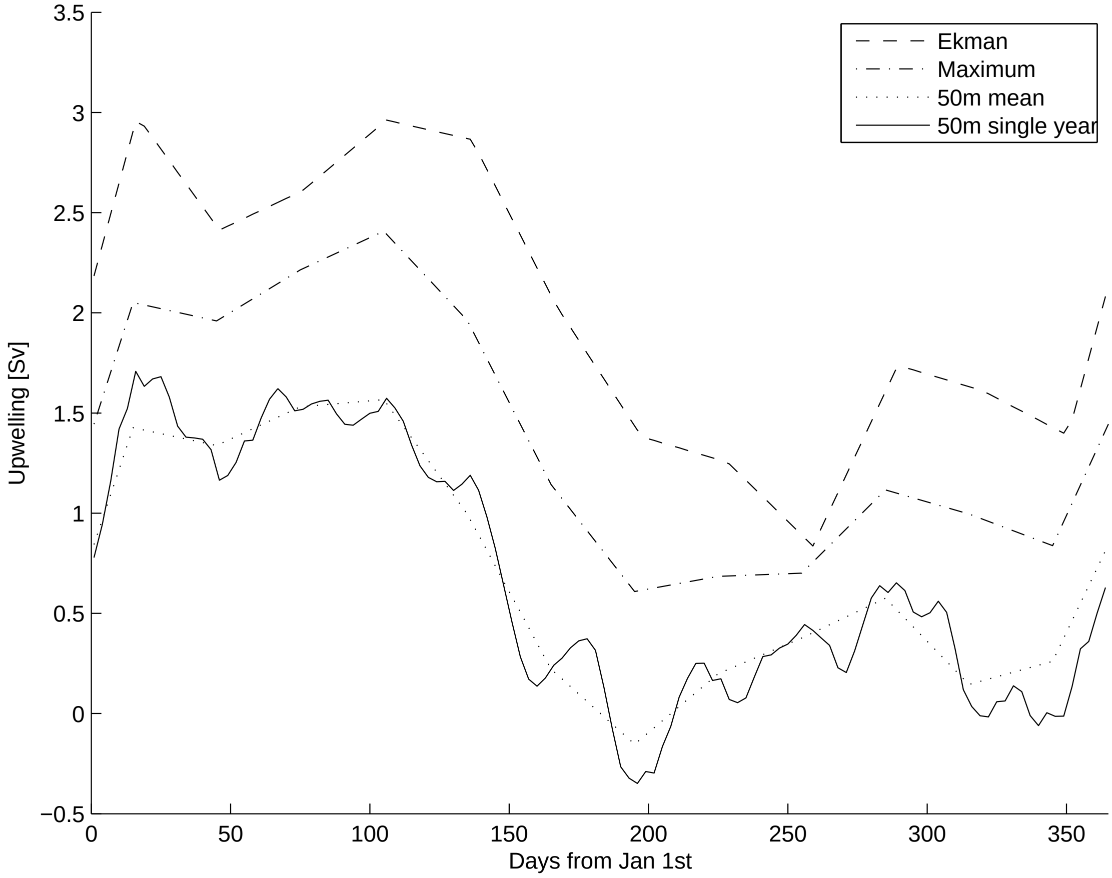

Figure 3.2: Upwelling in [Sv] into 'the upwelling region' off West Africa (16-18°W, 12-24°N). Upwelling calculated after Ekman theory from the wind stress forcing the model (dashed line). Upwelling calculated using the modelled vertical velocity at every gridpoint at the depth of the velocity maximum (dashed-and-dotted line). Upwelling calculated from the modelled vertical velocities through 50 m as monthly average over the model run (dotted line) and, as an example, through 50 m for the model year in which the floats were deployed (solid line).

predict properties like dissolved oxygen concentrations or nutrient concentrations. Floats considered here have been released in the upwelling region between the surface and 50m depth, and are integrated backwards in time. This means that we are looking at those floats that 'end up' in the upwelling (which is where they are started from for the backward-in-time trajectory integration) and 'start' at many different locations in the subtropical gyre and the equatorial current system (which corresponds to their position are at the end of the backward integration).

A northern and a southern boundary, 38°N and 0°N, were chosen to close a box, including all transport through 23°W. The section at 23°W has been occupied by observational campaigns and the simulated transports and water mass characteristics have been shown to be very well represented by the model (Brandt et al. [2008]; Hormann and Brandt [2007]). If integrations were long enough, eventually all floats would arrive from outside the box, but 92 % of the floats, on the annual average (94 % in winter down to 90 % in spring), come from outside the box already within the first five years. Thereof only about 1 % arrives from the south or the north, respectively, without crossing 23°W within the first 5 years. The remaining 8 % have not been outside the box within the first 5 years, 0.7 % of the floats have been inside the box and additionally passed through the OMZ.

In Fig. 3.3, the blue dots indicate the point where a float crossed the section 23°W before reaching the upwelling. Shading shows the annual mean zonal velocity at that section. The upper panels show the number of floats entering the box binned in 1-degree latitudinal bins. The contribution of different pathways to the upwelling changes with season. During autumn and winter, the biggest fraction of floats reaching the upwelling (42 % and 53 %, respectively) originates in the equatorial zonal current system between 3°N and 10°N at 23°W, as compared to 27 % in spring and 33 % in summer. The main eastward currents of the equatorial current system contributing to the upwelling are the North Equatorial Under Current (NEUC, 4°N), the North Equatorial Counter Current (NECC, 6°N), the northern NECC (nNECC, 8°N) and another more northerly current band at 11°N (more details can be found in Stramma et al. (2005)). In spring, the current system between 28°N and 38°N at 23°W supplies 35 % of the floats, compared to 28 % in summer, 22 % in fall and 20 % in winter. These changes correspond to the different upwelling regimes: A summer-intensified upwelling in the Canary Current (Bakun and Nelson [1991]) in the north and a winter-intensified upwelling off the coast of Mauritania and Senegal. Red dots in Fig. 3.3 indicate floats that were always below the mixed layer between the time they crossed 23°W and the moment they reached the upwelling. This criterion was chosen in order to exclude particles whose properties have been modified via contact with the atmosphere or by biological production (mixed layer depth used here as a proxy for the depth of the euphotic zone). For these floats, the picture remains essentially the same with regard to the southern bit of the transport. The contribution of the zonal current system between 0°N and 10°N at 23°W slightly declines by 0 to 3 %. However, the northern pathway between 28°N and 38°N at 23°W declines to values of only 1 % in winter, 4 % in spring and

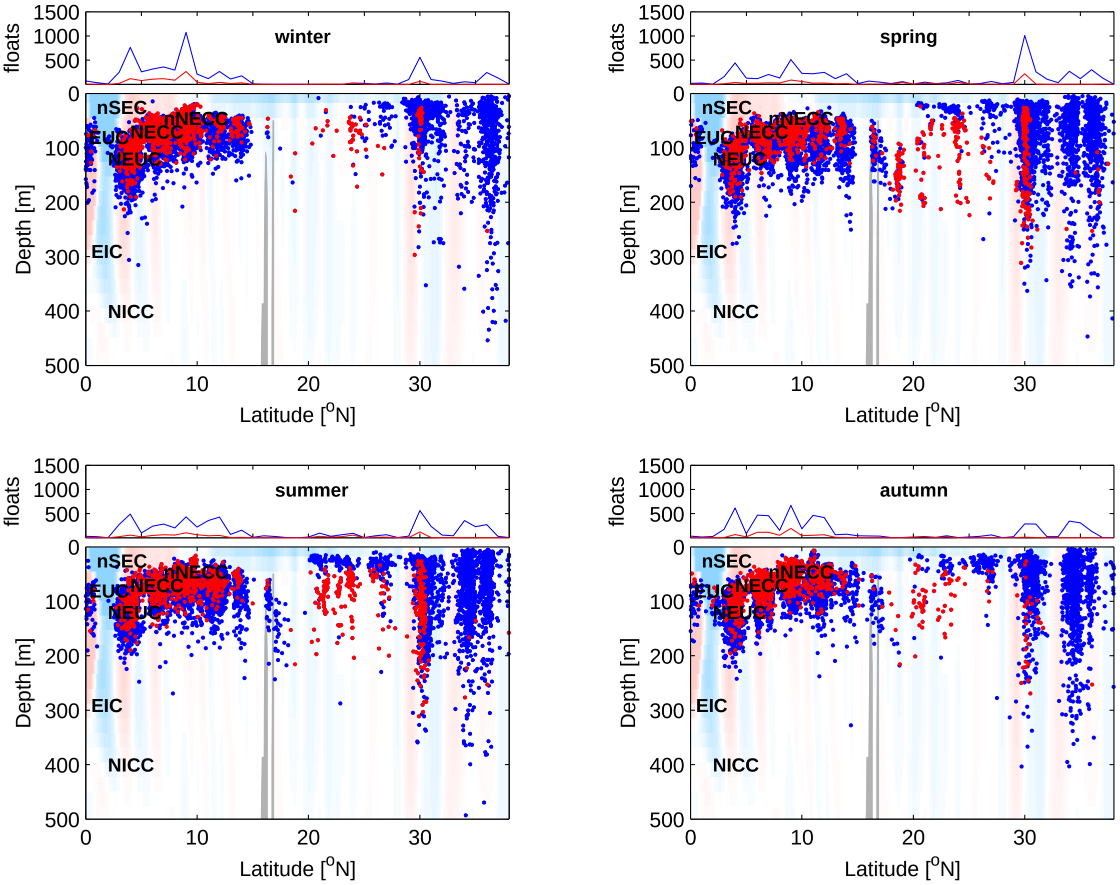

Figure 3.3: Origin of water upwelling in the region 16-18°W, 12-24°N shown in Fig. 3.1 for all seasons. Shown is the point where floats cross the section at 23°W for all floats (blue dots) and floats who have been underneath the mixed layer at all times between crossing the section and reaching the upwelling (red dots). Shading indicates simulated annual mean zonal velocities at 23°W (red: eastward, blue: westward). Currents are named following Stramma et al. [2005]: Equatorial UnderCurrent (EUC), Equatorial Intermediate Current (EIC), northern South Equatorial Current (nSEC), North Equatorial UnderCurrent (NEUC), North Equatorial CounterCurrent (NECC) and northern NECC (nNECC). Grey shading indicates topography.

summer and 2 % in autumn. Here most floats are in the surface mixed layer at least once before reaching the upwelling.

3.4.2 Oxygen minimum zone

In this Section, we concentrate on the connection between the OMZ and the upwelling region. Within the first 5 years after being released in the oxygen minimum zone, only 5 % of the floats reach the upper 50m of the ocean. Of these 5 %, 74 %-84 % surface in the upwelling region off Mauritania. Upwelling of oxygen minimum floats occurs mainly in spring coinciding with strongest upwelling, independent of the time of their release in the OMZ. Approximately 6 years after release, floats start to upwell predominantly outside of the upwelling box. Accordingly, they are no longer influenced by the strong seasonal cycle of the coastal upwelling, and instead display a more uniform distribution of surfacing times during the annual cycle. Within 30 years, 32 % of the floats have been shallower than 50m at least once, thereof 11 % in the upwelling region.

Looking at trajectories of particles being released in the oxygen minimum zone shows that the average mean flow is small compared to the random eddy flow, i.e. no advective pathways - and especially none connecting the oxygen minimum zone and the upwelling - are prominently visible. Note also that the lateral spreading is predominantly caused by realistic mesoscale variability, i.e. isopycnal mixing in our eddy-resolving model. The vertical spreading is governed by different dynamics, i.e. small-scale turbulent vertical (diapycnal) mixing not felt by the floats.

The transport error that arises from the neglect of diapycnal mixing in the float trajectory calculation can be estimated with a 'tracer release experiment'. The tracer is released in the same box representing the OMZ that has been used for the release of the floats in this Section. Fig. 3.4 compares when and where the floats and the tracer that were released in the OMZ simultaneously reach the mixed layer. In case of the tracer, we show the accumulated concentration of tracer that has been destroyed in the uppermost model layer over the first 6 years after release in the OMZ. The amount of tracer destroyed is then gridded on a 1°×1° grid and normalized to yield a global integral of one. For the floats we counted each event on a 1×1° grid where a float first entered the mixed layer during the first 6 years after being released in the OMZ. Whether a float is in- or outside the mixed layer is determined by comparing the density at the floats' current position with the density at the sea surface directly above the float. The total flux of floats into the mixed layer has then been normalized to yield a global integral of one. When looking at the regions defined before, floats and tracer behave very similarly except that about 2 times more tracer than floats has upwelled in all regions. After 6 years, 14 % of the tracer has entered the mixed layer compared to 7 % of floats which have been in the mixed layer at least once during these 6 years. Of the total upwelled amount, 75 % of tracer and 67 % of floats have upwelled in the upwelling box, and 85 % of tracer

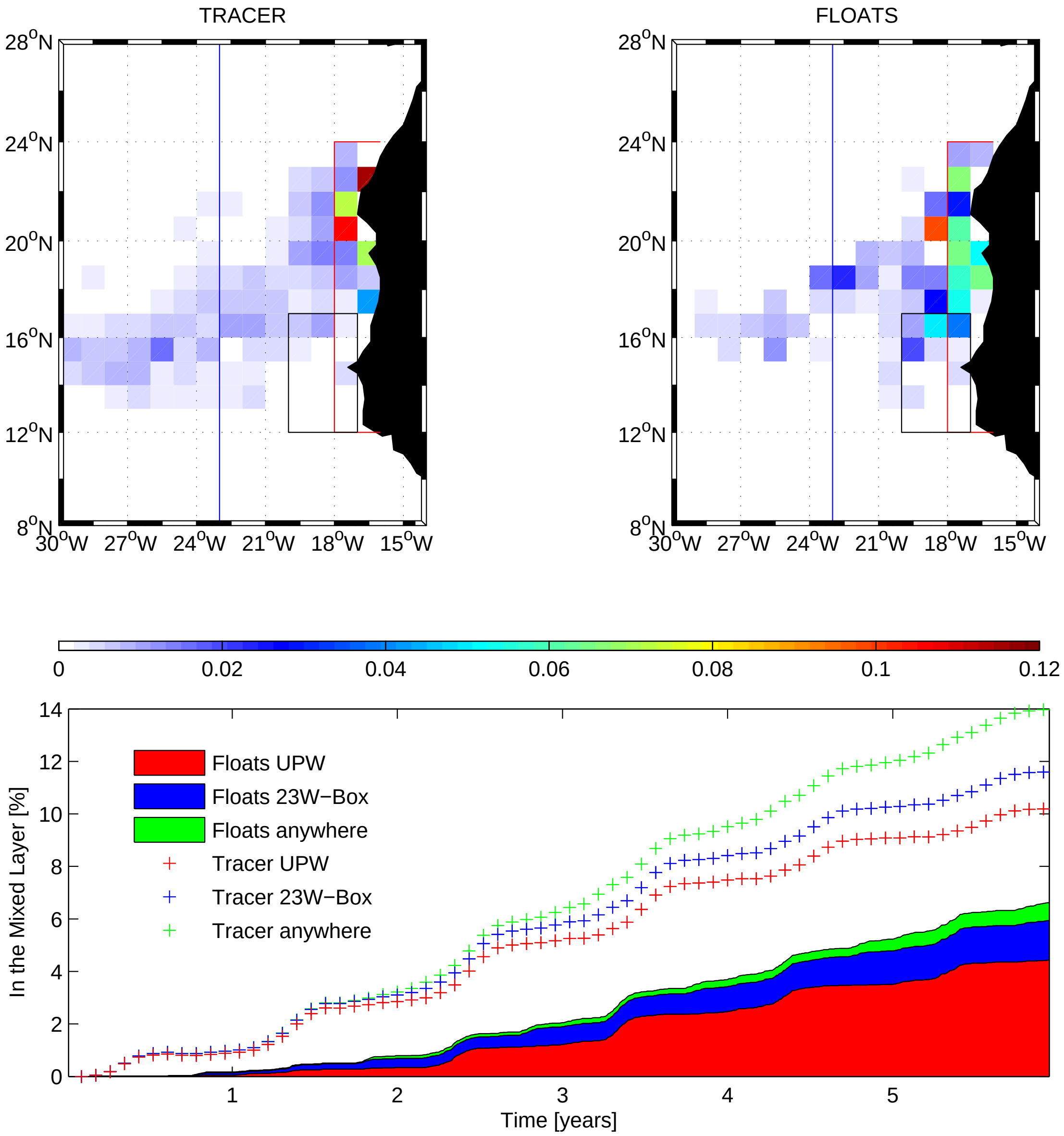

Figure 3.4: Upper left panel: Amount of tracer reaching the mixed layer within six years after its release in the OMZ, upper right panel: amount of floats reaching the mixed layer within three years after their release in the OMZ. For reasons of comparability, floats and tracer are gridded on a 1°×1° grid and their concentrations are normalized. Lower panel: Number of floats being released in the oxygen minimum zone and reaching the mixed layer within the upwelling (lowest wedge) within the 23°W-Box (middle) and anywhere else (upper) as a function of time. Green crosses show the amount of tracer that reaches the mixed layer. All graphs in [%]. The boxes indicated in the upper panels indicate those used for the wedges in the lower panel (Upwelling in red, 23°W-Box in blue).

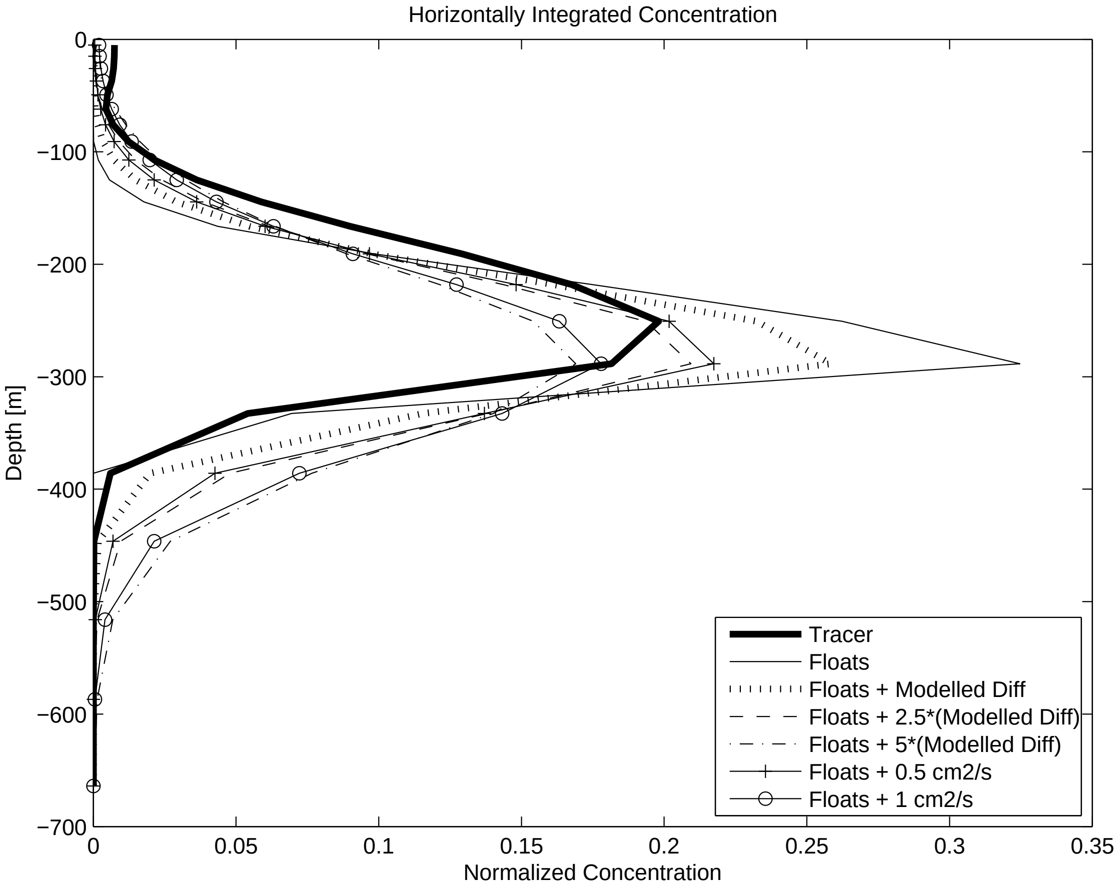

Figure 3.5: Estimates of the diffusion that the horizontally averaged float distribution would need in order to reproduce the horizontally averaged tracer distribution after a one-year run. Shown are the horizontally averaged profiles of tracer (thick solid line), floats (thin solid line), floats + modelled diffusion (dotted line), floats + 2.5*modelled diffusion (dashed line), floats + 5*modelled diffusion (dashed and dotted line), floats + 0.5 cm^2s^{-1} (solid line with crosses) and floats + 1 cm^2s^{-1} (solid line with circles).

and 89 % of floats have upwelled in the 23°W box. So even though twice as much tracer has upwelled, the regional distribution is very similar for upwelled tracer and floats. The difference in magnitude can be related to sub-grid scale vertical mixing felt only by the tracer but not by the floats.

A rough estimate of the effective diffusivity felt by the tracer can be obtained using a simple one-dimensional (1D) model of vertical diffusion without advection. Used as initial conditions are horizontally averaged modelled float concentration profiles are taken from the end of the first year of the three dimensional (3D) float simulation. This profile of float concentrations that is the result of one year of 3D advective float transport is then diffused vertically for one year by applying different diffusivities in the 1D model. Thus, advective and vertical diffusive transports are computed sequentially for one year each. Results of the one-year 3D float advection plus one-year 1D float diffusion simulations are then compared to the laterally averaged evolution of the one-year 3D dye-tracer simulation, which accounts for advective and diffusive transports simultaneously. Using constant diffusivities we find that the maximum tracer and float concentrations agree best when vertical diffusivities of about (0.5-1)*10^{-4}m^{2}s^{-1} are imposed on the initial float profile (see Fig. 3.5). When using the explicit diffusivity profile used in the model simulation rather than constant additional diffusivities, 2.5 times the values of the explicit diffusivites used in the model simulation are needed in order to reproduce the concentration at the tracer maximum in the simple 1D model. This corresponds to 0.6*10^{-4}m^{2}s^{-1} at the depth of the tracer maximum and indicates that implicit numerical diffusion in this region is of the same order of magnitude as the explicitly applied diffusion in this region of our model.

3.5 Conclusions

Two main supply routes of waters upwelling off Mauritania are identified in the model, agreeing well with observations by, for example, Mittelstaedt [1991]. First the southern pathway crossing the 23°W section between 3°N and 10°N and originating in the equatorial zonal current system, namely the NEUC, the nNECC and a more northerly band of the equatorial zonal current system, supplies up to 50 % of the water upwelled in winter, and about 30 % in summer. Second, the northern pathway crossing 23°W between 28°N and 38°N supplies 35 % of the upwelled water in spring compared to 25 % during the rest of the year. If only water is considered that stays below the mixed layer between crossing 23°W and reaching the upwelling, the northern pathway is almost non-existent. Therefore the main factor influencing biogeochemical properties in the upwelling region is the southern pathway and not the OMZ: The connection of the upwelling with the OMZ is very weak, only about 1 % of the upwelling waters originate in the OMZ. On the other hand, water leaving the OMZ tends to reach the mixed layer mostly in the coastal upwelling rather than further offshore on annual to decadal time scales.

According to our model, about 10 % of the tracer labeling the OMZ waters reach the surface mixed layer on a time scale of 6 years. If our findings for the tropical

Atlantic also apply to other upwelling regions situated above OMZs, this would suggest that the direct link between denitrification and nitrogen fixation postulated e.g. by Deutsch et al. [2007] is weaker than assumed. However, the observed increase of N_2O and CH_4 concentrations towards the Mauritanian upwelling regions (Kock et al. [2008a,b]) cannot simply be explained by a direct advective route between the OMZ and the upwelling. Instead, the link between OMZ and upwelling is largely mediated by diapycnal mixing processes that, in our model, are sub-grid scale. The strength of diapycnal mixing in the area is not well known and needs to be better constrained in order to obtain robust estimates of the leakage of OMZ waters into the upwelling off Mauritania.

3.6 Acknowledgments

We are grateful to Julia Getzlaff for providing the 1-D diffusion model. We would like to thank two anonymous reviewers for their constructive comments that helped to improve the manuscript. Funding of MSG through the BMBF Sopran project as well as the DFG-funded SFB 754 is acknowledged.

Chapter 4

The connection of the oxygen minimum zones with the surface ocean - a comparison between the Atlantic and the Pacific Ocean in models of different resolutions

4.1 Abstract

The Atlantic and Pacific oceanic oxygen minimum zones (OMZs) are located in the poorly ventilated shadow zone regions of their respective ocean basins. Close to eastern boundary and equatorial upwelling regions, nutrient rich water is brought up into the surface mixed layer. Thereby high biological productivity is sustained as well as eventually export of organic matter, whose remineralization at depth consumes oxygen. Time scales for feedback processes, e.g. between changes in nitrate-to-phosphate ratios in the OMZs and the surface mixed layer ecosystem, have to be longer than time scales of physical transport processes which bring water from OMZs up to the surface. Water from the Pacific OMZs reaches the surface mixed layer much faster than water from the OMZs in the Atlantic Ocean. These differences are investigated in a range of general ocean circulation models varying horizontal resolutions from high resolution FLAME (1/12°), eddy-permitting ORCA025 (1/4°) to the typical resolution of coupled climate models ORCA2 (2°), using float and tracer release experiments. Counter-intuitively, the interannual vari-

ability of the amount of tracer released in the Atlantic and Pacific OMZs reaching the mixed layer within 20 years is found to be quite large. Not only in the eddy-permitting ORCA025 model runs, but also in the coarse resolution ORCA2. This suggests that the system is much less simple than is commonly thought. Although the upwelling behavior of OMZ waters can partly be related to ENSO dynamics or the larger scale density field, most of the variability could not be easily related to indices of larger scale patterns. Under a CO_2 doubling scenario, the interannual variability is found to increase, while the strength of the connection between the OMZs and the upper ocean decreases.

4.2 Motivation

Oceanic oxygen minimum zones (OMZs) play an important role in the climate system, as under low oxygen conditions chemical and biological processes are fundamentally different from the rest of the oxygenated ocean. Under "normal" oxygen conditions, nutrient trapping in upwelling regions sustains high productivity. If oxygen levels fall below certain thresholds, rather than dead material being remineralized at depth, denitrification starts and molecular nitrogen and the greenhouse gas nitrous oxide are formed. Molecular nitrogen and nitrous oxide are inaccessible to most organisms, and are eventually lost to the atmosphere (Codispoti and Richards [1976]). This leads to low nitrate-to-phosphate ratios in the regions where water from the OMZs reaches the surface ocean, potentially influencing ecosystem composition. Molecular nitrogen can be made biologically available again by nitrogen fixers like cyanobacteria (Codispoti and Christensen [1985]). Externally driven changes in the oceanic nitrogen budget can be counteracted by a opposing changes in the rate of nitrogen fixation.

It has not yet been understood completely to what extent the position, size, and oxygen values of OMZs are determined by physical or biological processes. Oxygen concentrations are basically set to their highest value through exchange with the atmosphere when a water mass is being formed in the mixed layer. Afterwards, when the water mass is subducted and advected through the ocean interior, oxygen concentrations can change through mixing with water masses of different oxygen concentrations, or decline when oxygen is consumed by biological or chemical processes. Depending on the strength of the respiration, generally, oxygen concentration of a water mass decreases with time away from the atmosphere.

Atlantic and Pacific OMZs are located in so-called “shadow zones” (Luyten et al. [1983]; Sverdrup [1938]; Wyrtki [1962]) where advective ventilation is weak and hence waters can reside for a long time with little or no new oxygen being supplied. In addition, OMZs are also in close vicinity to the highly productive eastern boundary and equatorial upwelling areas, where degradation of sinking dead organic material uses up oxygen. However, rather than being located directly underneath the equatorial upwelling, OMZs are found to the north and south of it while directly at the equator a more oxygenated band exists.

In the Pacific OMZ, denitrification is taking place under current climatic conditions already (Deutsch et al. [2001]). In the Atlantic OMZ, oxygen concentrations are still well above critical thresholds, but oxygen concentrations in the world oceans are expected to decrease with global warming (Bopp et al. [2002]; Matear and Hirst [2003]), which was recently supported by observational results (Stramma et al. [2008b, 2009]). Predictions of how upwelling systems will react on global warming depend on the relative magnitude of two opposing effects: the thermal effect could strengthen the density stratification enough to decrease upwelling (DiLorenzo et al. [2005]) or the intensification of the thermal lows on the continents could lead to winds that are strong enough to enhance upwelling (Bakun [1990]). Therefore, understanding what determines the minimum oxygen concentrations in OMZs and why they are so different for the two ocean basins might enable us to forcast how mechanisms might change under global warming, and what consequences that might have on the ecosystem.

In a recent study, Deutsch et al. [2007] estimated that regions of nitrogen fixation are closely connected to zones of low oxygen and active denitrification in the water column, using a coarse resolution model (4° horizontal resolution). From that they inferred a feedback between externally driven changes in the oceanic nitrogen budget and the rate of nitrogen fixation acting on timescales of years to decades. Climate models investigating the role of the ocean in modulating climate change as well as feedbacks between ocean, atmosphere and biogeochemistry typically use a horizontal resolution of 2° longitude and latitude or even coarser. However, results of models are not independent of model resolution, as lower resolution means that more processes are too small or too fast to be explicitly resolved.

In case of OMZs, potentially important “unresolved processes” are not only eddies or surface waves, but also the equatorial current system, where narrow, alternating zonal thermocline and sub-thermocline current bands feed the equatorial

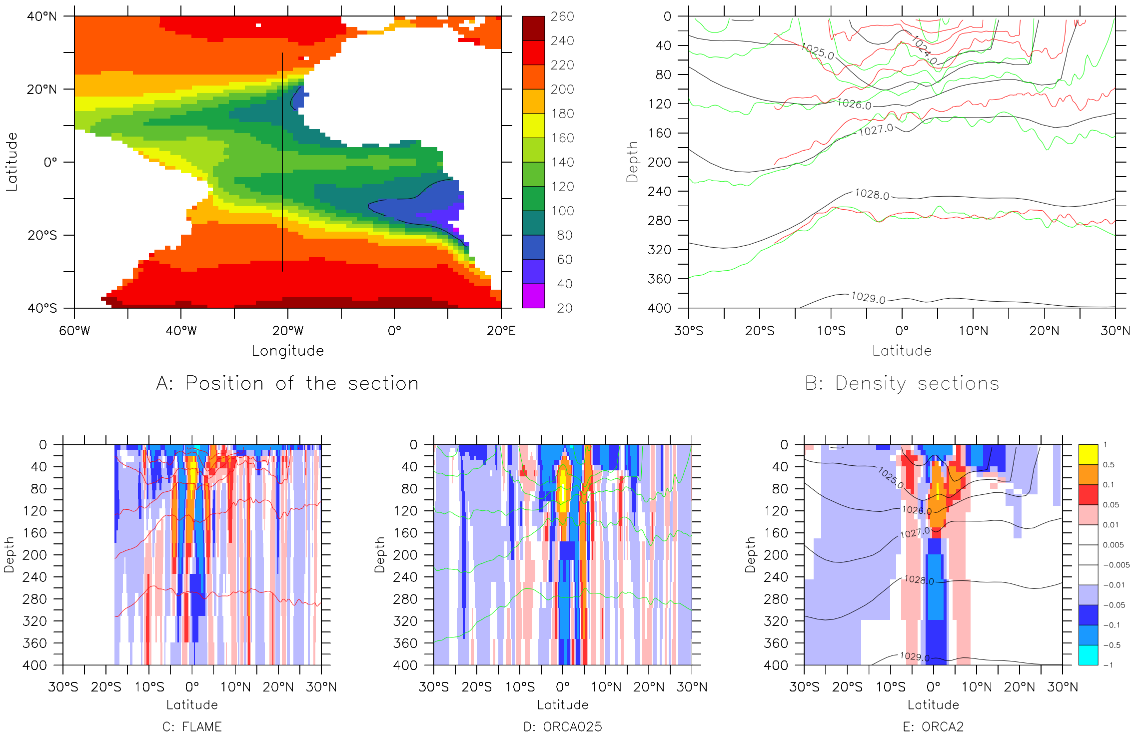

A: Position of the section

B: Density sections

C: FLAME

D: ORCA025

E: ORCA2

Figure 4.1: Panel A: WOA05 oxygen concentration in 200 m depth [μmol/l] with black contours at 80 μmol/l. Panel B: densities from the three different models (for details please refer to text) on the 23°W section shown in Panel A. Panel C-E: Zonal velocities (color, m/s) and density contours at 23°W for FLAME (Panel C), ORCA025 (Panel D) and ORCA2 (Panel E).

and eastern boundary upwelling systems and that supply oxygen along the equator. These current bands are less well represented the coarser the model resolution becomes (See Figure 4.1). Also inside the OMZ regions themselves model fields differ (See Figure 4.2 and Figure 4.3. Note: in FLAME the southern boundary of the model domain is at 20°S, and viscosity is greatly enhanced in a sponge layer close to the boundary. Hence in that latitudinal range FLAME data has to be handled cautiously). While density structures are represented relatively well, the velocity fields are very different. Seeing those differences, the question arises to what extent the horizontal model resolution influences the representation of OMZs and their connections with the upper ocean, and if climate models are capable of modeling the OMZs at all.

However, horizontal model resolution does not only affect the supply pathways into OMZs but also the upwelling systems in which OMZ waters reach the mixed layer again. In Glessmer et al. [2009] (Chapter 3, in the following called GEO09) the

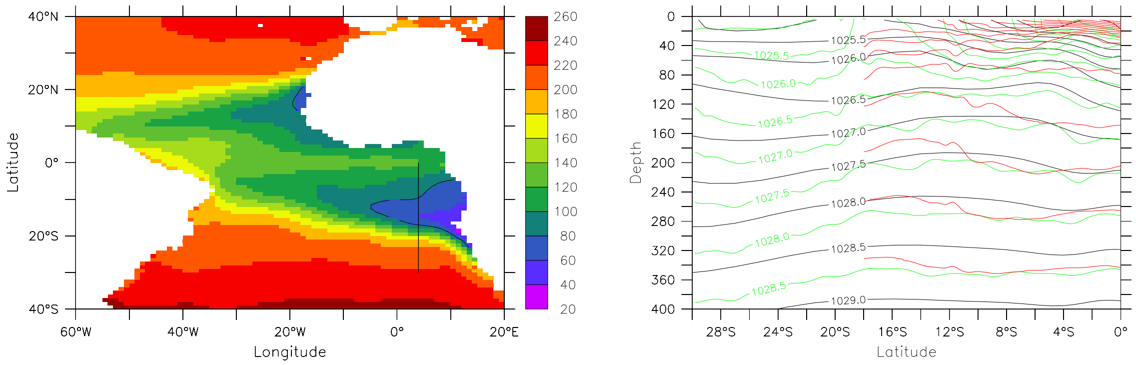

A: Position of the section

B: Density sections

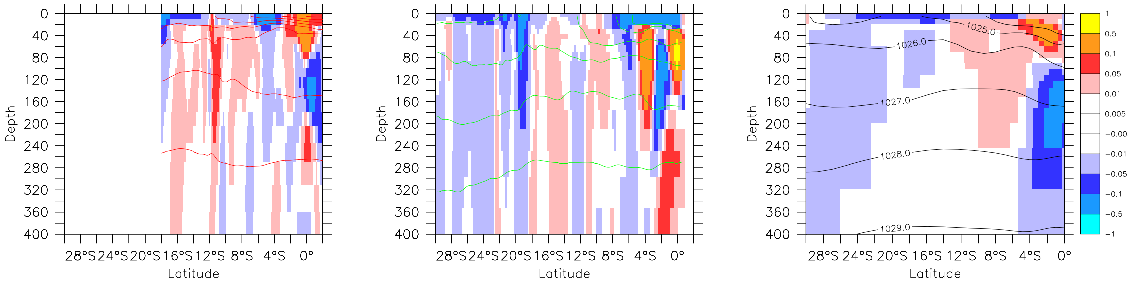

C: FLAME

D: ORCA025

E: ORCA2

Figure 4.2: Panel A: WOA05 oxygen concentration in 200 m depth [μmol/l] with black contours at 80 μmol/l. Panel B: densities from the three different models (for details please refer to text) on the 4°E section shown in Panel A. Panel C-E: Zonal velocities (color, m/s) and density contours at 4°E for FLAME (Panel C), ORCA025 (Panel D) and ORCA2 (Panel E).

connection between the OMZ off Mauritania in the eastern tropical North Atlantic and the upper ocean is investigated through float and tracer release experiments in a state-of-the-art high resolution model (1/12° horizontal resolution). Within 6 years only 7 % of the floats released in a box (described by geographical coordinates: 12°N-17°N, 17°W-20°W, 178.5 m-310.6 m (k=13:16)) and located in the OMZ, defined by oxygen fields simulated with that model, reach the mixed layer. However, floats are only advected and hence do not represent diffusive transports. In regions with little advective ventilation, diffusive transports are of bigger relative importance. In a tracer release experiment, GEO09 find that within 6 years 14 % of the tracer released in the same box as the floats reaches the mixed layer. This connection of the OMZ with the mixed layer is much weaker than suggested by for example Deutsch et al. [2007] in their model with 4° horizontal resolution. This suggests that horizontal model resolution influences the connection.

It is widely accepted (see for example Fung et al. [2000]) that coarse resolution

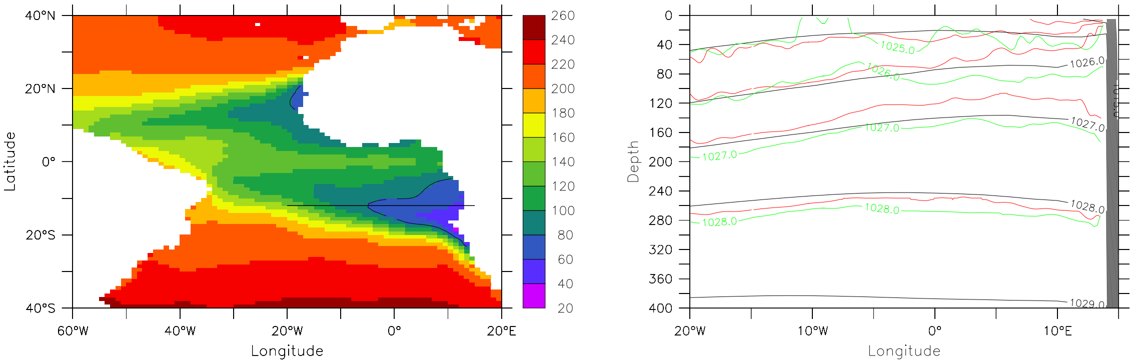

A: Position of the section

B: Density sections

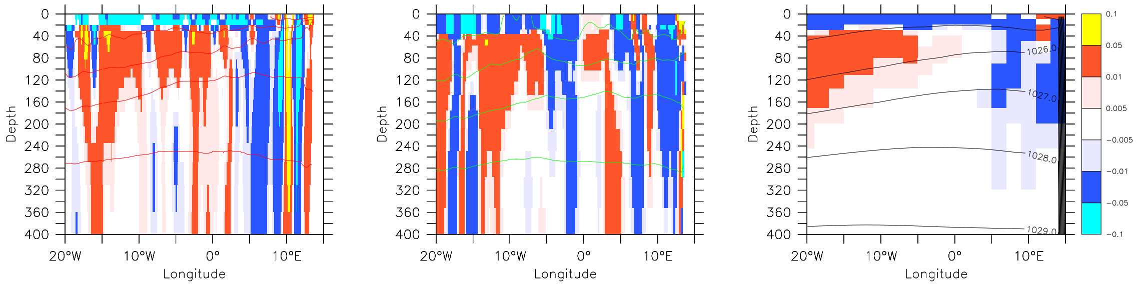

C: FLAME

D: ORCA025

E: ORCA2

Figure 4.3: Panel A: WOA05 oxygen concentration in 200 m depth [μmol/l] with black contours at 80 μmol/l. Panel B: densities from the three different models (for details please refer to text) on the 12°S section shown in Panel A. Panel C-E: Zonal velocities (color, m/s) and density contours at 12°S for FLAME (Panel C), ORCA025 (Panel D) and ORCA2 (Panel E).

models do not represent coastal upwelling systems as good as high resolution models do. If upwelling in the region between the western coast of Africa and 10° west of the coast between 6°N and 30°N (northern box) as well as the whole width of the Atlantic Ocean from 6°S to 6°N (equatorial box, boxes shown in Figure 4.16) are investigated, this problem does not seem to exist. Averaged over the width of several grid boxes the more sluggish upwelling in the coarse resolution model equals the narrow upwelling of the higher resolution models. Annual cycles of upwelling rates for the northern coastal boundary upwelling and the equatorial upwelling are shown in Figure 4.5. Coastal upwelling calculated using Ekman theory is very similar between the models, both in their annual cycle and regarding annual means (4.3 Sv for FLAME, 4.2 Sv for ORCA025, and 4.2 Sv for ORCA2). As both ORCA models use identical wind forcing fields, differences between the Ekman estimates of the different models are due to different model grids, which cause different coast lines and different interpolations of the forcing wind field. FLAME uses a different forcing which leads to substantially different upwelling estimates. Upwelling rates calculated for the northern box from the vertical model velocities display a more distinct seasonal cycle for ORCA025 and ORCA2 than for FLAME, although annual mean values are not that different between the models (1.6 Sv for FLAME, 1.4 Sv for ORCA025 and 1.0 Sv for ORCA2). As all these estimates agree well, the advective part of the northern coastal upwelling (although it is the region where almost all of the floats deployed in the GEO09 OMZ reach the mixed layer) cannot explain why the amount of floats that reach the mixed layer within 20 years is substantially different between FLAME, ORCA025 and ORCA2. As already mentioned in GEO09, the upwelling calculated from the curl of the windstress is approximately twice as high as the upwelling calculated from modelled vertical velocities. Although this discrepancy is found in observational data, too, no conclusive explanation has been found yet. But since the discrepancy also exists for the equatorial upwelling it cannot be caused by bottom friction as previously suggested.

For the equatorial box, the amplitude of the annual cycle is again smaller for FLAME than for ORCA025 and ORCA2. Average upwelling transport is 6.3 Sv for FLAME, but more than twice that value for ORCA025 and ORCA2 (14.0 Sv and 13.1 Sv, respectively). This shows that at least on the larger scale horizontal model resolution does not have a dramatic effect on upwelling transports. And since transports are similar this suggests that large scale velocity fields are similar, too. However, upwelling rates alone do not determine the strength of the connection between OMZs and the mixed layer: Mixing modifies fluxes and can - by changing the density structure - also change the flow field.

In Figure 4.4, solid lines display the time it takes for floats released in a box (17°W-20°W, 12°N-17°N) in the tropical North Atlantic to reach the surface mixed layer which is defined by a density criterion. For Figure 4.4 only floats released at the 200 m z-level are taken into consideration. 20 years after their release in the OMZ-box described above, 52 % of the FLAME floats (run FLAME-AF0ZBRF, for details see Section 4.6.1) reach the mixed layer, 78 % of the ORCA025 floats (ORCA025-AFSZBCF) and 28 % of the ORCA2 floats (ORCA2-AFSZBCF). This clearly demonstrates the importance of analyzing how models of different horizontal resolution represent the pathway from the OMZ to the mixed layer and leads to the hypothesis that while ORCA2 shows a weaker connection between the OMZ and the mixed layer than FLAME, the eddy-permitting ORCA025 model displays too

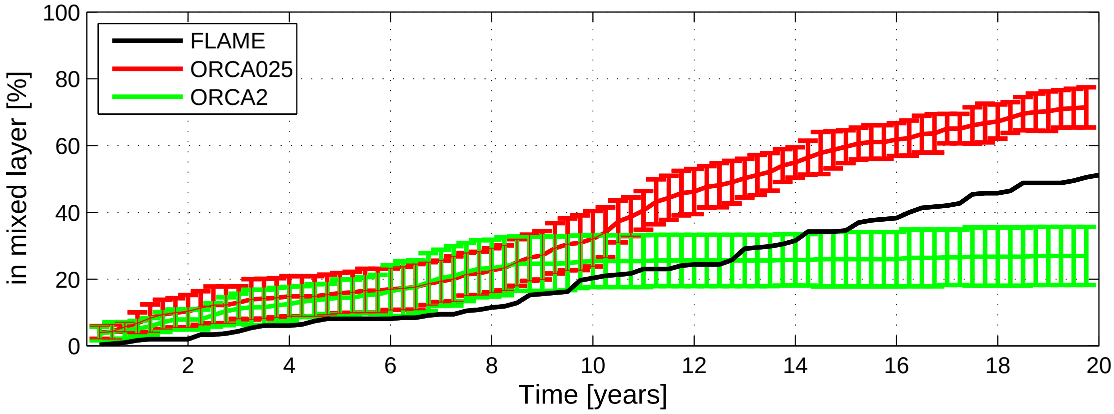

Figure 4.4: Mean percentage (± standard deviation over several runs started between 1978 and 1985) of floats reaching the surface mixed layer for models of different horizontal grid resolutions: 1/12°FLAME (black line, FLAME-AF0ZBRF), 1/4° ORCA025 (red lines, ORCA025-AFSZBCF) and 2° ORCA2 (green lines, ORCA2-AFSZBCF). Floats are started in the box 17°W-20°W, 12°N-17°N in 200 m depth.

high numerically induced mixing. Being aware of the potential influence of model resolution on the results is of particular relevance when utilizing coarse resolution models to forcast climate. However, several issues related to the curves shown in Figure 4.4 need to be addressed.

Firstly, the region where floats were deployed was chosen for reasons that were meaningful in the GEO09 study, but which are not here. A map of transit-time-to-mixed-layer of floats deployed at 200 m depth throughout the tropical Atlantic shows that although the region used in GEO09 did well represent - and was located in the middle of - the shadow zone in that model, the dynamical regions are slightly shifted in both ORCA runs, so that the deployment area sits well on the edge of the shadow zones (see Figure 4.10) and hence in ORCA the results become very sensitive to the exact deployment position. In order to obtain more objective results, in this study floats are deployed in the way described and discussed in Section 4.3.4.

Secondly, while in GEO09 it was shown that in that case individual trajectory runs were very similar independent of the time of deployment of floats and different forcing strategies, this is not the case in ORCA025 and ORCA2. Different forcing strategies are discussed in Section 4.4.1.

Thirdly, results for ORCA2 and ORCA025 are shown with errorbars, which indicates that in contrast to the results of GEO09 the connection between the OMZ and the mixed layer exhibits interannual variability. That interannual variability

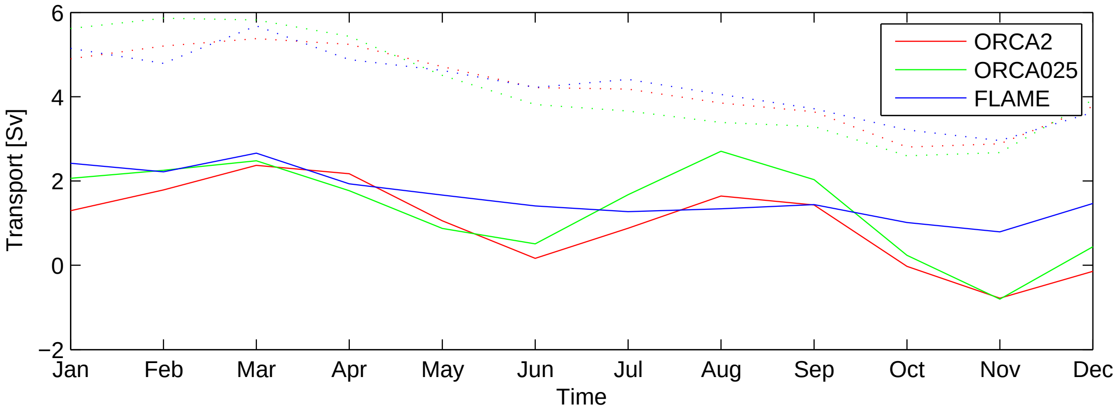

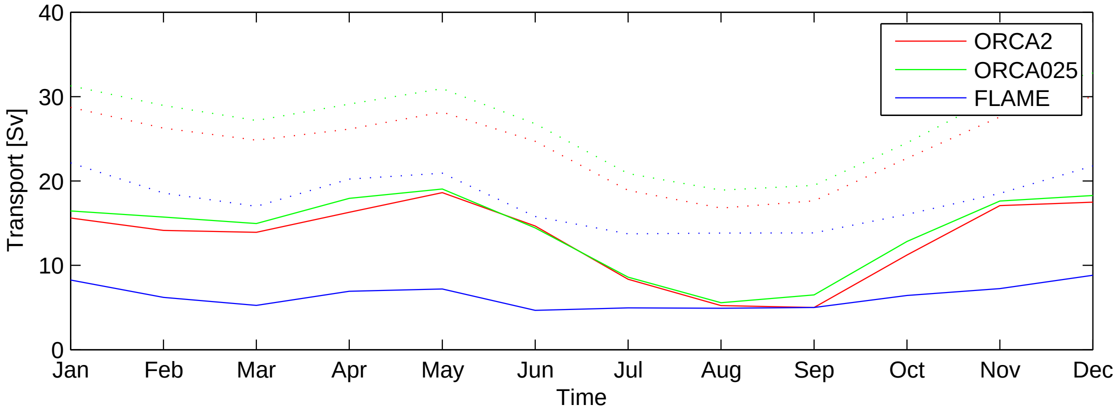

Figure 4.5: Mean upwelling transport in the northern (upper plot) and equatorial (lower plot) box for FLAME (blue), ORCA025 (green) and ORCA2 (red). Solid lines for transport calculated from the vertical model velocities, dotted lines for Ekman transport calculated from the curl of the wind stress (northern box) and from the divergence of the horizontal Ekman transport (equatorial box).

is investigated for the Atlantic in Section 4.4.2 and for the Pacific in Section 4.4.3. Those analyses are expanded to include global warming simulations in Section 4.4.4. The findings are summarized in Section 4.5.

4.3 Models and Methods

In this study, three different ocean models are used as basis for a number of numerical float and tracer release experiments. In the following, the models and methods are introduced. A tabular overview over all float and tracer experiments is given in Section 4.6.1.

4.3.1 Models

The model primarily used in this study is based on the NEMO ocean modeling framework and uses the ocean component OPA in ORCA configuration. ORCA is widely used in several different resolutions and on numerous different topics throughout the European research landscape. It is a z-coordinate OGCM that includes the most recent developments in ocean modeling, such as partial bottom cells and a free surface formulation. Different horizontal resolutions are used in this study:

ORCA025

ORCA025 with a horizontal resolution of 0.25°. This is the run KAB001 by Arne Biastoch[1]. The configuration is based on the Grenoble run G70 Molines et al. [2006], but based on the Drakkar Config Manager V1.12. A weak damping (300 days for 10 m depth) is applied, and full 3D-restoring is performed for both T and S in polar regions with a timescale of 181 days. The horizontal grid was defined as a generic "ORCA" type mesh with 3 poles, using a t-point pivot for the north fold condition. The horizontal grid resolution is 0.25° at the equator, leading to horizontal dimensions of 1442 x 1021 grid points. There are 46 levels on the vertical, with grid spacing ranging from 6 m near the surface to 250 m at 5750 m. The maximum depth allowed in the model is 6000 m. That depth is reached with partial cells, the deepest being 500 m thick in the deep basins. Vertical mixing is parameterized using the TKE scheme. The run is forced with the CORE forcing (Large and Yeager [2004]) and run from 1958 to 2004 and started in 1958 from scratch.

ORCA2

ORCA2 with a horizontal resolution of 2° (run by Olaf Duteil) with 182 x 149 grid points on an ORCA mesh as described above. Forcing is similar to ORCA025. ORCA2 has 31 z-levels with level thicknesses ranging from 10 m in the upper ocean to 500 m at depth.

KCM2

KCM2 (run by Wonsun Park, described in Park et al. [2009]) consists of the ECHAM5 atmospheric general circulation model (Roeckner and Coauthors [2003])

---

[1] http://wiki.ifm-geomar.de/wikiocdoc/index.php/Configuration/ORCA025/Config

coupled to the NEMO ocean model described above for ORCA2 in version OPA9 (Madec [2008]). Eight experiments are started from initial conditions chosen semi-regularly with 30-year or 40-year intervals from a 20th century run. In those eight experiments, carbon dioxide concentration is increased by 1 % per year until doubling is reached after almost 70 years, and stabilized thereafter for another 30 years. Out of those eight experiments, only the first one is analyzed.

FLAME

spFLAME, an isotropic 1/12° model (based on GFDL MOM-2.1 code (Pacanowski [1995]) is used in a regional North Atlantic setup, reaching from 20°S to 70°N. The model domain is bounded by land in the east and west, northern and southern boundaries are treated following the open boundary formulations by Stevens [1990]. The eastern Mediterranean Sea is represented by a restoring zone. Vertically, the model domain is divided into 45 z-levels, with level thicknesses ranging from 10 m in the uppermost 50 m to 250 m for the grid boxes deeper than 2250 m. The maximum depth is 5500 m. Horizontal resolution ranges from ca. 5 km in high latitudes to ca. 9 km in the region of interest. Vertical mixing is parameterized by the turbulent kinetic energy based closure of Gaspar et al. [1990]. After a climatological spinup of 10 years, the model is run for 5 years under ECMWF-Dynamo monthly climatological forcing. The run discussed here is the same as in Glessmer et al. [2009].

4.3.2 Trajectory calculations

In trajectory calculations, numerical "floats" are advected by the simulated velocity field. This method is very helpful to determine transit times of water masses. However, floats only feel the modelled velocity field and neglect diffusion. Using a simple scaling analysis, the time scale t on which diffusive processes are starting to dominate a system can be calculated as $t = \frac{L^2}{K}$ with L being the typical length scale of the system and K being the average diffusivity in the area. Here, the time scale on which mixing starts to dominate the transport of tracers from the OMZ to the mixed layer is deduced. A typical length scale of this process is 100 m from the upper boundary of the OMZ to the surface mixed layer, and vertical diffusivities are typically in the range of $0.1 * 10^{-4} \mathrm{m}^2\mathrm{s}^{-1}$. This leads to a time scale of 32 years. Time scales longer than that have to be investigated by other methods which do not neglect diffusion, like for example tracer release experiments.

In a trajectory study of the model's circulation field, the flow field is assumed to consist of floats, each associated with the same volume of water. The trajectory of a float is calculated from the instantaneous three-dimensional Eulerian velocity field of the model, $\vec{v}$, by numerical integration over the differential equation $\frac{d\vec{x}}{dt} = \vec{v}$, with the float position $\vec{x}$ (Döös [1995]). For all calculations, velocities defined on the model grid are linearly interpolated in space and time onto the float position.

For calculating those trajectories from the ORCA-based runs, a modified version of the packet ARIANE[2] (Blanke and Raynaud [1997]) was used. ARIANE is a FORTRAN code which computes 3D streamlines in a given velocity field, i.e. the output of an Ocean General Circulation Model (OGCM). ARIANE provides two different options for trajectory calculations, qualitative and quantitative. In this study, the qualitative option is used (For reason refer to Section 4.6.2). ARIANE is an offline diagnostic tool. In this study, 5-daily averages of the model velocity as well as temperature and salinity fields are read in. The version used here is based on the ARIANE 2.1.8_17 version, but new routines are included: Firstly, seeding of particles following new strategies is enabled. Secondly, an additional output of densities at z=0 at the position of each float at each timestep is added, allowing to determine via a density criterion whether or not a float is in the surface mixed layer at any given time. In the case of ORCA025, only sub-regions are read in which makes runs much quicker and computationally cheaper. ARIANE has been modified such that the loss of floats through the boundaries does not lead to the abortion of the whole program but only stops the calculation of that particular particle.

Floats are not deployed continuously and in a transport-weighted way, but at discrete points in time. Tests show that interannual variability is larger than seasonal variability. Hence, concentrating on interannual variability, a single run per year is used, started at January 15th each year. However, as shown in Figure 4.12 this potentially introduces aliasing of the seasonal signal.

Calculation of trajectories in the FLAME runs was done with the FLAME routines described in Glessmer et al. [2009]. Floats are advected with daily mean velocity fields, but it was shown there that in that case results do not significantly depend on the forcing frequency.

---

[2] http://stockage.univ-brest.fr/~grima/Ariane/

4.3.3 Tracer release experiments

While the model floats follow the advective velocity field but do not experience subgrid-scale diffusive mixing, a simulated tracer distribution is determined by both. In a simulated tracer release experiment, an additional passive dye tracer is integrated during the model integration, thereby being advected and diffused following the same numerical algorithms as temperature and salinity. The tracer is passive in the sense that it has no effect on either density or any other model quantity.

NEMO V3.1 provides an offline tracer model which reads in velocity fields from earlier runs (in this case ORCA2 as described in 4.3.1) and uses them to advect the tracer fields. Diffusion and all other processes (depending on the tracer e.g. sources and sinks, air-sea-fluxes etc) are done by the same routines as in the online case, and results for online and offline runs are very similar.

In areas that satisfy the OMZ criterion (defined and discussed in Section 4.3.4), the passive tracer is initialized with the value 1 in 196.7 m to 240 m depth (grid level k=17), and with the value 0 elsewhere.

Diffusion of tracer depends on the tracer gradient. Introducing an artificial tracer with sharp gradients leads initially, while the gradients are still high, to unrealistically high mixing. Those initial gradients are diminished within a few time steps, however gradients of the tracer are still different from oxygen gradients in the ocean, leading to different diffusive fluxes.

In comparison to floats, tracer release experiments have the advantage that they represent exactly the same transport processes that act on all other model tracers. The drawback with calculating tracer on the other hand is that only instantaneous concentrations of the tracer are known and trajectories cannot be inferred. To be able to separate the different sources after longer runs, the OMZs in the different ocean basins are calculated in individual fields. Time and location the tracer gets in contact with the atmosphere is deduced by "destroying" the tracer on entering the mixed layer. This is represented by setting the tracer concentration to zero in the uppermost layer of the model at every time step, assuming that mixing within the mixed layer is fast so that errors introduced by only destroying the tracer in the first level and not throughout the whole depth of the mixed layer are very small compared to the time scales of all other relevant processes. Destroying the tracer in the uppermost model layer artificially increases the gradient between the first and the second model layer and hence leads to a higher flux from the second into the first layer.

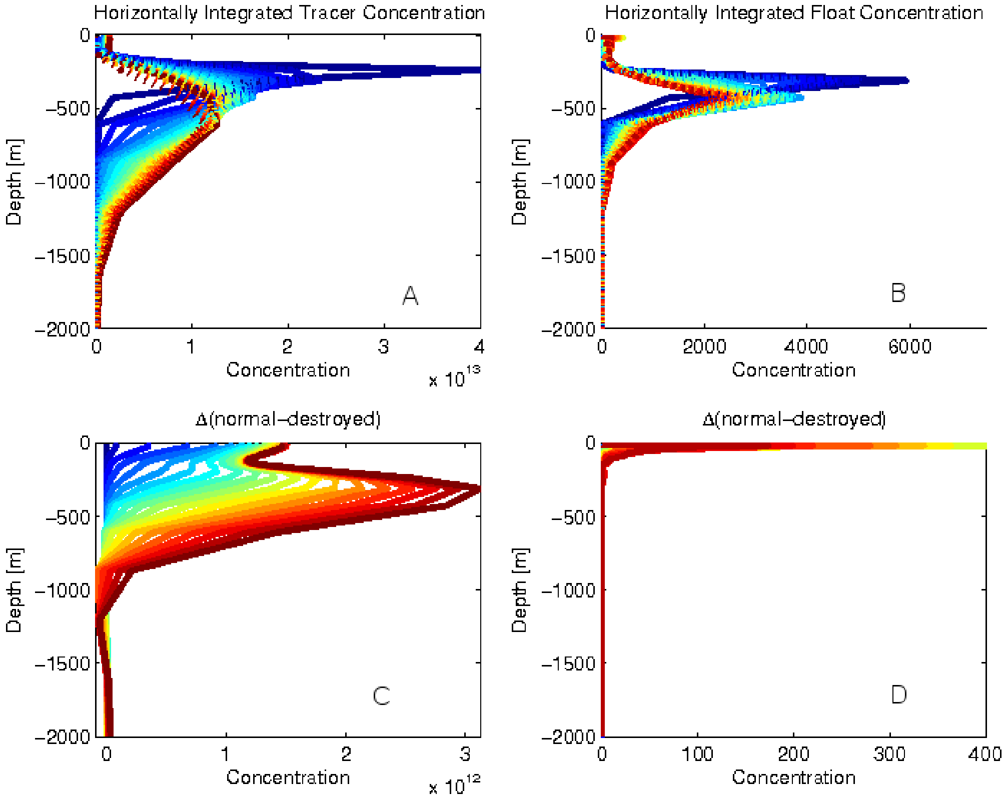

Figure 4.6: Comparison of conservative tracer/floats and a tracer/floats that are destroyed at the surface. All were released in 196.7 to 240 m depth in the Atlantic Ocean region with WOA05 oxygen concentration below 80 μmol/l. Panel A: Horizontally integrated tracer concentration (solid lines: conservative, dotted lines: destroyed at the surface). Colors reaching from dark blue (1st year) to dark red (20th year). Panel B: Horizontally integrated float concentration. Colors and lines as in A. Panel C: Difference between the profiles shown in A. Panel D: Difference between the profiles shown in B.

Destroying the tracer at the surface and keeping track of the distribution of the destroyed tracer provides a way to diagnose where and how much tracer reaches the surface as a function of time. However, it also changes the tracer gradient between the upper most grid boxes and the ones below at each timestep. This gradient influences the diffusion of tracer not only between the surface boxes and the ones below, but progressively over the entire water body. A comparison between the 1978 tracer run in which tracer is destroyed at the surface, and the one with a conservative tracer is shown (Figure 4.6 for the Atlantic, Figure 4.7 for the Pacific). Initially, the biggest difference is at the surface, but after 7 years, a second maximum is starting to form at mid-depth. This maximum is slowly sinking downward, and from 11 years onward is stronger than the maximum at the surface. The minimum in between is at a depth range where upwelling takes place, so in contrast to the surface or the OMZ, tracer does not accumulate here, and hence absolute differences between the runs must be small.

Intuitively, this behavior of tracer runs in which tracer is destroyed at the surface seems not to be desirable. However, one has to keep in mind that the tracer in this case represents a marker for the OMZs. This could for example be an oxygen deficiency or a nitrate-to-phosphate anomaly. Both are destroyed at the surface, too, either through gas exchange or through biological processes. Hence interpretation of the tracer is similar to that of those anomalies.

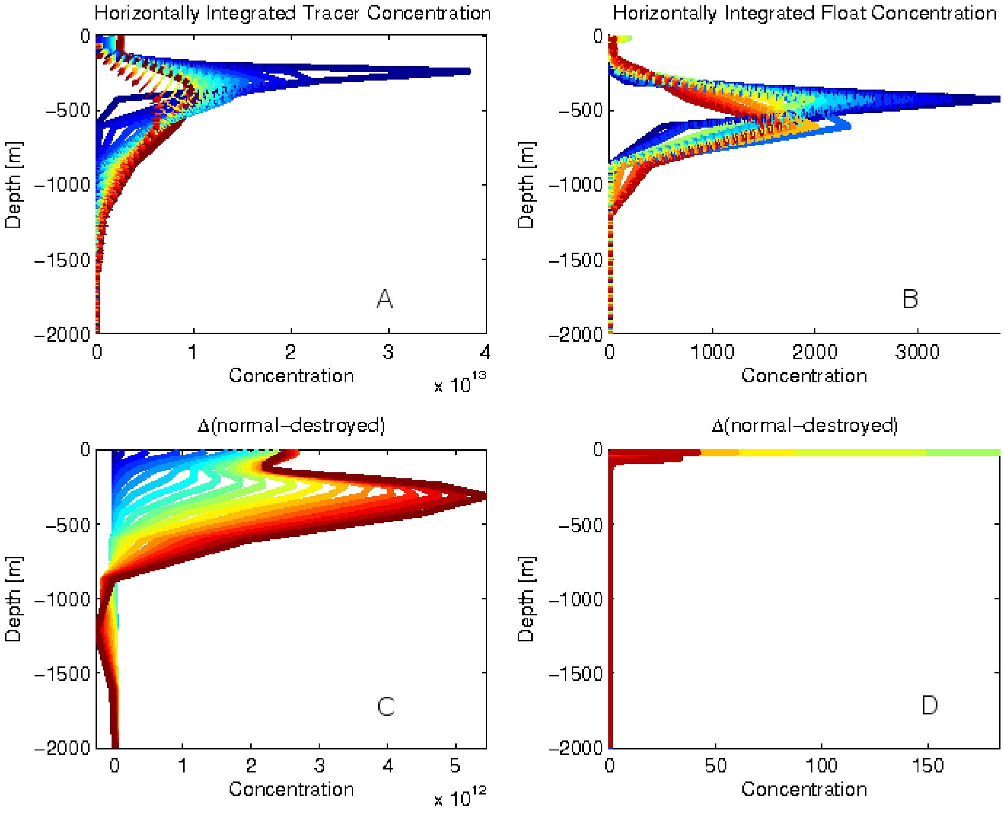

Figure 4.7: Comparison of conservative tracer/floats and a tracer/floats that are destroyed at the surface. All were released in 196.7 to 240 m depth in the Pacific region with WOA05 oxygen concentration below 10 μmol/l. Panel A: Horizontally integrated tracer concentration (solid lines: conservative, dotted lines: destroyed at the surface). Colors reaching from dark blue (1st year) to dark red (20th year). Panel B: Horizontally integrated float concentration. Colors and lines as in A. Panel C: Difference between the profiles shown in A. Panel D: Difference between the profiles shown in B.

Comparing the Atlantic and the Pacific, destroying tracer at the surface introduces bigger differences between runs that destroy tracer and conservative runs in the Pacific than in the Atlantic. This is because in the Pacific case, much more tracer reaches the uppermost boxes, hence much more tracer is destroyed. Therefore the downward traveling signal has to be bigger in this case.

When considering float analyses, a similar phenomenon does not exist: "destruction" of individual floats does not affect the behavior of the other floats. However, the horizontally integrated concentration of floats differs over a wider depth range than only the uppermost boxes because some of the floats that reached the mixed layer have been subducted again and hence are missing deeper down in the profile of the "destructive" run. Hence, tracer runs in which tracer is destroyed at the surface rather than float calculations appear to be the relevant property for the analyses conducted in this study.

4.3.4 How to define "the OMZ"

When talking about comparing OMZs between different models or at different times, it sounds like it should be easy to define what "the OMZ" is. But even in the real ocean, regions with different oxygen concentrations and different biogeochemical environments are not unambiguously defined (Canfield and Thamdrup [2009]). Even if they were, translating an oceanic definition onto a model is not trivial. Not all our model runs included biogeochemical models with oxygen, so choosing the OMZs in the model by just specifying oxygen concentrations was not possible. Modelled oxygen fields strongly depend on the details of the biochemical models used (Meissner et al. [2005]), and the location of the shadow zones in the model. Hence, OMZs in models are not necessarily located in the exact respective area of the real ocean, and additionally often have too low oxygen concentrations. This makes the choice of regions according to an oxygen concentration criterion more questionable, as using this criterion would imply comparing different OMZ volumes in different models. Age and transit-time-to-mixed-layer-distributions suggest that modelled low ventilation regions, although generally in agreement with WOA05 low oxygen zones, are not completely identical, making the use of water-age-criteria also sub-optimal for the definition of the OMZs.

Translating "the OMZ" into the model

In this study, OMZs are defined using the annual mean oxygen fields of the WOA05, interpolated onto the model grids. There are several issues with this criterion: Firstly, oxygen concentrations and hence the position and size of the OMZ vary substantially on interannual timescales which is completely ignored when looking at mean fields. Oxygen concentrations are potentially overestimated in regions with very low oxygen concentrations (which are the regions that this paper takes special interested in), as all surrounding waters and the atmosphere have higher oxygen concentrations which makes sampling without contaminating with higher oxygen values difficult. Additionally, oxygen concentrations in the Pacific OMZ are close to the detection limit of the in-situ-methods. So, even for a definition of OMZs in the real ocean, the WOA05 mean field is potentially not the best choice.

In case of the Pacific OMZ, oxygen concentrations below $10\,\mu$mol/l WOA05 regridded on the model grids are used as criterion for "the OMZ". $10\,\mu$mol/l was chosen as a compromise between two conflicting demands. On the one hand, the main interest of this study in the fate of waters with oxygen concentrations below $5\,\mu$mol/l, where denitrification occurs. In order to ensure that the whole volume of that water is included at all times, a higher oxygen concentration than $5\,\mu$mol/l is chosen as a bound for the OMZ. On the other hand, to prevent getting too close to the edge of both the real and the modelled OMZ where ventilation is a lot higher, so $10\,\mu$mol/l is still sufficiently low to be inside the OMZ at all times. In case of the Atlantic OMZ, due to the much higher oxygen concentrations $80\,\mu$mol/l is chosen as a bound for the OMZ which leads to similar OMZ areas at 200 m depth in the Pacific and the Atlantic Ocean ($1.9\times10^6\,\mathrm{km}^2$).

The 200 m depth was chosen as the average upper edge of the tropical North Atlantic OMZ. In the Pacific Ocean, the OMZ clearly reaches much closer to the surface. However, runs with floats deployed at 60 m depth showed that at that depth all waters reach the mixed layer within the first year after being deployed. Hence 200 m for both the Atlantic and Pacific is chosen for consistency, and compared to other definitions.

4.4 Results and discussion

4.4.1 On different forcing strategies

When trajectory studies are conducted, especially when different time slices are to be investigated and compared to each other, trajectory calculations are often forced with short (usually 1 year) periods of model velocity fields that are repeated as often as necessary in order to obtain the desired length of trajectory runs. This type of run will in the following be called “recycled” run. While this procedure is computationally cheaper because less velocity fields have to be read in, and cheaper in terms of storage, because shorter periods of high-frequency velocity fields have to be stored, it might not lead to the same results as if longer, continuous forcing periods had been used (as in “continuous” runs like the ones that have been investigated in this study up to now).

In case of the transit times from the Atlantic OMZs to the mixed layer, the different forcing strategies lead to different results (Figure 4.8): The mean values for ORCA025 increase by 3 % when comparing continuous to recycled runs (73.1 % for ORCA025-AFSZOCF to 76.2 % for ORCA025-AFSZORF) and by 12 % for ORCA2 (43.5 % for ORCA2-AFSZOCF to 55.1 % for ORCA2-AFSZORF). The standard deviation of the percentage of floats started from the OMZs having reached the mixed layer within 20 years is much larger in ORCA2 (22.1 % for the recycled runs as compared to 3 % for the continuous), and still substantially larger (9.1 % for the recycled and 2.3 % for the continuous runs) in ORCA025. This behavior can be explained by the existence of eddies in ORCA025, which dampen out the signal of different surface forcings. In contrast, in ORCA2 different years are in different states of the circulation, which either allow for a fast connection between the OMZ and the mixed layer, or not. If a specific year is repeated over and over again, its specific characteristics lead to either a lot of floats reaching the mixed layer or only very few, while in continuous runs chances are that during each 20 year run enough different circulation states happen to allow for similar amounts of floats reaching the mixed layer in subsequent runs.

Using continuous forcing which allows for the association of individual runs to specific periods in real time provides also the opportunity to investigate not only a steady state (which is what most trajectory studies up to now have been doing, though this mostly is an implicit assumption rather than being explicitly stated) but also the temporal evolution and changes of the system.

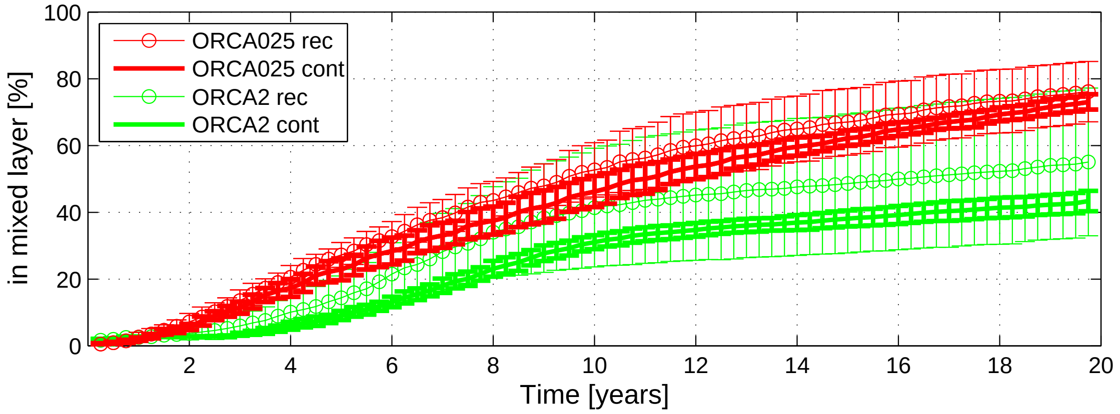

Figure 4.8: Percentage of floats reaching the surface mixed layer for models of different horizontal grid resolutions and forcing strategies: 1/4° ORCA025 (red lines) and 2° ORCA2 (green lines). Bold lines and errorbars represent the mean ± standard deviation for runs that were forced with 20 subsequent years (ORCA025-AFSZOCF and ORCA2-AFSZOCF), thin lines with open circles and errorbars are mean ± standard deviation for runs that were forced with the same year repeated 20 times (ORCA025-AFSZORF and ORCA2-AFSZORF).

Another effect is even more prominent when monthly mean oceanic velocity forcing fields are used. The variability between runs using different years to force the floats increases because large mean flows exist for individual years which cannot be compensated when repeatedly using a single year of forcing. Producing climatological velocity fields by averaging over several years would lead to an even bigger loss of variability and hence mixing that would otherwise be introduced by eddies. While this might not be a problem in ORCA025 it certainly is for ORCA2.

Another issue to consider when interpreting Figure 4.4 is the frequency with which forcing fields change. In GEO09, daily snapshots from velocity fields from a single year could be used over and over again without a significant effect on the results because subsequent snapshots were sufficiently different to well represent the small scale variability. This is no longer possible for ORCA025 and especially ORCA2, when only 5-daily-mean output fields are available and not single day means. This - additionally to being much more large scale than FLAME - leads to loss of variability, which can only at least partly be compensated if subsequent years are different.

Using a single year of velocity forcing repeatedly has its issues. For one, at each backward “jump” in the forcing to the first time step to start the next cycle,

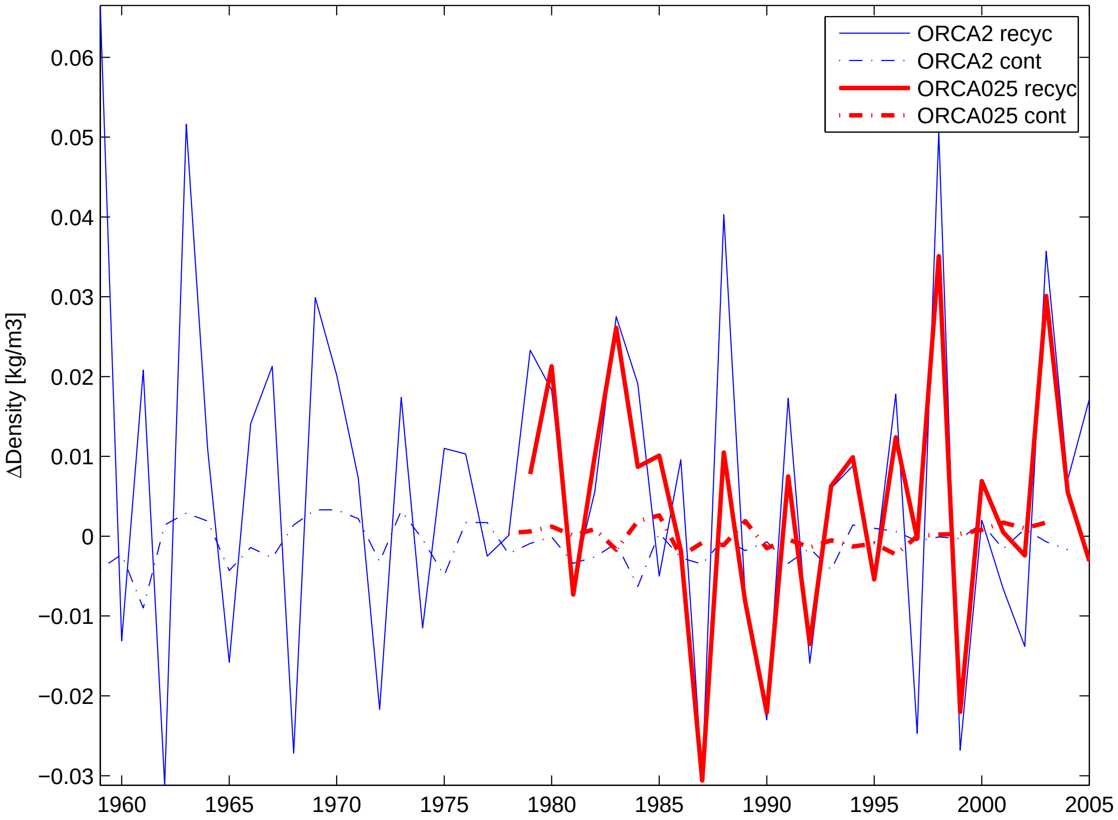

Figure 4.9: Density jump between 29.12. (last timestep each year) and 3.1. (first timestep each year) of each year (solid lines) and between subsequent years (dashed lines), averaged over the region with WOA05 oxygen concentrations below 80 μmol/l in the Atlantic at 200 m depth for ORCA2 (blue) and ORCA025 (red).

floats may end up on different isopycnals and hence in different dynamical regimes than they were at the time step before. This discontinuity in the conditions can lead to diffusive behavior of the floats, as can, for the same reason, low frequency forcing. The standard deviation of OMZ-mean-density jumps between 29.12. and 3.1. of each individual year is an order of magnitude larger than the standard deviation between the density of 29.12. and 3.1. of the subsequent year (Figure 4.9), explaining why in Figure 4.8 the standard deviation is substantially smaller for continuous runs than for recycled runs. As a consequence, the following sections use what could be determined as the best forcing strategy: continuous runs with 5-daily mean forcing fields.

4.4.2 Comparison of ORCA025 and ORCA2 in the Atlantic

Floats can be used to deduce transit times of water masses. When a surface mixed layer criterion is used, the time from the release of a float in a certain region until the mixed layer criterion is met can be interpreted as the time that a water parcel has to travel from its initial position before it reaches the mixed layer and can exchange properties with the atmosphere. If applied to OMZ waters, this timescale can serve as a proxy for the minimal time for feedback processes between changes inside of the OMZs and the mixed layer to take place.

The mixed layer criterion used for floats in this study is a density criterion. Floats are defined as being in the mixed layer if the difference between the density at their instantaneous position and the density at the surface at that position is less than $0.1\,\mathrm{kg\,m^{-3}}$. This criterion has been tested and found to be robust, both different density criteria and fixed-depth mixed-layer-criteria (e.g. $z<50\,\mathrm{m}$) lead to consistent results.

The regional distribution of transit times from 200 m depth to the surface can be shown by floats deployed over a wide area of the Atlantic in 200 m depth (see Figure 4.10 A+B, run ORCA025-AF0ZTCF forward for ORCA025, run ORCA2-AF0ZTCF forward for ORCA2, please see Section 4.6.1 for details). The dark blue area north of 30°N in the northwest is a region where winter mixed layers reach deeper than 200 m. Therefore floats which started here meet the mixed layer criterion quickly because of mixed layer deepening. In the regions just to the south of that dark blue area, intermediate waters are formed. Floats in this region are therefore subducted and only reach the mixed layer much later on the equatorward side of the subtropical cell. Traveling time for that distance can reach years to decades - longer than 20 years in ORCA2.

Even in the tropics, the distribution of transit times is very inhomogeneous. In ORCA2, the eastern tropical North Atlantic region from where floats take longer than 20 years to reach the mixed layer is close to the coast of Ivory Coast, Ghana, Togo, Benin and Nigeria. This region with water older than 20 years is also present in ORCA025, but there it encompasses a much smaller area. In ORCA2, there is also an extended region of transit times to the mixed layer longer than 20 years in the South Atlantic which is not present in ORCA025. Comparison of Figure 4.10 A+B shows that large scale patterns differ between ORCA025 and ORCA2 mainly in the clarity of the regions - while for ORCA2 age gradients are large-scale and coherent, ORCA025 has much more small-scale variability and noise on the transit time fields.

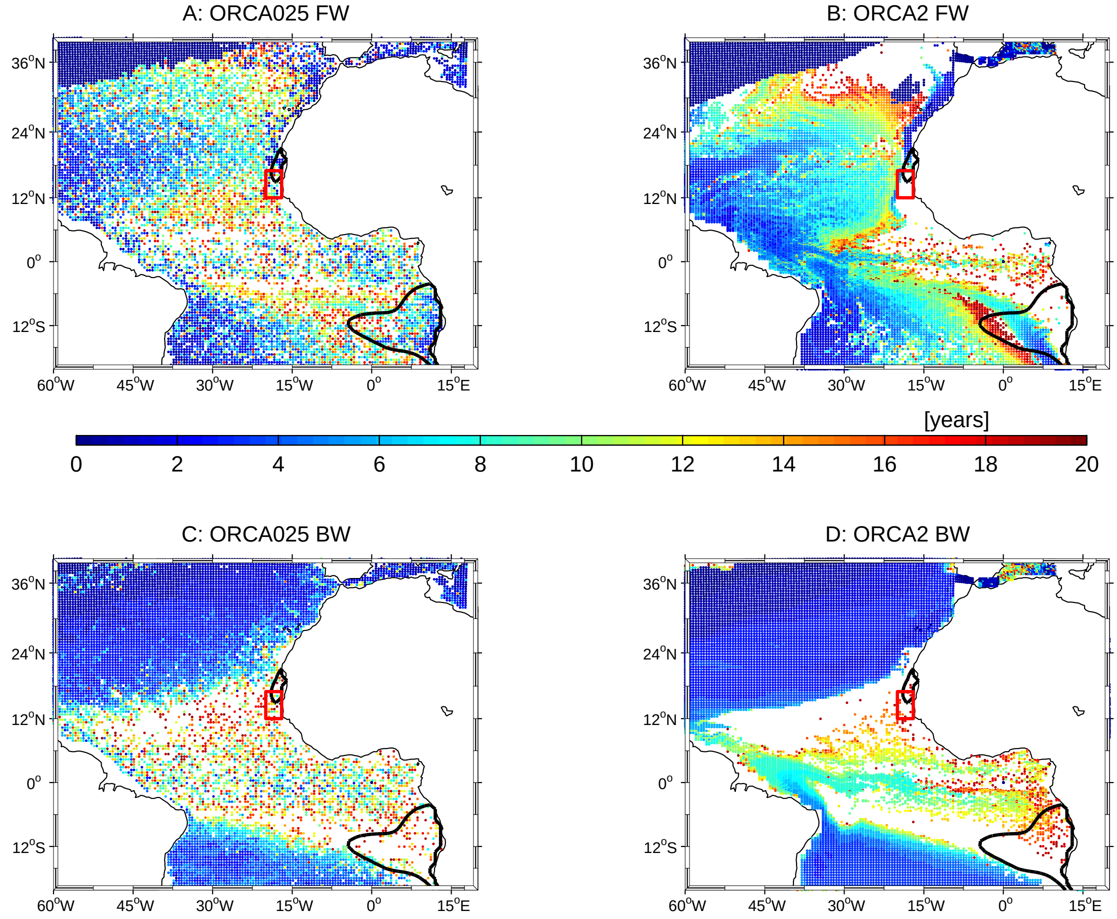

Figure 4.10: Regional distribution of transit times between 200 m depth and the surface mixed layer, calculated from trajectories. Shown are the transit times at the position where floats were started. Note: This figure does not contain any information about where those floats reach the mixed layer. Upper plots for forward calculations ("transit time to mixed layer", A: ORCA025 1985-2004 (ORCA025-AF0ZTCF forward), B: ORCA2 1985-2004 (ORCA2-AF0ZTCF forward)), lower plot for backward calculations ("age", C: ORCA025 2004-1985 (ORCA025-AF0ZTCF backward), D: ORCA2 2004-1985 (ORCA2-AF0ZTCF backward). Colors range from 0 years (dark blue) to 20 years (dark red), white areas are either land or indicate times >20 years. Contours are 80 μmol/l WOA05 annual mean oxygen concentration in 200 m depth (black) and the deployment region of Glessmer et al. [2009] (red).

Additionally to transit times, water age can be deduced from float runs (Figure 4.10 C+D, ORCA025-AF0ZTCF backward and ORCA2-AF0ZTCF backward), with age in this context meaning the time it takes a float to travel between its deployment position and the mixed layer in a run backward in time. While over most of the volume of the OMZs water is older than 20 years, deducing the age of these waters with trajectory experiments cannot be done safely, because on those timescales the influence of diffusion starts playing a dominant role (compare Section 4.3.2).

Similar to transit time fields, age fields show large scale characteristics: A wedge (bounded to the north by a line between Cape Blanc in the northeast and Suriname in the northwest, and to the south by a line between the boarder between Namibia and Angola in the southeast and the easternmost tip of Brazil) contains almost all waters which are older than 10 years at 200 m depth in the Atlantic. Along those boundaries, there are very high age gradients to the outside, and oldest ages are found right along those lines. A younger band exists along the Equator. Maximum extent of areas with waters older than 20 years increase from ORCA025 to ORCA2. Here again the distribution of transit times is much less patchy for ORCA2 than for ORCA025, agreeing with a less turbulent flow field of ORCA2.

In the North Atlantic, there are extended regions where both forward and backward floats take longer than 20 years to reach the mixed layer outside of the 80 μmol/l WOA05 oxygen contour at 200 m, but hardly any inside. Assuming that the OMZs in the model would be somewhat similar to those of WOA05, this shows clearly that the inverse proportionality between water age and oxygen levels does not always hold.

Figure 4.11 shows the percentage of floats released in the Atlantic region with oxygen concentrations below WOA05 80 μmol/l in ORCA2 and ORCA025 that reach the mixed layer over a 20 year run. Shown are curves for one run per year, starting on the x-axis at the time when floats in that run were released. Several different experiments are compared: Firstly, floats that were released at 200 m depth (ORCA2-AFLZOCF and ORCA025-AFSZOCF). Secondly, a passive dye tracer that was released at depth level k=17 (196.7 m to 240 m, ORCA2-ATSVOCF) in ORCA2, and thirdly floats that were released over the same depth range as the tracer for ORCA2 and ORCA025 (ORCA2-AFLVOCF and ORCA025-AFSVOCF).

The problem with a deployment of floats on a constant depth is that this does not take into account the movement of isopycnals which in the real ocean shift the OMZ

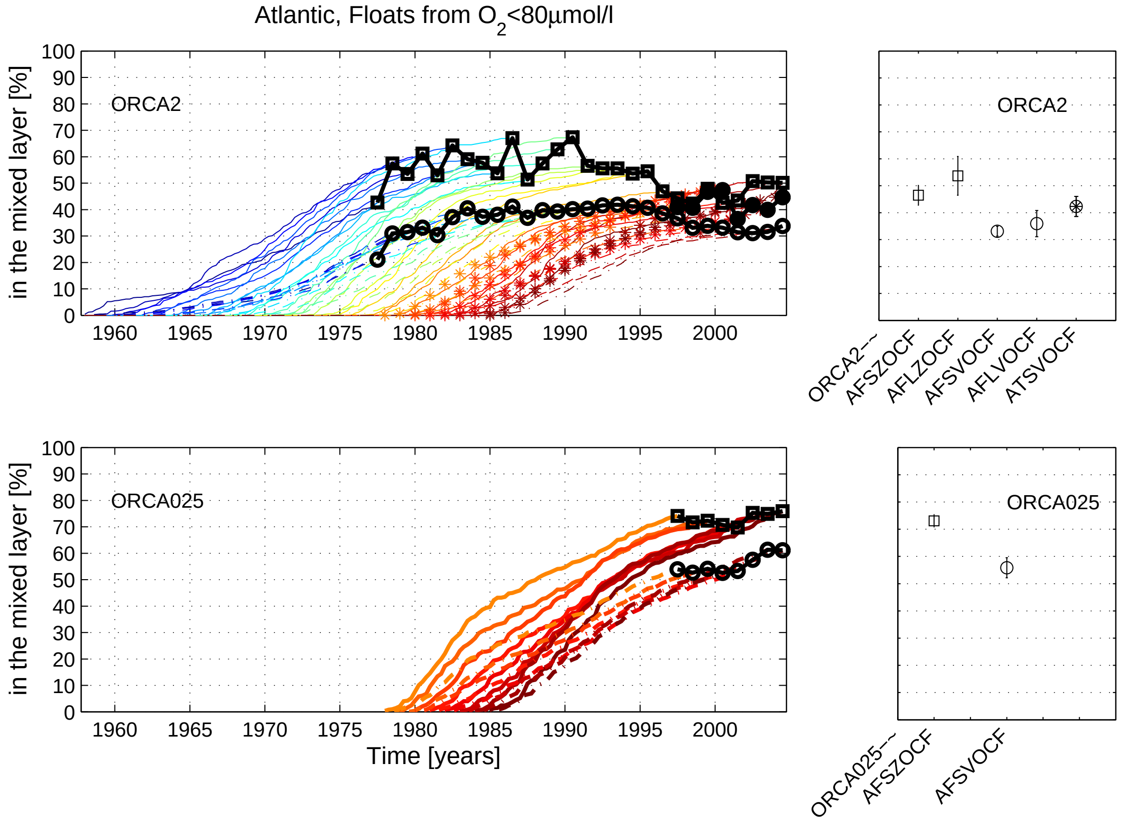

Figure 4.11: Percentage of floats started from the OMZ defined by WOA05 oxygen concentration at 200 m depth in the Atlantic below 80 μmol/l, reaching the surface mixed layer. Upper plots for ORCA2, lower plots for ORCA025. Left plots: Colored lines for different runs started from 1958 to 1985. Solid lines (squares) for floats deployed in 200 m depth, dashed-and-dotted lines (open circles) for floats deployed from 196.7 m to 240 m depth and stars (closed circles) for tracer deployed from 196.7 m to 240 m depth. Black symbols mark the end of the runs after 20 years. They are connected by solid black lines for an easier visual inspection of interannual variability. Right plots: Average values after 20 years of run with errorbars showing ± the standard deviation. ORCA2-AFSZOCF, ORCA025-AFSZOCF, ORCA2-AFLZOCF = Floats deployed at 200 m z-level averaged over the runs started between 1978 and 1985, 1958 and 1985, respectively. ORCA2-AFLVOCF, ORCA2-AFSVOCF, ORCA025-AFSVOCF = Floats deployed over the depth range 196.7 m to 240 m averaged over the runs started between 1978 and 1985, 1958 and 1985, respectively. ORCA2-ATSVOCF = Tracer deployed between 196.7 m and 240 m and averaged over the runs started between 1978 and 1985.

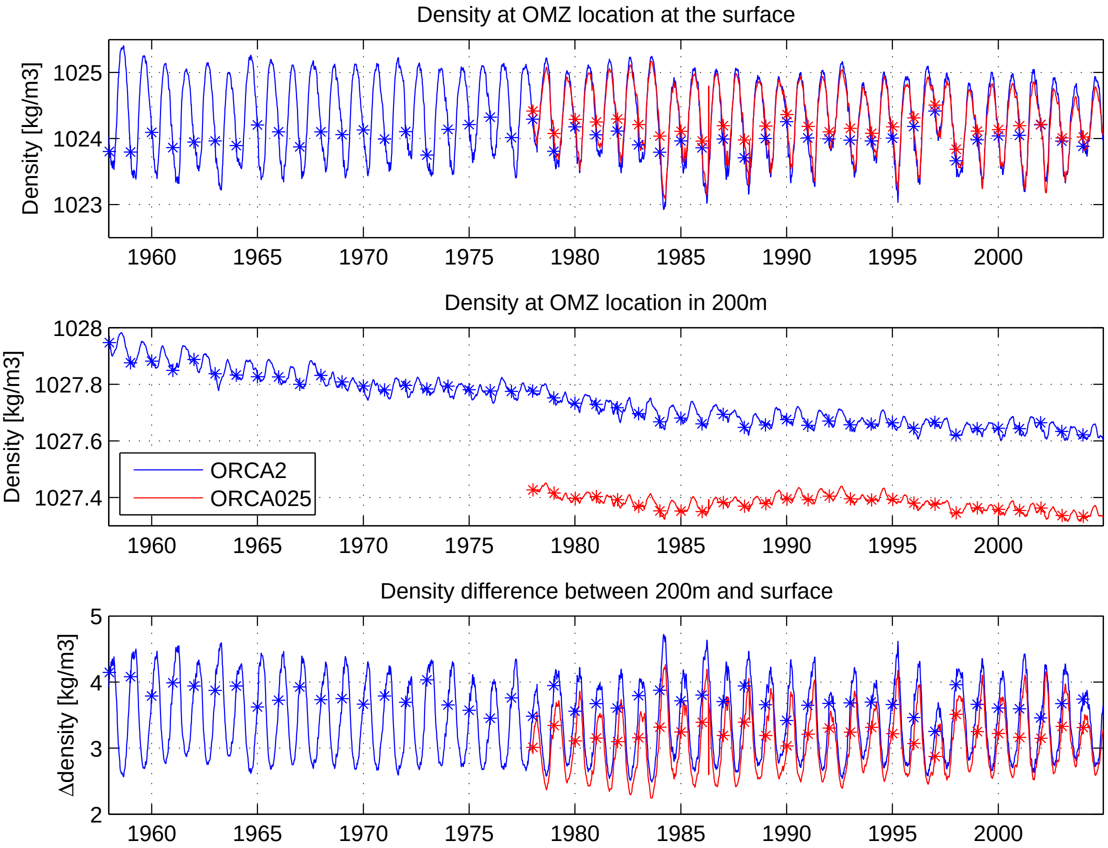

Figure 4.12: Mean density at the surface above the region with WOA05 oxygen concentrations at 200 m below 80 μmol/l in the Atlantic (upper panel), at that region at 200 m depth (middle panel), and the difference of both (lower panel), blue for ORCA2 and red for ORCA025. Stars mark January 15th of each year, the time at which floats/tracer are released.

up and down. Deploying floats on a fixed depth rather than a fixed density therefore potentially introduces a problem, because floats are deployed at different density horizons and hence potentially in very different dynamical regimes. However, in a model density is only defined in discrete steps rather than continuously along the z-axis, so a box is either completely inside or outside a regime, hence specifying the deployment depth over a relationship with density is not feasible. Figure 4.12 shows the density at the region with WOA05 oxygen concentrations below 80 μmol/l in the Atlantic from 1958 to 2004 for both ORCA025 and ORCA2. In both models, density at 200 m displays a drift. However, this drift still corresponds to a vertical range of less than one grid box.

On average, 46 % (± 4 %) of ORCA2-floats released at 200 m depth during the period 1978 to 1985 (ORCA2-AFSZOCF) reach the mixed layer within 20 years. Of the ORCA2-floats released over the volume during the same period, 33 % (± 2 %) reach the mixed layer (ORCA2-AFSVOCF). In case of the tracer, it is 42 % (± 4 %, ORCA2-ATSVOCF). In ORCA025, of the floats released over the same period, 73 % (± 2 %) of the floats released in 200 m depth and 56 % (± 4 %) of the floats released over the volume reach the mixed layer (ORCA025-AFSZOCF and ORCA025-AFSVOCF, respectively). If in case of ORCA2 a longer period including climatological parts of the run is investigated, 54 % (± 7 %) and 38 % (± 9 %) of the floats released in 200 m depth (ORCA2-AFLZOCF) or over the volume (ORCA2-AFLVOCF) respectively, reach the mixed layer within 20 years.

In 6 out of 8 experiments, tracer estimates are higher than the estimates made with floats started from the identical volume. Intuitively, one would expect tracer to reach the mixed layer faster than floats, because additionally to being advected upward, diffusive fluxes should also be upward as long as the tracer gradient is such that the surface concentration of tracer is lower than the concentration at depth. Additionally, tracer is being “sucked” upwards by the gradients artificially created by destroying the tracer near the surface. However, as the tracer is deployed in the middle of the water column, gradients exist both upward and downward, and hence diffusive fluxes occur upward and downward. Those downward diffusive fluxes can on average compensate and potentially even over-compensate the upward diffusive fluxes. This is sketched in Figure 4.13: If laminar advection is the dominant process over eddying velocities acting on floats and tracer, floats are advected with approximately fixed positions relative to each other. In this setting, the center of gravity of the tracer patch moves parallel to the center of gravity of the float cluster. However, additionally to being advected, the tracer is being diffused. So once the floats have passed a certain horizon, floats will seem to have moved faster, because the trail of the tracer is still below that horizon. This holds true even if not all floats and all tracer are in the advective regime, but if only a fraction has separated from the main patch (as depicted in Figure 4.13). Hence interpretation depends on the choice of criterion, i.e. if the center of gravity or a threshold is chosen.

Another possible mechanism is caused by the depth-dependence of vertical diffusivity in the model. Diffusivities are high in the mixed layer, then very low in and below the thermocline and then gradually increase again with depth. When isopycnals on which the tracer is deployed move, the diffusivity on the lower and upper edge of the tracer patch is not necessarily the same throughout the run and

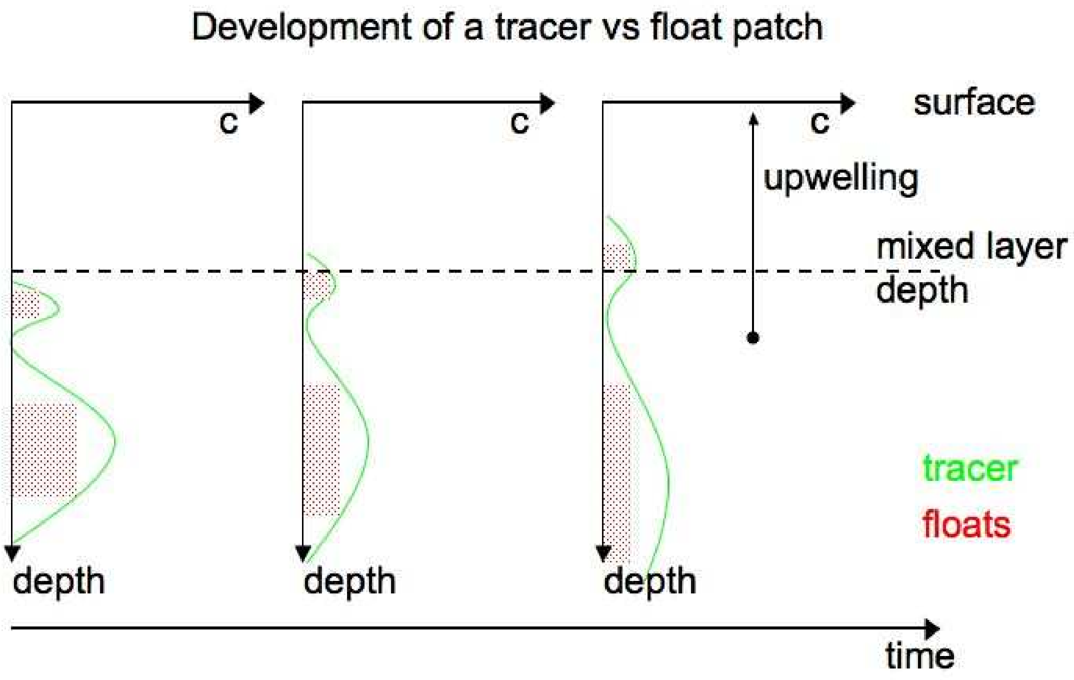

Figure 4.13: Sketch of a possible mechanism explaining how under some circumstances floats can reach the mixed layer faster than tracer: If laminar advection is the dominant process over eddying velocities acting on floats and tracer, floats are advected with approximately fixed positions relative to each other. In this setting, the center of gravity of the tracer patch moves parallel to the center of gravity of the float cluster. However, additionally to being advected, the tracer is being diffused. So once the floats have passed a certain horizon, floats will seem to have moved faster, because the trail of the tracer is still below that horizon. This holds true even if not all floats and all tracer are in the advective regime, but if only a fraction has separated from the main patch (as depicted here). Graphic modified after Tim Fischer, pers. comm., 2010.

between different runs. This can cause the tracer to diffuse stronger downwards in some runs than in others. Since this process does not act on floats they reach the mixed layer faster under these circumstances.

Initial steepness of individual curves in Figure 4.11 is a good indicator for how much tracer and floats will reach the mixed layer within 20 years. This is shown in Figure 4.14: Relative to the years before and after, a year with a relatively high amount of floats or tracer having reached the mixed layer within the first 5 years

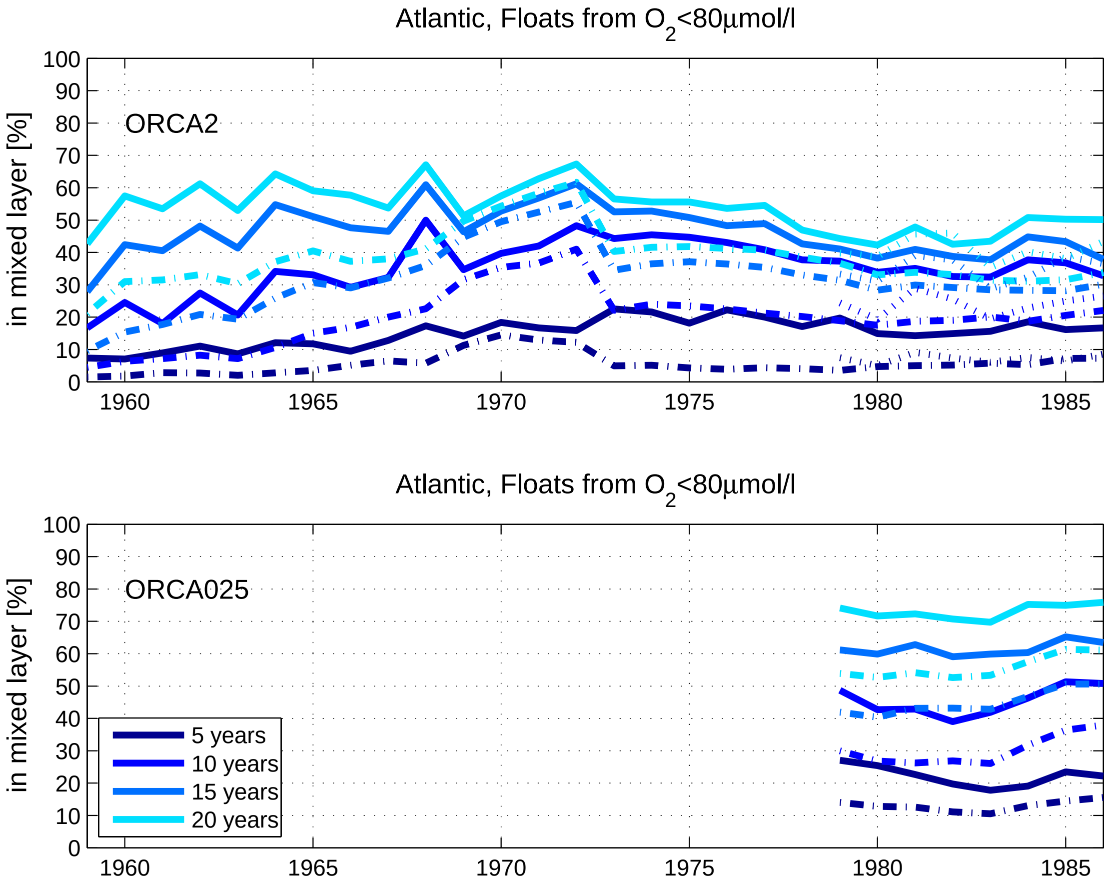

Figure 4.14: Temporal evolution of floats and tracer released in the Atlantic OMZ defined by WOA05 oxygen concentration below 80 μmol/l reaching the mixed layer, upper panel for ORCA2, lower panel for ORCA025. Color scale ranges from dark blue (5 years) progressively lightening in 5 year steps to light blue (20 years). Solid lines represent floats released in 200 m depth (ORCA2-AFLZOCF, ORCA025-AFSZOCF), dashed-and-dotted lines floats released between 196.7 m and 240 m depth (ORCA2-AFLVOCF, ORCA025-AFSVOCF), and dotted lines tracer released between 196.7 m and 240 m depth (ORCA2-ATSVOCF). The x-axis denotes the time at which individual runs were started, subsequent representations of each run are plotted against the time when that run was started.

will also have a relatively high amount of floats and tracer having reached the mixed layer after 20 years. This relationship is especially strong for floats started in 200 m depth in ORCA2 which were deployed between 1958 and 1973, but is also clearly visible for floats deployed over the volume in ORCA2, and for the tracer.

Clearly, if a large percentage of floats or tracer released in a specific year will reach the mixed layer within 20 years is determined very early on. Figure 4.15

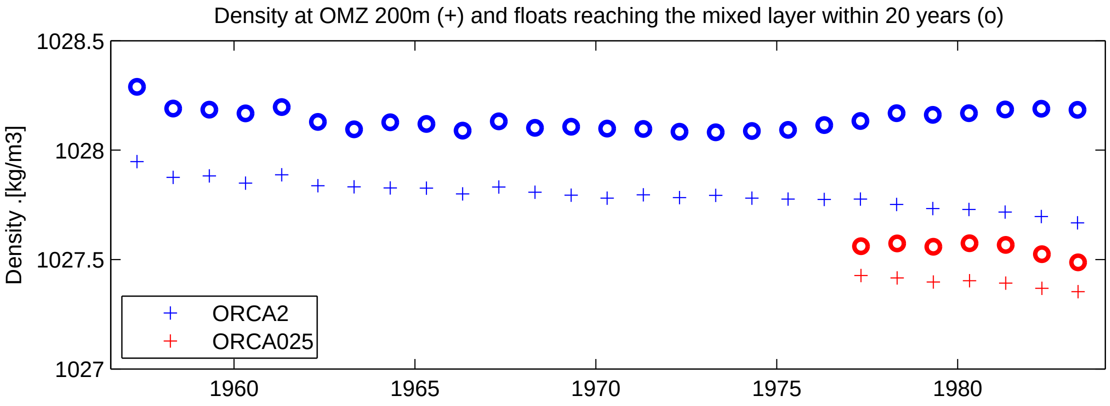

Figure 4.15: Density at the deployment region at each start of a run. Blue stars for ORCA2, red stars for ORCA025. Open circles indicate how many floats have reached the mixed layer within 20 years of their release (ORCA2-AFLVOCF, ORCA025-AFSVOCF), for easier comparability normalized with -1/100+1028.5 in ORCA2 and -1/100+1028.1 in ORCA025 and plotted against the time of their release.

shows the mean density at the deployment region at each year and the percentage of floats reaching the mixed layer within 20 years. This shows that at least for floats released between 1958 and approximately 1968, starting density determines how quickly floats will reach the mixed layer. The strong correlation weakens after approximately 1975. This is caused by the increasing influence of the interannual forcing velocity fields. Forcing is only fully interannual after 1978, hence differences between runs which were mainly run before 1978 are primarily due to the density at 200 m depth and its drift, shown in Figure 4.12, while apart from that each year is more or less similar to the one before. Only when interannual forcing acts on most of the run, other factors than the initial density gain importance.

The interannual variability of the tracer is more closely related to the one of the floats deployed in 200 m depth in ORCA2 than to the floats deployed over a volume in ORCA2, especially after the first approximately 5 years of the run. This suggests that within the first couple of years, when because of the high initial tracer gradients diffusive fluxes of the tracer are especially high, parts of the amount of tracer reach regions dominated by advective processes, where hence the forcing on and the behavior of the floats deployed at 200 m depth and the tracer are largely similar, because diffusive processes are not very important.

In case of ORCA025, interannual variability is smaller than in ORCA2, suggesting that the influence of eddies dampens out signals that are imprinted by the forcing. The temporal development of floats deployed at 200 m depth or over the volume are related, but not similar to each other, as was the case in ORCA2.

Considering the connection of the OMZ region defined by the oxygen below 80 μmol/l in WOA05 in 200 m depth criterion and the mixed layer, the regional distribution of where tracer and floats released in the OMZ reach the mixed layer is very similar between different runs. The main regions can be identified as the eastern boundary and equatorial upwelling systems. The relative contributions of these areas, defined above as the northern, equatorial and southern box and shown in Figure 4.16, to the total amount of floats or tracer reaching the mixed layer stays approximately constant. On average, 75 % (± 9 %) of the floats and tracer reach the mixed layer. The southern box always contributes most, on average 64 % (± 7 %) of the total upwelled floats and tracer. The second biggest contribution comes from the equatorial upwelling with 7 % (± 3 %), and the smallest contribution from the northern upwelling (3 % (± 1 %)). The northern upwelling is mainly fed by the northern OMZ, whereas the equatorial and southern upwelling are fed by the southern OMZ, which in 200 m depth spans an area approximately one order of magnitude larger than the northern OMZ. Together, these three regions explain 75 % (± 11 %) of the total amount of floats and tracer reaching the mixed layer within 20 years (See Figure 4.16 F).

Although the regions where floats reach the mixed layer are largely independent of the model resolution, the pathways to the mixed layer differ. The most noticeable difference is that while in ORCA2 clear pathways and regions in which tracer and floats reach the mixed layer exist, the picture is much more diffused in ORCA025. From the northern OMZ, ORCA2-floats either reach the mixed layer directly in the coastal upwelling above or circle the subtropical gyre and then reach the mixed layer in the equatorial or northern coastal upwelling. The southern ORCA2-floats reach the mixed layer either in the upwelling directly above, or circle the southern subtropical gyre and reach the mixed layer in the equatorial upwelling, or take a direct route into the equatorial undercurrent and surface in the equatorial upwelling. In the ORCA2 tracer run, tracer reaches the mixed layer in a region off Uruguay that does not exist in the ORCA2 float runs. In the tracer case, there seems to be a direct pathway linking the southern OMZ and the blob, going through the equatorial current system and then along the coast of Brazil. In the float runs, floats take the same pathway and pass through the region of the blob, but without reaching the mixed layer there. This is most likely due to the different definitions

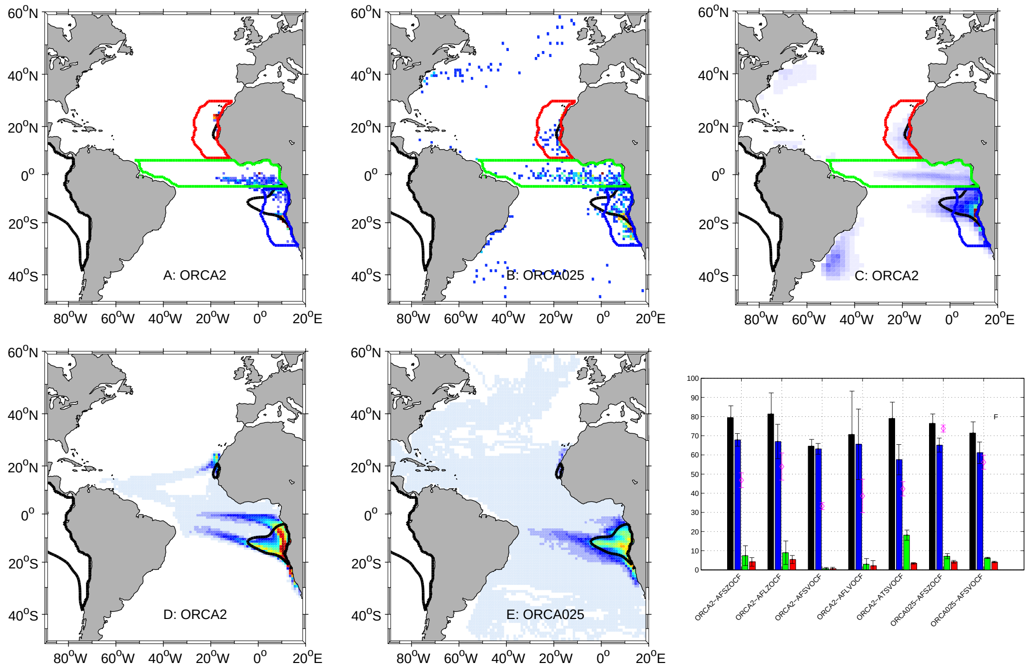

Figure 4.16: Panel A, B and C: Mean amount of floats/tracer (deployed within the black contour, i.e. WOA05 oxygen concentration = 80 μmol/l) reaching the mixed layer within 20 years from the release in the Atlantic OMZ in 200 m depth, gridded on a 1°×1° grid and normalized. Colors range from white (no floats/tracer reach the mixed layer in this grid box) to red (maximum amount of floats/tracer). Panel A: Floats in ORCA2, Panel B: Floats in ORCA025, Panel C: Tracer in ORCA2. Red, green and blue contours indicate the northern, equatorial and southern box used in Panel F. Panel D and E: Mean depth-integrated path density map between the OMZ and the mixed layer, counted every three days on a 1°×1° grid, corresponding to the runs shown in Panel A and B. Colors range from white (no float ever crossed that grid box) to red (highest number of floats crossing). Color scale is normalized with the number of floats in both panels. Panel D for ORCA2, Panel E for ORCA025. Panel F (for an enlarged version of this panel see Figure 4.24): Magenta diamonds: Average amount of floats/tracer having reached the mixed layer after 20 years of run with errorbars showing the standard deviation (Compare Figure 4.11). Contribution of the different boxes to the total amount of floats/tracer having reached the mixed layer within 20 years; relative to the values shown in magenta as 100 %: Black bars denote the total that can be explained by the three boxes, blue bars show the contribution of the southern box, green bars of the equatorial box and red bars of the northern box. (Note: While the magenta diamonds and errorbars denote the percentage relative to the total number of floats deployed in the OMZ, the colored bars and errorbars show the percentage relative to the value of the magenta diamond as 100 %.)

of the mixed layer for floats and tracer. That blob is rudimentary existent in the ORCA025 run. ORCA025-floats have more diverse pathways than ORCA2-floats. Although the pathways described for ORCA2 exist, floats are by no means restricted to them (See Figure 4.16 E). ORCA025-floats also reach the mixed layer in the Gulf Stream extension and in the South Atlantic off Uruguay.

In the Atlantic Ocean, interannual variability of the connection of the OMZ and the mixed layer (see Figure 4.11) is determined by the variability of the southern OMZ because of its much larger size. In the northern OMZ, interannual variability is very large for ORCA2, and here it does matter if floats are deployed at 200 m depth or over the 196.7 m to 240 m depth range. If floats that started during the period 1958 to 1985 are considered, 62 % (±23 %) of the floats deployed at 200 m depth, and 20 % (±27 %) of the floats deployed over the volume, reach the mixed layer within 20 years. If only looking at floats deployed between 1978 and 1985 (which is the period for which actual interannually varying forcing, and also ORCA025 data exists), 41 % (±23 %) of the z-level-floats reach the mixed layer compared to 2 % (±4 %) of the floats deployed over the volume. The interannual variation of volume- and z-level-floats looks very similar, however the relative amplitude is much bigger for the floats deployed over a volume. The percentage of floats having reached the mixed layer is highly correlated with the density at the time of their release, both at that depth and at the surface above. What influences the density in the western subtropical Atlantic could not be determined. There are some studies that found it to be correlated with STC strength or meridional overturning (see Kröger et al. [2005]; Rabe et al. [2008]), but neither could be shown here. Another guess would be the local wind stress, but that does not seem to be the case either. In the case of ORCA025, of the floats deployed between 1978 and 1985, 80 % (±8 %) of the floats deployed at 200 m depth reach the mixed layer within 20 years, and 71 % (±4 %) of the floats deployed over a volume. The shape of the upwelling curves of ORCA2 and floats deployed at 200 m in ORCA025 show similar interannual behavior, the floats deployed over the volume in ORCA025 behave differently. Neither upwelling of floats deployed at 200 m depth nor of floats deployed over the volume are correlated with the local density at the time of their release, nor with local wind fields. What determines the interannual variability for the ORCA025 floats could not be found.

In the southern OMZ, although the interannual variability of the connection between the OMZ and the surface ocean seems qualitatively similar for floats deployed at 200 m depth and floats deployed over a volume, only floats deployed in ORCA2 at 200 m depth seem to be correlated to density at the time of their deployment. In the case of ORCA025, there is no correlation.

4.4.3 Comparison with the Pacific

Many characteristics of the connection of the Pacific OMZ to the upper ocean are similar to the Atlantic case, hence this section concentrates on pointing out the differences.

Figure 4.17 shows the percentage of floats that reach the mixed layer over a 20 year run. Shown are curves for one run per year, starting on the x-axis at the time when floats in that run were released. Several different experiments are compared: Firstly, floats that were released at 200 m depth in the Pacific region with WOA05 oxygen concentrations below 10 μmol/l in ORCA2 and ORCA025 (ORCA2-PFSZOCF, ORCA025-PFSZOCF, ORCA2-PFLZOCF). Secondly, a passive dye tracer that was released at k=17 (196.7 m to 240 m) in ORCA2 (ORCA2-PTSVOCF), and thirdly floats that were released over the same depth range as the tracer for ORCA2 and ORCA025 (ORCA2-PFLVOCF, ORCA2-PFSVOCF, ORCA025-PFSVOCF).

As in the Atlantic Ocean, here again tracer and float based estimates of the connection of the OMZ with the upper ocean agree better than in GEO09. Of floats released over the period 1978 to 1985 in 200 m depth in ORCA2, 90 % (±6 %) reach the mixed layer within 20 years, as compared to 56 % (±18 %) of the tracer and 55 % (±13 %) of the floats deployed over the same volume as the tracer. For ORCA025, 80 % (±12 %) of the floats released at 200 m and 74 % (±17 %) of the floats released in the volume reach the mixed layer. As in the Atlantic case, using floats released over the longer period (1958 to 1985) leads to bigger standard deviations: 80 % (±15 %) in case of the floats released at 200 m depth, and 45 % (±18 %) for floats released over the volume. The amount of floats and tracer reaching the mixed layer in the Pacific Ocean are bigger than in the Atlantic over the same period. Also, interannual variability is substantially higher in the Pacific.

In order to investigate in which regions floats and tracer reach the mixed layer, boxes are defined: The region between the western coast of America and 10° west of the coast between 6°N and 30°N (northern box) and 6°S and 30°S (southern box) as well as the whole width of the Pacific Ocean from 6°S to 6°N (equatorial box) and the box offshore of the northern box, ranging from 6°N to 20°N to 180°W (Costa Rica Dome box, all boxes shown in Figure 4.18). In all float runs, the box in

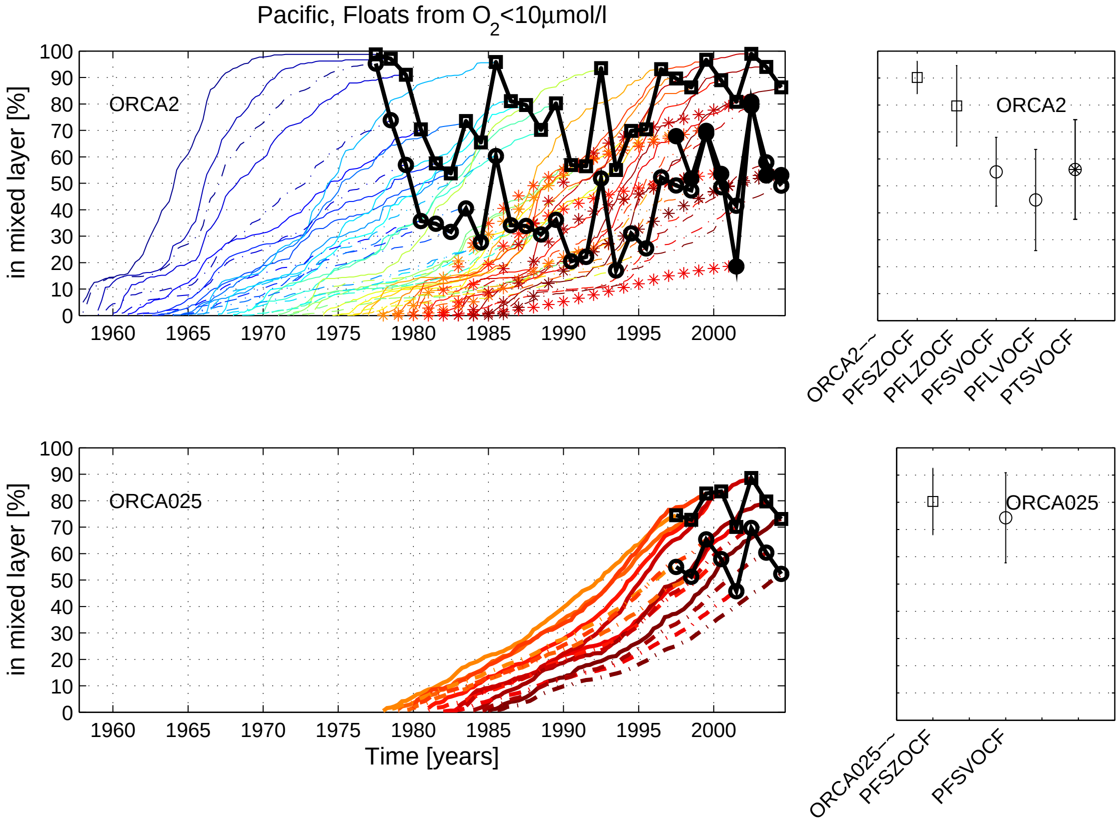

Figure 4.17: Percentage of floats started from the OMZ defined by WOA05 oxygen concentration at 200 m depth in the Pacific below 10 μmol/l, reaching the surface mixed layer. Upper plots for ORCA2, lower plots for ORCA025. Left plots: Colored lines for different runs started from 1958 to 1985. Solid lines (squares) for floats deployed in 200 m depth, dashed-and-dotted lines (open circles) for floats deployed from 196.7 m to 240 m depth and stars (closed circles) for tracer deployed from 196.7 m to 240 m depth. Black symbols mark the end of the runs after 20 years. They are connected by solid black lines for an easier visual inspection of interannual variability. Right plots: Average values after 20 years of run with errorbars showing ± the standard deviation. ORCA2-PFSZOCF, ORCA025-PFSZOCF, ORCA2-PFLZOCF = Floats deployed at 200 m z-level averaged over the runs started between 1978 and 1985, 1958 and 1985, respectively. ORCA2-PFLVOCF, ORCA2-PFSVOCF, ORCA025-PFSVOCF, = Floats deployed over the depth range 196.7 m to 240 m averaged over the runs started between 1978 and 1985, 1958 and 1985, respectively. ORCA2-PTSVOCF = Tracer deployed between 196.7 m and 240 m and averaged over the runs started between 1978 and 1985.

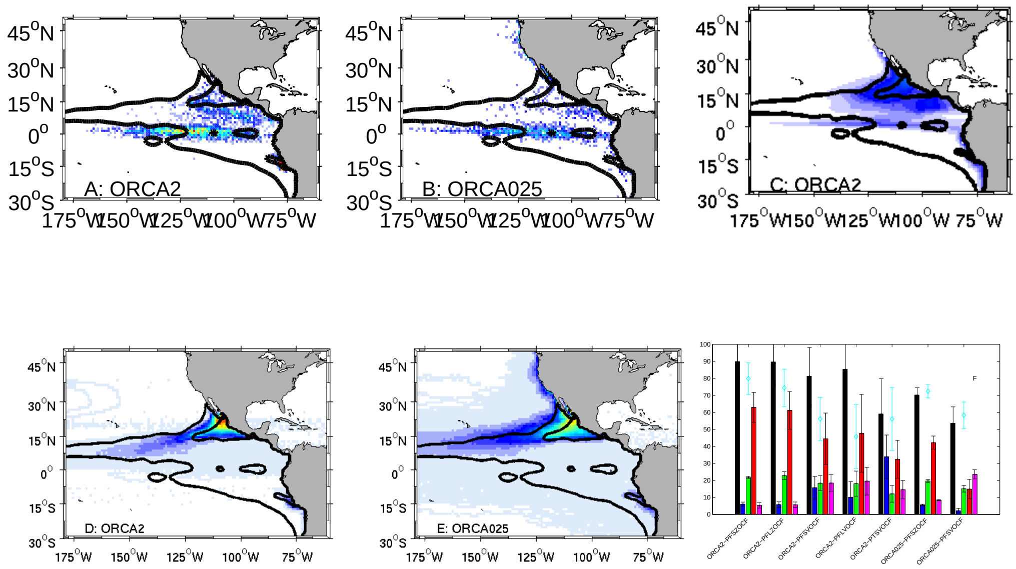

Figure 4.18: Panel A, B and C: Mean amount of floats/tracer reaching the mixed layer within 20 years after the release in the Pacific OMZ, gridded on a 1°×1° grid and normalized. Panel A: Floats in ORCA2, Panel B: Floats in ORCA025, Panel C: Tracer in ORCA2. Red, green and blue contours indicate the northern, equatorial and southern box used in Panel F. Panel D and E: Depth-integrated, averaged way floats take from the OMZ to the mixed layer, counted every three days on a 1°×1° grid. Colors range from white (no float ever crossed that grid box) to red (highest number of floats crossing). Color scale is normalized with the number of floats in both panels, respectively. Panel D for ORCA2, Panel E for ORCA025. Panel F (for an enlarged version of this panel see Figure 4.25): Cyan diamonds: Average amount of floats/tracer having reached the mixed layer after 20 years of run, with errorbars showing the standard deviation. Contribution of the different boxes to the total amount of floats/tracer having reached the mixed layer within 20 years; 100 % are the values shown in cyan: Black bars denote the total that can be explained by the four boxes, blue bars show the contribution of the southern box, green bars of the equatorial box, red bars of the northern box and magenta of the Costa Rica Dome box. (Note: While the cyan diamonds and errorbars denote the percentage relative to the total number of floats deployed in the OMZ, the colored bars show the percentage relative to the value of the cyan diamond as 100 %.)

which most floats reach the mixed layer is the northern box. This is equivalent to findings for the Atlantic Ocean, where the coastal upwelling close to the bigger OMZ contributed most. As for the tracer, the box in which most of the tracer reaches the mixed layer is the Costa Rica Dome box, clearly indicating the importance of diffusive processes - enhanced by the destruction of tracer at the surface - in that region. The floats and tracer that reach the mixed layer in that region are the ones that potentially form the closest link between zones of low oxygen concentrations with active denitrification in the water column and regions of nitrogen fixation.

In the Pacific Ocean, the difference in the spatial extent of the northern and southern OMZ is not as large as in the Atlantic Ocean, but in 200 m depth the area of the northern OMZ is still 6 times larger than that of the southern OMZ. In case of the southern OMZ, the percentage of floats that reach the mixed layer within 20 years of their release is strongly inversely correlated with the density, both at the depth of their release and at the surface above, at their time of release. High densities at the deployment lead to low percentages of floats reaching the mixed layer within 20 years. Two distinct dynamical states, linked to the El Niño-La Niña cycle, can be separated: In the "upwelling" state, densities are high and floats from the OMZ off Peru are directly drawn upward and all floats have reached the mixed layer in the coastal upwelling within 15 years. In the other state, densities are low and only about 60 % of the floats reach the mixed layer within 20 years. Floats that do not reach the mixed layer on those timescales behave clearly differently from all floats that reach the upwelling in both states: They stay at their depth horizon and start drifting southward in the poleward undercurrent (Peru-Chile-UnderCurrent) which is known to be saltier, richer in nutrients and lower in oxygen than surrounding waters, and stronger at the onset of El Niños (Strub et al. [1998]).

In case of the northern OMZ, the percentage of floats that reach the mixed layer within 20 years of their release is strongly inversely correlated with the density at the depth and time of their release. However, those densities at the deployment position are not correlated to El Niño as in the southern OMZ.

Why in ORCA2 floats and tracer reach the mixed layer at approximately the same rate, while in GEO09 the tracer reached the mixed layer twice as fast as the floats did can be investigated in simple 1-dimensional (1D) experiments. Theoretically, advective and diffusive transports can be calculated sequentially. In a simple 1D model, diffusion can be applied on top of the already advectively distributed, horizontally integrated float concentration for the corresponding time. When dis-

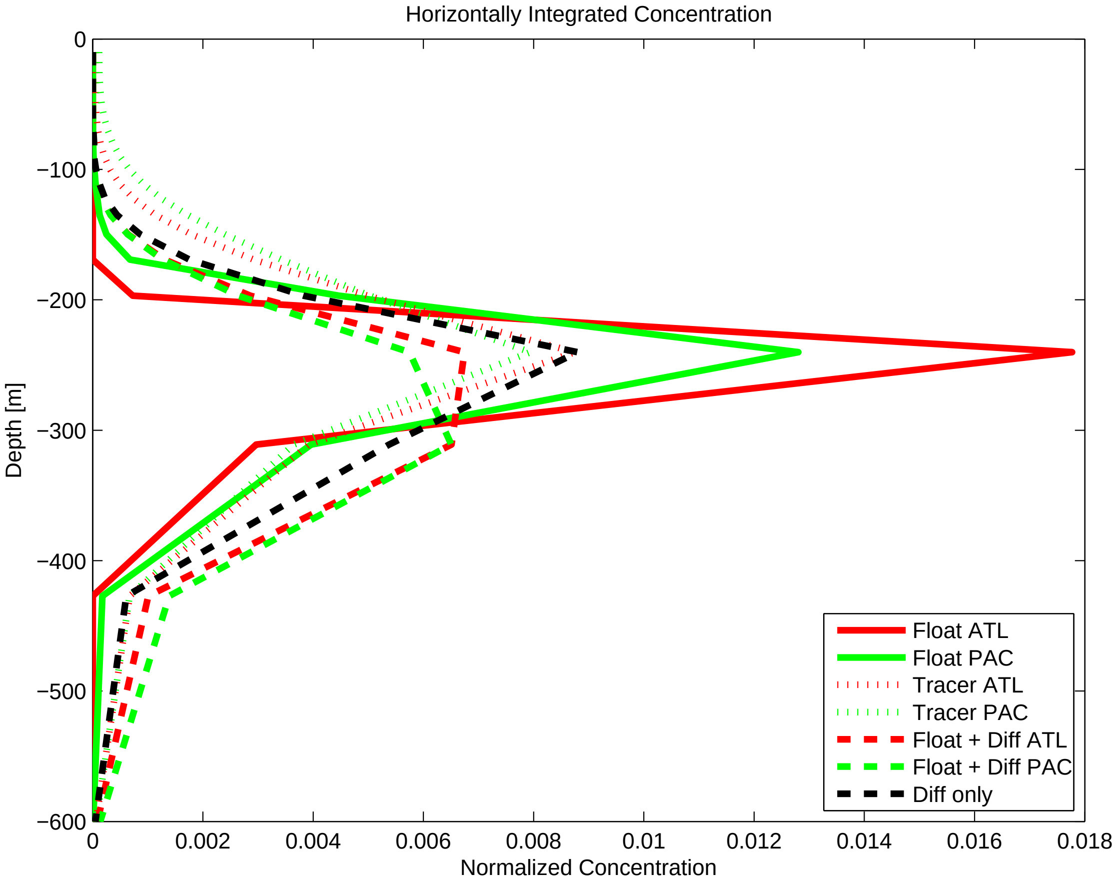

Figure 4.19: Horizontally integrated concentrations of floats (solid lines) and tracer (dashed lines) 1 year after their release in the Atlantic (red) and Pacific (green) OMZ. Dotted lines indicate float profiles after 1 year with the equivalent amount of diffusion applied in a simple 1D model. The black dotted line is a tracer distribution that has been purely diffused in the 1D model from the initial tracer profile.

cussing those 1D experiments one has to keep in mind that several far-reaching assumptions have been made. Firstly, that horizontal integration of float or tracer concentrations is valid, i.e. that the mixing induced by averaging on z-levels rather than on isopycnals is small compared to the fluxes that are being investigated in those experiments. This can - but does not have to be - the case. In the OMZ areas and depths if concentrations are examined 1 year after their release this can be assumed.

After 1 year the tracer has spread over a wider depth range than the floats (see Figure 4.19), suggesting it should reach the mixed layer faster. If on the horizontally averaged float concentration an additional year of diffusion is applied, the profile becomes very similar to a purely diffused tracer patch. This indicates that diffusive processes are more important than advective. This new profile has a broader peak than the float profiles, but is shifted downward compared to the float profiles and the modelled, horizontally integrated tracer profile. This analysis has been done using a constant diffusivity coefficient ($0.1 \times 10^{-4}\,\mathrm{m}^2\,\mathrm{s}^{-1}$) which is a good approximation in the region of the tracer patch. Differing from GEO09 where on horizontally integrated float concentrations 2.5 times the explicit diffusivity had to be applied, little implicit diffusion seems to act here. Intuitively it makes sense that tracer is faster in the mixed layer than floats in the beginning of the run, but then at some point floats have to catch up. This happens at different times in different cases.

4.4.4 Connection under doubling atmospheric CO_2 concentration

Under the assumption that the time it takes floats that were released in the OMZ to reach the mixed layer as introduced above is a good diagnostic for the closeness of the link between the OMZ and the mixed layer, and hence an indicator for the closeness of the feedback between changes in OMZ's nitrate-to-phosphate ratios and changes in the upper-ocean ecosystem, this diagnostic can be used to forecast.

In order to be able to use the coupled ocean-atmosphere model, it has to be shown that it behaves reasonably similar to the ocean-only model. This has partly been done in Park et al. [2009], and in Figure 4.20 the interannual variability of the connection between the OMZ and the mixed layer is shown (H08-AF0VOCF and H08-PF0VOCF). For both the Atlantic and Pacific Ocean, the results of the coupled run agree well with the results of the ocean-only runs presented in Section 4.4.2 for the Atlantic and Section 4.4.3 for the Pacific Ocean. In the coupled model, the mean connection is a little weaker than in the ocean-only runs. This can be due to the shorter averaging period of the ocean-only results - in the coupled runs periods of 8 years with similar results to the ocean-only runs can be found.

If the control run is accepted as a reasonable mean state, and under the assumption that the OMZs in the global warming run are still well represented by WOA05 oxygen fields and the criteria outlined in Section 4.3.4, predictions can be made. In a 100 year coupled ocean-atmosphere-model run, atmospheric CO_2 is increased by 1 % per year until doubling is reached after 70 years, and then stabilized. The last 18 years of this run are used for analysis here. Because of the shortness of the record, only the average over the first 10 years of float runs can be shown here.

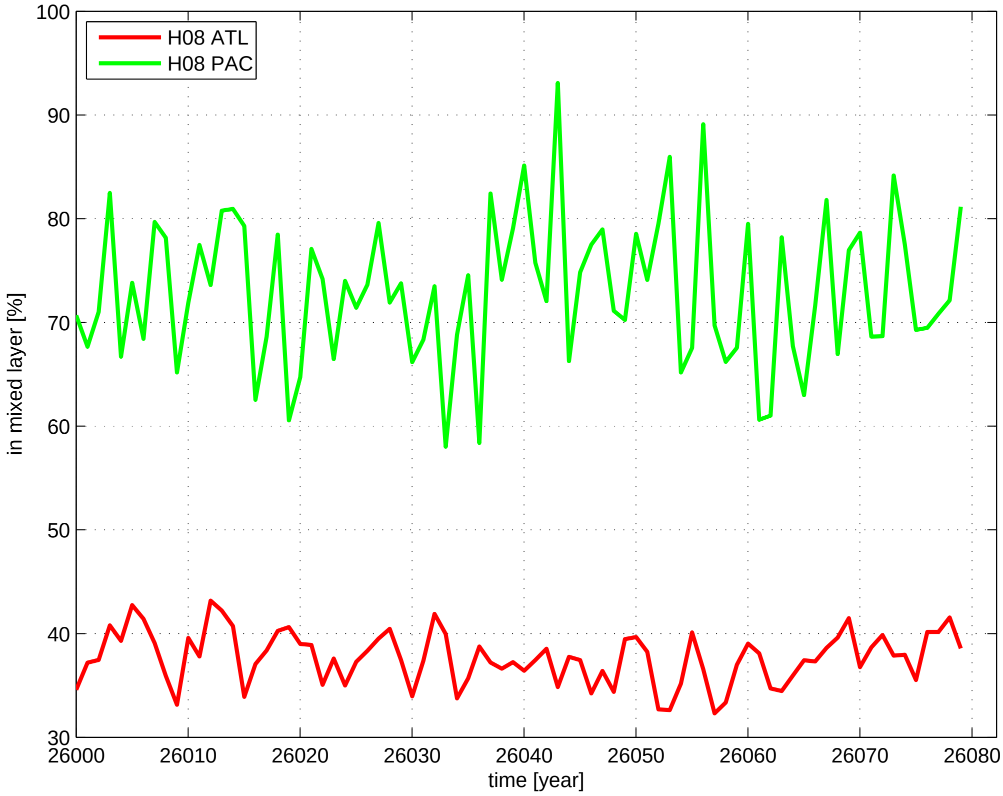

Figure 4.20: Interannual variability of the connection between the OMZs and the mixed layer in the control coupled atmosphere-ocean model run. Red curve: H08-AF0VOCF, green curve: H08-PF0VOCF.

On average, after 10 years they show a weakening of the connection by 50 % in the Atlantic, and a weakening of 2/3 in the Pacific (see Figure 4.21). This can be linked to the weakening strength of the northern hemisphere STC in the Pacific Ocean, which leads to a more sluggish ventilation of the North Pacific STC, while the Atlantic STC strength increases. But as the volume of the North Pacific OMZ is much larger than that of the South Pacific OMZ, the total signal is still dominated by a weakening of the connection. In the Atlantic, both STC strengths are decreasing (W. Park, pers. comm. 2010). Additional runs are currently being done.

4.5 Summary and conclusions

In this paper, the connection between OMZs and the surface mixed layer is investigated in models of different horizontal resolutions. Methods that were used in a high resolution model in a study by Glessmer et al. [2009] (called GEO09) are

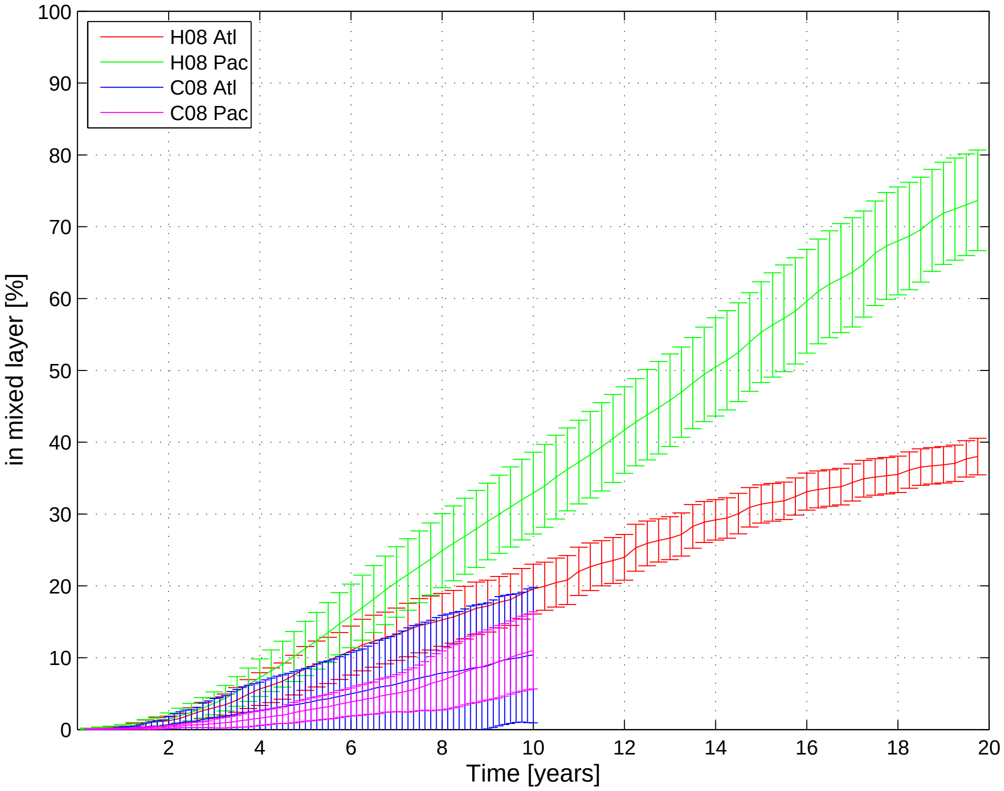

Figure 4.21: Mean ± standard deviation of the percentage of floats deployed in the Atlantic (red+blue) and Pacific (green+magenta) OMZ reaching the mixed layer over 20 years, under present climate (red+green) and under a CO_2-doubling scenario (blue+magenta).

applied to an eddy-permitting and a non-eddy-resolving model, and results of the different resolutions are compared. Although the general flow fields of the models are similar, and especially upwelling transports agree well, the closeness of the connection between the OMZs and the mixed layer is different from the results of GEO09. Although a dependence of the closeness of the link on model resolution was expected and found, no systematic relationship appears to exist.

Different strategies to force float calculations are discussed, and it is found that it is - especially in the 2° resolution model - advisable to use continuous forcing fields rather than repeatedly use single years to force longer runs. Comparing tracer and float estimates shows that, after 20 years, they agree much better than they did in GEO09. However, as shown in Figure 4.22 in the Pacific big differences exist in the coarse resolution model, too. After an initial period of approximately 10 years where the tracer is faster in reaching the mixed layer than both float runs, both float runs catch up. Intuitively it makes sense that tracer initially reaches the mixed layer faster than floats (additionally to the upward advection it is also driven by upward diffusion, which is even enhanced by the destruction of tracer at the surface - a process that cannot be similarly applied to floats), however at some point all floats and all tracer will have reached the mixed layer, so there has to be a period where more floats than tracer reach the mixed layer. In the Atlantic, tracer estimates are always slightly - but never substantially - higher than the corresponding float estimates.

In a study of the Atlantic Ocean a large interannual variability of the connection between the OMZ and the mixed layer is found that had not been expected from the results of GEO09. However, those interannual fluctuations are found to be closely correlated with the density at which floats where deployed.

In the Pacific Ocean, the interannual variability could partly be related to El Niño states. Floats that started in the OMZ during years with a strong density stratification were much less likely to reach the mixed layer within the following 20 years than floats that were started during less stratified years. Surprisingly, the connection between the Pacific OMZ and the mixed layer is much stronger in both models than that of the Atlantic OMZ at the same depth. This indicates that although the Pacific OMZ is much more intense and closer to the surface, other processes than the ventilation must determine the strength of the OMZ.

In a coupled atmosphere-ocean model, the connection between the Atlantic and Pacific OMZs and the mixed layer were investigated after it had been shown that the mean state of the present day simulations of this coupled model agrees well with the ocean only model. This analysis shows that the connection weakens under global warming, suggesting an enhanced isolation of the OMZ from the upper ocean. This can be explained by the strength of the subtropical cells, which are much weaker under global warming.

All results of this paper depend on the definition of OMZs that are taken to be similar to those of WOA05. From the data available this is the best possible definition, however future work should include examining different criteria to define the OMZ. For example, model runs including age tracers can be used to find the least-ventilated regions, and models including biogeochemistry and oxygen can provide actual OMZs, to support the results of this study.

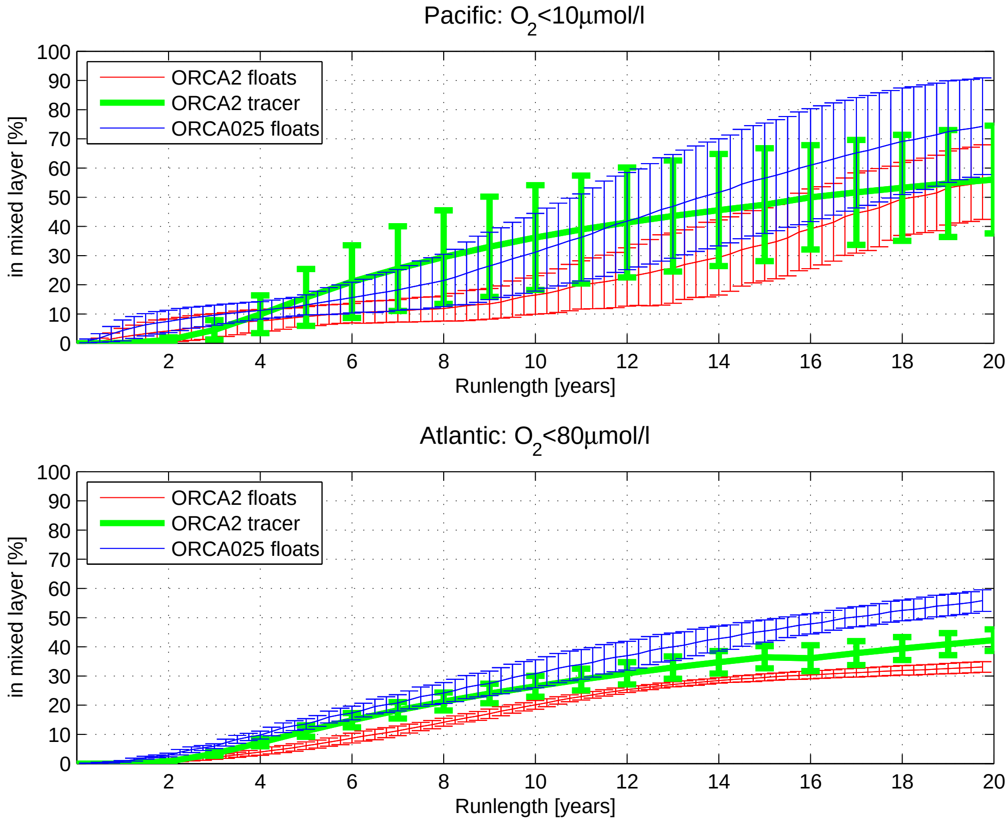

Figure 4.22: Comparison of float and tracer estimates: Mean percentage (± errorbars) of floats and tracer released in the Atlantic and Pacific OMZ reaching the mixed layer over a period of 20 years.

4.6 Appendix

4.6.1 Overview over float and tracer runs used in this study and their naming convention

Float and tracer runs are named following a specific naming convention, depicted in Figure 4.23. Names include, in the following order, information on

- which model was used to calculate the tracer/floats (FLAME, ORCA025, ORCA2)
- in which ocean the experiment took place (A=Atlantic, P=Pacific)
- if it was a tracer or float experiment (T=tracer, F=float)

- the length of the period over which runs were started (L=long=1958-1985, S=short=1978-1985, 0=climatological FLAME run or one single run or climate model runs)
- the depth of the deployment (Z=200 m, V=196.7-240 m, D=196.7-311 m)
- the horizontal deployment region (O=WOA05 oxygen criterion (oxygen concentration less than 10 μmol/l in the Pacific Ocean and less than 80 μmol/l in the Atlantic Ocean), B=box as in Glessmer et al. [2009], T=wide range in the Atlantic)
- forcing strategy (C=continuous, R=recycled)
- the type of run (N=online, F=offline).

The run ORCA025-AFLZOCF for example would be a continuous offline float run done in the Atlantic in ORCA025, with individual floats released each year from 1958 to 1985 at 200 m depth in the region where WOA05 oxygen is below 80 μmol/l. All runs are listed with their name and run details in Table 4.1.

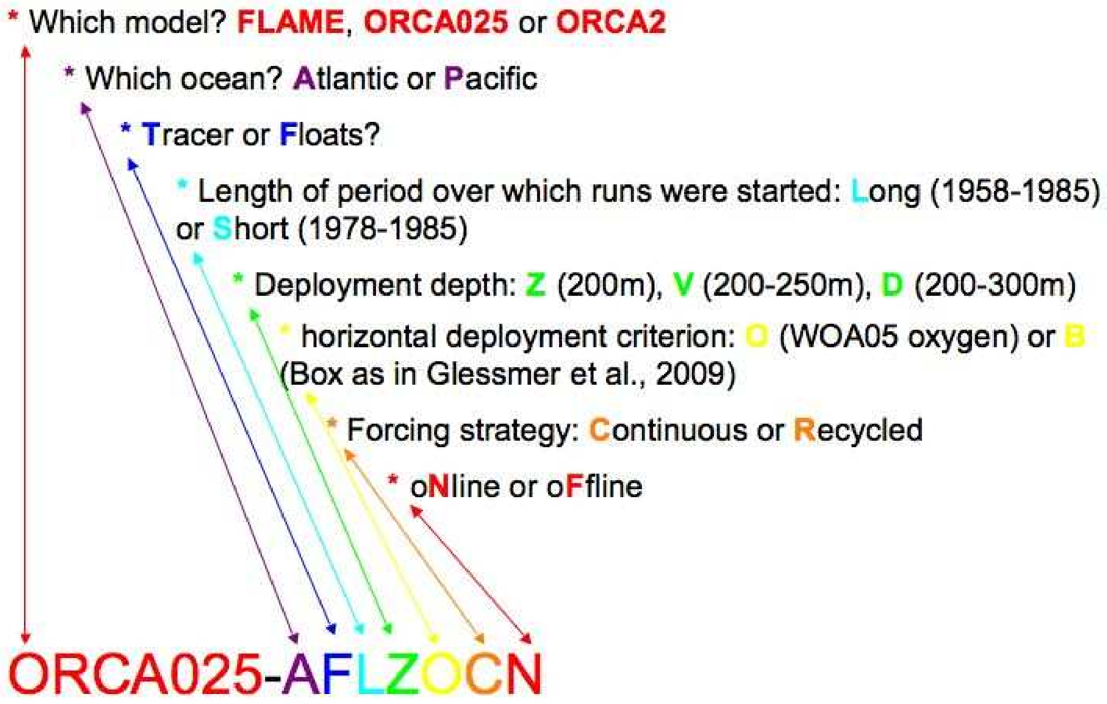

Figure 4.23: Naming convention float and tracer runs. For details please refer to Section 4.6.1.

experiment name	model	ocean	tracer or floats	online or offline	deployment position	deployment depth	forcing period
FLAME-AF0ZBRF	FLAME	Atlantic	float	offline	17°W-20°W, 12°N-17°N	200 m	20 years from a climatological run
ORCA025-AFSZBCF	ORCA025	Atlantic	float	offline	17°W-20°W, 12°N-17°N	200 m	eight runs, 1978-1997, 1979-1998, .. 1985-2004
ORCA025-AFSZORF	ORCA025	Atlantic	float	offline	within WOA05 80 μmol/l O_2 at 200 m	200 m	eight runs, 20 times repeating each of 1985, 1986, .. 1992
ORCA025-AFSZOCF	ORCA025	Atlantic	float	offline	within WOA05 80 μmol/l O_2 at 200 m	200 m	eight runs, 1978-1997, 1979-1998, .. 1985-2004
ORCA025-PFSZOCF	ORCA025	Pacific	float	offline	within WOA05 10 μmol/l O_2 at 200 m	200 m	eight runs, 1978-1997, 1979-1998, .. 1985-2004
ORCA025-AF0ZTCF	ORCA2	Atlantic	float	offline	Atlantic	200 m	1985-2004 or 2004-1985
ORCA025-AFSVOCF	ORCA025	Atlantic	float	offline	within WOA05 80 μmol/l O_2 at 200 m	196.7 m - 240 m	eight runs, 1978-1997, 1979-1998, .. 1985-2004
ORCA025-PFSVOCF	ORCA025	Pacific	float	offline	within WOA05 10 μmol/l O_2 at 200 m	196.7 m - 240 m	eight runs, 1978-1997, 1979-1998, .. 1985-2004
ORCA2-AFSZBCF	ORCA2	Atlantic	float	offline	17°W-20°W, 12°N-17°N	200 m	eight runs, 1978-1997, 1979-1998, .. 1985-2004

Continued on next page

experiment name	model	ocean	tracer or floats	online or offline	deployment position	deployment depth	forcing period
ORCA2-AFSZORF	ORCA2	Atlantic	float	offline	within WOA05 80 μmol/l O_2 at 200 m	200 m	eight runs, 20 times repeating each of 1985, 1986, .. 1992
ORCA2-AF0ZTCF	ORCA2	Atlantic	float	offline	Atlantic	200 m	1985-2004 or 2004-1985
ORCA2-AFSZOCF	ORCA2	Atlantic	float	offline	within WOA05 80 μmol/l O_2 at 200 m	200 m	eight runs, 1978-1997, 1979-1998, .. 1985-2004
ORCA2-PFSZOCF	ORCA2	Pacific	float	offline	within WOA05 10 μmol/l O_2 at 200 m	200 m	eight runs, 1978-1997, 1979-1998, .. 1985-2004
ORCA2-AFSVOCF	ORCA2	Atlantic	float	offline	within WOA05 80 μmol/l O_2 at 200 m	196.7 m - 240 m	eight runs, 1978-1997, 1979-1998, .. 1985-2004
ORCA2-PFSVOCF	ORCA2	Pacific	float	offline	within WOA05 10 μmol/l O_2 at 200 m	196.7 m - 240 m	eight runs, 1978-1997, 1979-1998, .. 1985-2004
ORCA2-AFLZOCF	ORCA2	Atlantic	float	offline	within WOA05 80 μmol/l O_2 at 200 m	200 m	28 runs, 1958-1977, 1959-1978, .. 1985-2004
ORCA2-PFLZOCF	ORCA2	Pacific	float	offline	within WOA05 10 μmol/l O_2 at 200 m	200 m	28 runs, 1958-1977, 1959-1978, .. 1985-2004
ORCA2-AFLVOCF	ORCA2	Atlantic	float	offline	within WOA05 80 μmol/l O_2 at 200 m	196.7 m - 240 m	28 runs, 1958-1977, 1959-1978, .. 1985-2004

Continued on next page

experiment name	model	ocean	tracer or floats	online or offline	deployment position	deployment depth	forcing period
ORCA2-PFLVOCF	ORCA2	Pacific	float	offline	within WOA05 10 μmol/l O_2 at 200 m	196.7 m - 240 m	28 runs, 1958-1977, 1959-1978, .. 1985-2004
ORCA2-ATSVOCF	ORCA2	Atlantic	tracer	offline	within WOA05 80 μmol/l O_2 at 200 m	196.7 m - 240 m	eight runs, 1978-1997, 1979-1998, .. 1985-2004
ORCA2-PTSVOCF	ORCA2	Pacific	tracer	offline	within WOA05 10 μmol/l O_2 at 200 m	196.7 m - 240 m	eight runs, 1978-1997, 1979-1998, .. 1985-2004
ORCA2-AT0VOCN	ORCA2	Atlantic	tracer	online	within WOA05 80 μmol/l O_2 at 200 m	196.7 m - 240 m	1985-2004
ORCA2-PT0VOCN	ORCA2	Pacific	tracer	online	within WOA05 10 μmol/l O_2 at 200 m	196.7 m - 240 m	1985-2004
H08-AF0VOCF	KCM	Atlantic	float	offline	within WOA05 80 μmol/l O_2 at 200 m	196.7 m - 240 m	80 runs, 26001-26020, 26002-26021, .. 26080-26099
H08-PF0VOCF	KCM	Pacific	float	offline	within WOA05 10 μmol/l O_2 at 200 m	196.7 m - 240 m	80 runs, 26001-26020, 26002-26021, .. 26080-26099
C08-AF0VOCF	KCM	Atlantic	float	offline	within WOA05 80 μmol/l O_2 at 200 m	196.7 m - 240 m	eight runs, 2570-2579, 2571-2580, .. 2577-2585
C08-PF0VOCF	KCM	Pacific	float	offline	within WOA05 10 μmol/l O_2 at 200 m	196.7 m - 240 m	eight runs, 2570-2579, 2571-2580, .. 2577-2585

Table 4.1: Overview over the float and tracer experiments as used in this study; their names, deployment positions, forcings, etc.

4.6.2 Why are we not using quantitative ARIANE runs?

One comment we often hear from other ARIANE-users is why we do not use trajectories only as examples for visualization of pathways and the quantitative run option for “real” analysis, as commonly done. Using the quantitative runs instead of qualitative runs has many advantages. For example, in qualitative runs every trajectory has to be saved individually which means that approximately 30.000 trajectories can be calculated for 20 years when saving a position every 5 days without producing files that are too large for default netcdf, ferret and matlab to handle. Quantitative runs allow for simultaneous calculation of many more trajectories, thereby reducing the number of runs that have to be made. Also, in quantitative runs floats are automatically deployed in a transport-weighted way over a vertical section. This is very helpful in accurately accounting for the fate of the water that flows through this section. However, this method cannot be applied in case of OMZs, where floats are deployed on a horizontal plane and no mean flow exists. Trajectories of floats deployed in the OMZ show that some floats reside for several years horizontally in the area of their deployment. Vertically, those floats typically oscillate with the seasonal movement of the isotherme ±50 m around the 200 m depth in which they were deployed, before eventually leaving the OMZ. This behavior cannot easily be dealt with in quantitative runs, where the same transport might be counted twice (with no way to know about that afterwards) when new transport-weighted floats are deployed when the same water-parcel oscillates back through its original depth. In the qualitative runs used for our studies, “double-counting” of the same water parcel can potentially occur, too, but this is of no relevance since transports are not considered. Also, the criterion for when the investigation of each trajectory ends is defined using a density criterion and thus at each timestep depends on the local temperature and salinity profiles which was not yet implemented in ARIANE and much easier to realize in qualitative runs.

4.6.3 Figures

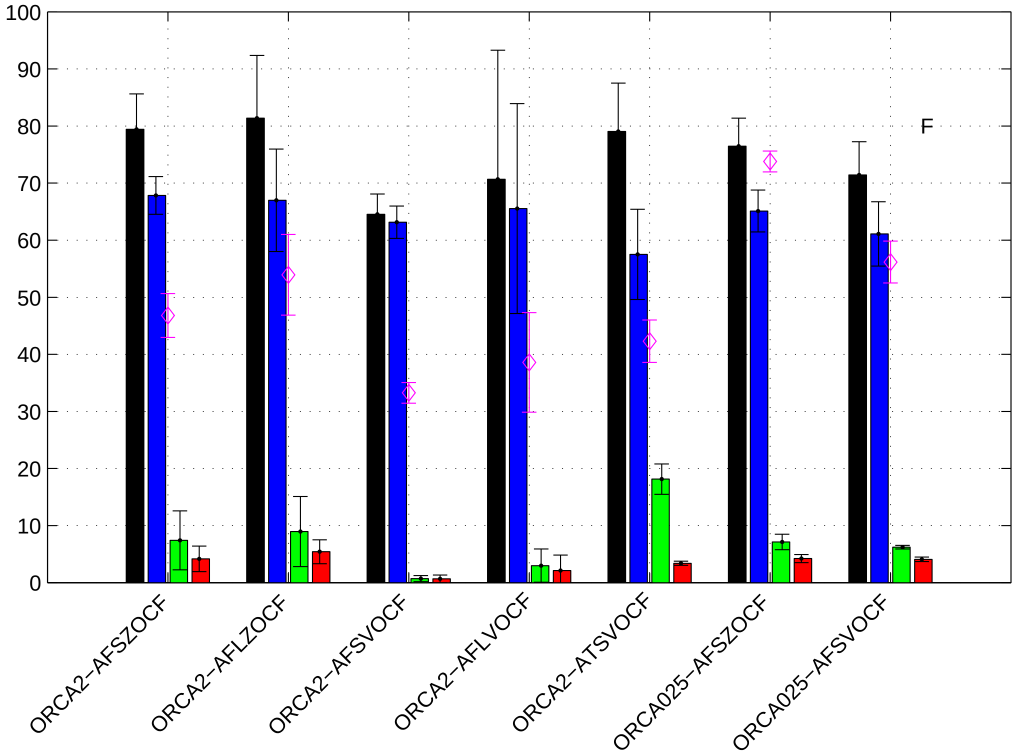

Figure 4.24: Atlantic: Enlarged version of Figure 4.16, Panel F: Magenta diamonds: Average amount of floats/tracer having reached the mixed layer after 20 years of run with errorbars showing the standard deviation (Compare 4.11). Contribution of the different boxes to the total amount of floats/tracer having reached the mixed layer within 20 years; relative to the values shown in magenta as 100 %: Black bars denote the total that can be explained by the three boxes, blue bars show the contribution of the southern box, green bars of the equatorial box and red bars of the northern box. (Note: While the magenta diamonds and errorbars denote the percentage relative to the total number of floats deployed in the OMZ, the colored bars show the percentage relative to the value of the magenta diamond as 100 %.)

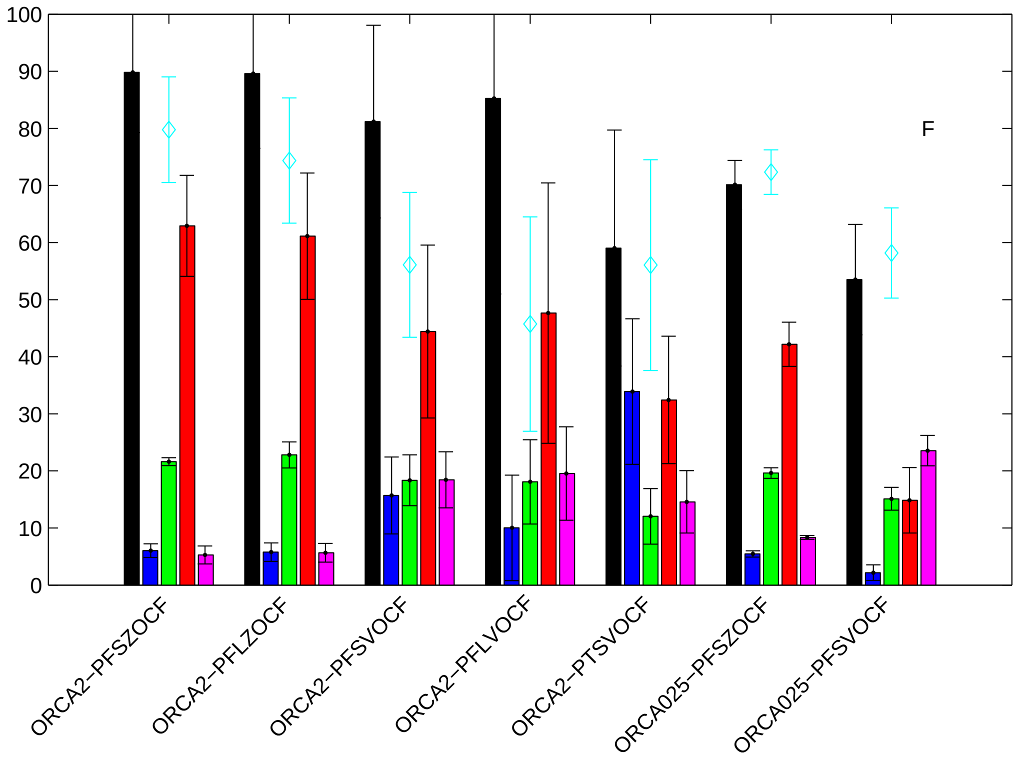

Figure 4.25: Pacific: Enlarged version of Figure 4.18,Panel F: Cyan diamonds: Average amount of floats/tracer having reached the mixed layer after 20 years of run, with errorbars showing the standard deviation. Contribution of the different boxes to the total amount of floats/tracer having reached the mixed layer within 20 years; 100 % are the values shown in magenta: Black bars denote the total that can be explained by the four boxes, blue bars show the contribution of the southern box, green bars of the equatorial box, red bars of the northern box and magenta of the Costa Rica Dome box. (Note: While the cyan diamonds and errorbars denote the percentage relative to the total number of floats deployed in the OMZ, the colored bars show the percentage relative to the value of the cyan diamond as 100 %.)

4.7 Acknowledgments

I am grateful to Julia Getzlaff for providing the 1-D diffusion model. Thanks to Arne Biastoch for ORCA025 data, Olaf Duteil for ORCA2 data and help with ORCA2 offline tracer runs, Wonsun Park for the coupled KCM runs and helpful discussions, and the ARIANE-team for providing the offline trajectory calculation routine. Funding of MSG through the DFG-funded SFB 754 is acknowledged.

Chapter 5

Conclusions and outlook

Numerical ocean models are a tool that can help to understand oceanic processes and their interaction with biogeochemistry and the atmosphere on different temporal and spatial scales. A better understanding of climate model behavior is crucial, as model predictions are used to formulate international protocols intended to mitigate the severity of climate change and its impacts, e.g. on the global ecology and economy. In order to improve numerical models of the climate system, this thesis concentrates on the parameterization of a small-scale process in an ocean model and its impact on simulated upper-ocean properties, as well as on the influence of horizontal grid resolution on the representation of the connection between tropical oxygen minimum zones and the surface ocean.

In Chapter 2, the simulated impact of double-diffusive mixing on the physical and biogeochemical upper-ocean properties was discussed. Using a global ocean model, coupled to a simple NPZD-type biogeochemistry model, two different parameterizations of double-diffusive mixing, LMD94 and ZSH98 (Large et al. [1994] and Zhang et al. [1998], respectively), are investigated.

The results of this study suggest that double diffusion only has a limited effect on physical upper ocean properties. Changes in heat fluxes between double-diffusive runs and the control run turn out to be more than an order of magnitude smaller than fluxes associated with the current anthropogenic greenhouse effect. The biggest impact of including double diffusive mixing was found for the marine biology and biogeochemistry. Primary production shows regional enhancements by some 100 % over large areas of the oligotrophic subtropical gyres. Global enhancement of primary production is much smaller, about 1 % for LMD94 and 3 % for ZSH98, because the large relative enhancement mostly takes place in low-productivity regions. Simulated CO_2 uptake of the ocean is enhanced by about $0.14\,\mathrm{Gt\,C\,yr^{-1}}$ in the double diffusive runs, comparable to $7\,\%$ of the anthropogenic CO_2 emission.

Applied to temperature and salinity profiles measured during the North Atlantic Tracer Release Experiment and comparing root-mean-square differences, ZSH98 better represents diffusivities measured during the same experiment. Results of the model run including the ZSH98 parameterization almost always differ more from the control run than results of the model run including LMD94. Still, results of this modeling study do not allow for a definite conclusion about which parameterizations, if any of the two, is more realistic than a complete omission of double-diffusive mixing. Changes to physical fields are of the same order of magnitude as uncertainties connected to those fields. Changes in modelled biogeochemical fields, although larger than in physical fields, are still small compared to the uncertainties connected with the observed fields as well as with the biogeochemical model, and hence do not allow for a recommendation of which mixing parameterization should be used.

The main result of Chapter 2 is that mechanistic understanding of mixing processes and their parameterizations in ocean circulation models are not yet satisfactory. A better understanding of mixing processes (including, but not limited to, double diffusion) is important in order for models to accurately simulate real-world behavior – including that caused by anthropogenically-driven climate change. Further work could focus on including double-diffusive mixing in other mixing parameterizations to investigate if the changes found in this study can be reproduced. Then, it would be interesting to include double-diffusive mixing in climate model runs to determine if it has the potential of changing the mean state of the model, for example in terms of the strength of meridional overturning. And since global warming is likely to lead to changes in the proportion of "ordinary" and double-diffusive mixing, including double-diffusive mixing in global warming climate model simulations would be the next step.

Chapter 3 and Chapter 4 focus on the connection between oxygen minimum zones (OMZs) and the surface ocean in order to determine how quickly feedback processes between changes in OMZ nutrient ratios and the upper-ocean ecosystem can occur. In Chapter 3, the contribution of OMZ waters to the coastal upwelling off Mauritania in Northwest Africa is investigated in a regional study. Two main supply routes of waters upwelling off Mauritania have been identified by calculating trajectories of e-floats in the model, agreeing well with observations. First the southern pathway, supplying up to 50 % of the water upwelled in winter, and about 30 % in summer, originates in the equatorial zonal current system, namely the NEUC, the nNECC and a more northerly band of the equatorial zonal current system. Second, the northern pathway supplies 35 % of the upwelled water in spring compared to 25 % during the rest of the year. Considering only water that stays below the mixed layer between crossing 23°W and reaching the upwelling, the northern pathway is almost non-existent. Therefore, the main factor influencing biogeochemical properties in the surface waters of the upwelling region is the southern pathway and not the OMZ: The connection of the upwelling with the OMZ is very weak. Only about 1 % of the upwelling waters originate in the OMZ. On the other hand, water leaving the OMZ tends to reach the mixed layer mostly in the coastal upwelling rather than further offshore on annual to decadal time scales. According to our model, about 10 % of the tracer labeling the OMZ waters reach the surface mixed layer on a time scale of 6 years - twice as much as estimated with trajectories of e-floats. However, the observed increase of N_2O concentrations towards the Mauritanian upwelling regions cannot simply be explained by a direct advective route between the OMZ and the upwelling. Instead, the link between OMZ and upwelling is largely mediated by diapycnal mixing processes that, in our model, are sub-grid scale. The strength of diapycnal mixing in the area is not well known and needs to be better constrained in order to obtain robust estimates of the leakage of OMZ waters into the upwelling off Mauritania.

In Chapter 4, the discussion of Chapter 3 is resumed in the context of coarse-resolution climate models and the connection between OMZs and the surface mixed layer is investigated in models of different horizontal resolutions. Although the general flow fields of the models are similar, and especially upwelling transports agree well, the closeness of the connection between the OMZs and the mixed layer is different from the results in Chapter 3. Although a dependence of the closeness of the link on model resolution was expected and found, no systematic relationship appears to exist.

In a study of the Atlantic Ocean a large interannual variability of the connection between the OMZ and the mixed layer is found that had not been expected from the results of GEO09. However, they are found to be closely correlated with the density at which floats where deployed. In the Pacific Ocean, the interannual variability could partly be related to El Niño states. Floats that started in the OMZ during years with a strong density stratification were much less likely to reach the mixed layer within the following 20 years than floats that were started during less stratified years. Surprisingly, the connection between the Pacific OMZ and the mixed layer is much stronger in both models than that of the Atlantic OMZ at the same depth. This indicates that although the Pacific OMZ is much more intense and closer to the surface, other processes than the ventilation must determine the strength of the OMZ.

In a coupled atmosphere-ocean model, the connection between the Atlantic and Pacific OMZs and the mixed layer were investigated after it had been shown that the mean state of the present day simulations of this coupled model agrees well with the ocean only model. This analysis shows the connection to become weaker under global warming, suggesting an enhanced isolation of the OMZ from the upper ocean. This can be explained by the strength of the subtropical cells, which are much weaker under global warming.

Chapter 3 and Chapter 4 both discuss the use of e-floats and tracer as a proxy for the connection of OMZs and the upper ocean. From these chapters, recommendations on the use of both floats and tracer experiments can be made. For example it is important to use continuous velocity fields to force low-resolution float calculations, rather than repeatedly use short periods. For tracer calculations, destroying tracer at the surface provides quasi-lagrangian information on when how much tracer reaches the surface in which region. Additionally, by destroying tracer at the surface the characteristics of the nitrate-to-phosphate anomaly that is being modelled is better captured than with a conservative tracer.

The results of Chapter 4 depend on the assumption that WOA05 OMZs are a good approximation of the position and extent in the different models, even under the global warming scenario. This assumption needs to be tested in future work. For example running the model with age-tracer and biogeochemistry including oxygen could provide means to better estimate where in those models the least-ventilated regions and the OMZs are located. Those next studies should also consider deploying floats and tracer continuously in time in order to avoid aliasing.

In Chapter 4 the impression arises that numerically induced mixing in the eddy-permitting model is too high, or at least higher than in the high- and coarse-resolution model. This needs to be tested by repeating the tracer analyses of the coarse-resolution model in the eddy-permitting model.

In summary, future work motivated by this study should address questions related to mixing processes and their representation in ocean models. First of all, a better knowledge of mixing actually taking place in the ocean has to be obtained. Both values of mixing coefficients as well as understanding of processes are important. Parameterizations of mixing processes can then be improved and validated against measured values. Also, implicit mixing spuriously introduced by advection schemes and other numerical issues has to be considered and accounted for. Then, the newly obtained mixing parameterizations have to be tested over a range of model resolutions, and can help to improve future model simulations.

Author contributions

Chapter 2 has been published (Reproduced by permission of American Geophysical Union):

Glessmer, M. S., A. Oschlies, and A. Yool (2008), Simulated impact of double-diffusive mixing on physical and biogeochemical upper ocean properties, J. Geophys. Res., 113, C08029, doi:10.1029/2007JC004455.

MSG wrote the manuscript, included two new parameterizations and performed experiments with the OCCAM general circulation ocean model. AY repeated the model runs with an aditionally included biological NPZD model and provided the output from those runs. Figure 2.7 was also done by AY. All other figures, calculations and analyses were performed by MSG. All of the authors contributed to discussion and the design of the research. All authors commented on the manuscript.

Chapter 3 has also been published (Author's rights without the need to obtain specific permission from Elsevier include the right to include the journal article, in full or in part, in a thesis or dissertation[1]):

Glessmer, M. S., C. Eden, and A. Oschlies (2009), Contribution of oxygen minimum zone waters to the coastal upwelling off Mauritania, Progr. Oceanogr., 83, 143–150, doi:10.1016/j.pocean.2009.07.015.

MSG wrote the manuscript and repeated, including an additional tracer, model runs provided by CE with the spFLAME model. Julia Getzlaff provided a 1D model that MSG used. All figures, calculations and analyses were performed by MSG. All of the authors contributed to discussion and the design of the research. All authors commented on the manuscript.

Chapter 4 is a manuscript in preparation. In Chapter 4 data produced by Arne Biastoch and Olaf Duteil and Wonsun Park, all IFM-GEOMAR, is used. All figures, calculations and analyses were performed by MSG. Andreas Oschlies contributed to discussions and the design of the research. This chapter is not ready for submission

---

[1] http://www.elsevier.com/wps/find/authorsview.authors/copyright am 12.08.2009

yet, because some time-consuming model runs still have to be performed. Waiting for them would disproportionately elongate MSG's time spent on obtaining her PhD, hence the analysis of those runs and the inclusion of the results into the manuscript will be performed by MSG later on as a PostDoc.

Additionally to tools described in the chapters I have used the programs Matlab and Ferret, and for Chapter 4 Ariane, Crush und cdftools.

List of Figures

1.1 Atmospheric CO_2, CH_4 and N_2O over the last 10,000 years 4
1.2 Changes in temperature, sea level and ice cover since 1961 5
1.3 Ice core data of T, CO_2, CH_4 and N_2O for the last 650 kyr 8
1.4 Schematic illustration of the global circulation system 10
1.5 Schematic of three circulation modes of the glacial Atlantic 11
1.6 Climate record for the second half of the last glacial 12
1.7 Schematic illustration of the biological pump 14
1.8 Schematic illustration of OMZs 16
1.9 Climatological mean dissolved oxygen concentrations 17
1.10 Dissolved oxygen concentration versus time (1960 – 2008) 18
1.11 Schematic representation of the Atlantic subtropical cell circulation 19
1.12 Mean zonal current distribution across 35°W 21
1.13 Mean modelled zonal current distribution across 35°W 22
1.14 Potential vorticity as an indicator for OMZ positions 23
1.15 Schematic: meridional circulations in the upper and lower oceans . 26

2.1 Diffusivities as a function of the density ratio 37
2.2 Diffusivities at the NATRE site 40
2.3 Diffusivities on two sections 42
2.4 Annual cycle of diffusivities at the NATRE site 44
2.5 Simulated air-to-sea heat flux 45
2.6 Comparison of simulated production with data 47
2.7 Simulated primary production 48
2.8 Comparison of simulated nitrate with data 49
2.9 Simulated surface pCO_2 and influence of T, S and DIC 50

3.1 Comparison of modelled and satellite SSTs 66
3.2 Comparison of modelled upwelling with Ekman theory 68

3.3 Origin of upwelling waters at 23°W 70
3.4 Floats and tracer reaching the mixed layer 72
3.5 Horizontally averaged float distribution 73

4.1 Velocity and density section 23°W 80
4.2 Velocity and density section 4°E 81
4.3 Velocity and density section 12°S 82
4.4 Atlantic: Comparison with FLAME 84
4.5 Atlantic: Upwelling transport 85
4.6 Comparison of conservative and destroyed tracer - Atlantic 90
4.7 Comparison of conservative and destroyed tracer - Pacific 91
4.8 Floats reaching the mixed layer under different forcings 95
4.9 Density jumps caused by different forcing strategies 96
4.10 Atlantic: transit times to mixed layer 98
4.11 Atlantic: Floats reaching the mixed layer in ORCA025 and ORCA2 100
4.12 Interannual variability of density at the Atlantic OMZ 101
4.13 Sketch of a mechanism explaining behavior of tracer 103
4.14 Temporal evolution of surfaced tracer and floats 104
4.15 Density at the deployment region vs connection to OMZ 105
4.16 Atlantic: pathways and areas where the mixed layer is reached . . . 107
4.17 Pacific: Floats reaching the mixed layer 110
4.18 Pacific: Pathways and areas where the mixed layer is reached 111
4.19 Horizontally integrated float and tracer concentrations 113
4.20 Interannual variability of the connection in coupled model 115
4.21 Connection under global warming scenario 116
4.22 Comparison of float and tracer estimates 118
4.23 Naming convention float and tracer runs 120
4.24 Enlarged version of Figure 4.16, Panel F 125
4.25 Enlarged version of Figure 4.18, Panel F 126

List of Tables

4.1 Overview over the float and tracer experiments 123

Bibliography

Y. Aksenov. The sea ice-ocean global coupled ARCICE project report part 1: description of dynamical-thermodynamical sea ice model. *SOC Research & Consultancy Report 103*, 2002.

I. Allison, N. Bindoff, R. Bindschadler, P. Cox, N. de Noblet, M. England, J. Francis, N. Gruber, A. Haywood, D. Karoly, G. Kaser, C. L. Quéré, T. Lenton, M. Mann, B. McNeil, A. Pitman, S. Rahmstorf, E. Rignot, H. Schellnhuber, S. Schneider, S. Sherwood, R. Somerville, K. Steffen, E. Steig, M. Visbeck, and A. Weaver. The Copenhagen diagnosis, 2009: Updating the world on the latest climate science. *The University of New South Wales Climate Change Research Centre (CCRC), Sydney, Australia, 60 pages*, 2009.

M. A. Altabet. Nitrogen isotopic evidence for micronutrient control of fractional NO_3^- utilization in the equatorial Pacific. *Limnology and Oceanography*, 46(2): 368 – 380, 2001.

A. Bakun. Global climate change and intensification of coastal ocean upwelling. *Science*, 247:198 – 201, 1990.

A. Bakun and C. S. Nelson. The seasonal cycle of wind-stress curl in subtropical eastern boundary current regions. *Journal of Physical Oceanography*, 21:1815 – 1834, 1991.

H. W. Bange, S. W. Naqvi, and L. A. Codispoti. The nitrogen cycle in the Arabian Sea. *Progress in Oceanography*, 65:145 – 158, 2005.

M. J. Behrenfeld and P. G. Falkowski. Photosynthetic rates derived from satellite-based chlorophyll concentration. *Limnology and Oceanography*, 42:1 – 20, 1997.

M. J. Benton and R. J. Twitchett. How to kill (almost) all life: the end-Permian extinction event. *Trends in Ecology & Evolution*, 18:358–365, 2003.

F. Birol and R. Morrow. Source of the baroclinic waves in the southeast Indian Ocean. *Journal of Geophysical Research*, 106:9145 – 9160, 2001.

B. Blanke and S. Raynaud. Kinematics of the Pacific Equatorial Undercurrent: an Eulerian and Lagrangian approach from GCM results. *Journal pf Physical Oceanography*, 27:1038 – 1053, 1997.

C. W. Böning and M. D. Cox. Particle dispersion and mixing of conservative properties in an eddy-resolving model. *Journal of Physical Oceanography*, 18:320 – 338, 1988.

L. Bopp, C. LeQuéré, M. Heimann, A. C. Manning, and P. Monfray. Climate-induced oceanic oxygen fluxes: Implications for the contemporary carbon budget. *Global Biogeochemical Cycles*, 16(2), 2002.

P. Brandt, V. Hormann, B. Bourls, J. Fischer, F. A. Schott, L. Stramma, and M. Dengler. Oxygen tongues and zonal currents in the equatorial Atlantic. *Journal of Geophysical Research*, 113(C04012), 2008.

W. S. Broecker. The biggest chill. *Natural History*, 96:74 – 82, 1987.

W. S. Broecker, D. M. Peteet, and D. Rind. Does the ocean-atmosphere system have more than one stable mode of operation? *Nature*, 315:21 – 26, 1985.

K. W. Bruland, E. L. Rue, G. J. Smith, and G. R. DiTullio. Iron, macronutrients and diatom blooms in the Peru upwelling regime: brown and blue waters of Peru. *Marine Chemistry*, 2-4:81–103, 2005.

K. Bryan. Potential vorticity in models of the ocean circulation. *Quart. J. Roy. Meteor. Soc.*, 113:713 – 734, 1987.

D. E. Canfield. Models of oxic respiration, denitrification and sulfate reduction in zones of coastal upwelling. *Geochimica*, 70:5753–5765, 2006.

D. E. Canfield and B. Thamdrup. Towards a consistent classification scheme for geochemical environments, or, why we wish the term 'suboxic' would go away. *Geobiology*, 7:385 – 392, 2009.

A. Capotondi, M. A. Alexander, C. Deser, and A. Miller. Low-frequency pycnocline variability in the northeast pacific. *Journal of Physical Oceanography*, 35(8):1403 – 1420, 2005.

P. U. Clark, N. G. Pisias, T. F. Stocker, and A. J. Weaver. The role of the thermohaline circulation in abrupt climate change. *NATURE*, 415:863 – 869, 2002.

L. A. Codispoti and J. P. Christensen. Nitrification, denitrification and nitrous oxide cycling in the eastern tropical South Pacific Ocean. *Mar. Chem.*, 16:277 – 300, 1985.

L. A. Codispoti and F. A. Richards. An analysis of the horizontal regime of denitrification in the eastern tropical North Pacific. *Limnol. Oceanogr.*, 21:379 – 388, 1976.

L. A. Codispoti, J. A. Brandes, J. P. Christensen, A. H. Devol, S. A. Naqvi, H. W. Paerl, and T. Yoshinari. The oceanic fixed nitrogen and nitrous oxide budgets: Moving targets as we enter the Anthropocene? *Scientia Marina*, 65(S2), 2001.

M. E. Conkright, R. A. Locarnini, H. E. Garcia, T. D. O'Brien, T. P. Boyer, C. Stephens, and J. I. Antonov. World Ocean Atlas 2001: Objective analyses, data statistics, and figures, CD-ROM documentation. *National Oceanographic Data Center, Silver Spring, MD, USA, Internal Report No. 17*, page 17, 2002.

A. C. Coward and B. A. de Cuevas. The OCCAM 66 level model: physics, initial conditions and external forcing. *Southampton Oceanography Centre Internal Report*, 99:58 pp, 2005.

G. Danabasoglu, W. G. Large, J. J. Tribbia, P. R. Gent, B. P. Briegleb, and J. C. McWilliams. Diurnal coupling in the tropical oceans of CCSM3. *Journal of Climate*, Special Issue, 2006.

C. Deutsch, N. Gruber, R. M. Key, J. L. Sarmiento, and A. Ganachaud. Denitrification and N_2 fixation in the Pacific Ocean. *Global Biogeochemical Cycles*, 15: 483 – 506, 2001.

C. Deutsch, J. L. Sarmiento, D. M. Sigman, N. Gruber, and J. P. Dunne. Spatial coupling of nitrogen inputs and losses in the ocean. *Nature*, 445:163 – 167, 2007.

E. P. Dever, C. E. Dorman, and J. L. Largier. Surface boundary-layer variability off Northern California, USA, during upwelling. *Deep-Sea Research II*, 53:2887 – 2905, 2006.

H. Dietze, A. Oschlies, and P. Kähler. Internal-wave-induced and double-diffusive nutrient fluxes to the nutrient-consuming surface layer in the oligotrophic subtropical North Atlantic. *Ocean Dynamics*, 54:1 – 7, 2004.

E. DiLorenzo, A. J. Miller, N. Schneider, and J. C. McWilliams. The warming of the california current system: Dynamics and ecosystem implications. *Journal of Physical Oceanography*, 35:336 – 362, 2005.

K. Döös. Interocean exchange of water masses. *Journal of Geophysical Research*, 100(C7):13499 – 13514, 1995.

C. Eden. Mid-depth equatorial tracer tongues. *Journal of Geophysical Research*, 111(C12):C12025, 2006.

C. Eden and A. Oschlies. Adiabatic reduction of circulation-related CO_2 air-sea flux biases in a North Atlantic carbon-cycle model. *Global Biogeochemical Cycles*, 20, 2006.

A. Elmoussaoui, M. Arhan, and A. M. Treguier. Model-inferred upper ocean circulation in the eastern tropics of the North Atlantic. *Oceanographic Research Papers*, 52(7):1093 – 1120, 2005.

K. N. Fedorov. *Layer thickness and effective diffusivities in the 'diffusive' thermohaline convection in the ocean.* Elsevier Oceanography Series, 1988.

K. J. Flynn. Castles built on sand: dysfunctionality in plankton models and the inadequacy of dialogue between biologists ans modellers. *Journal of Plankton Research*, 27(12):1205 – 1210, 2005.

I. Y. Fung, S. K. Meyn, I. Tegen, S. C. Doney, J. G. John, and J. K. B. Bishop. Iron supply and demand in the upper ocean. *Global Biogeochemical Cycles*, 14: 281–296, 2000.

A. Ganachaud and C. Wunsch. Improved estimates of global ocean circulation, heat transport and mixing from hydrographic data. *NATURE*, 408:453 – 240, 2000.

A. C. N. Garabato, K. L. Polzin, B. A. King, K. J. Heywood, and M. Visbeck. Widespread intense turbulent mixing in the Southern Ocean. *Science*, 303:210 – 213, 2004.

H. E. Garcia, R. A. Locarnini, T. P. Boyer, and J. I. Antonov. Dissolved oxygen, apparent oxygen utilization, and oxygen saturation. In S. Levitus, editor, *World Ocean Atlas 2005, Volume 3*, page 342. NOAA Atlas NESDIS 63, U.S. Government Printing Office, Washington, D.C., 2006.

A. E. Gargett. Ocean turbulence. *Annual Review of Fluid Mechanics*, 21:419 – 451, 1989.

P. Gaspar, Y. Gregoris, and J.-M. Lefevre. A simple eddy kinetic energy model for simulations of the oceanic vertical mixing: tests at station PAPA and long-term upper ocean study site. *Journal of Geophysical Research*, 95:16179 – 16193, 1990.

P. R. Gent and J. C. McWilliams. Isopycnal mixing in circulation models. *Journal of Physical Oceanography*, 20:150 – 155, 1990.

J. Getzlaff. *Diagnostics of diapycnal diffusion in z-level ocean models*. PhD thesis, University of Southampton, Faculty of Engineering Science and Mathematics, School of Ocean and Earth Sciences, 2008.

M. S. Glessmer, C. Eden, and A. Oschlies. Contribution of oxygen minimum zone waters to the coastal upwelling off Mauretania. *Progress in Oceanography*, 83:143 – 150, 2009.

M. C. Gregg. Diapycnal mixing in the thermocline: A review. *Journal of Geophysical Research*, 92:5249 – 5286, 1987.

S. M. Griffies, C. Böning, F. O. Bryan, E. P. Chassignet, R. Gerdes, H. Hasumi, A. Hirst, A.-M. Treguier, and D. Webb. Developments in ocean climate modelling. *Ocean Modelling*, 2:123 – 192, 2000a.

S. M. Griffies, R. C. Pacanowski, and R. W. Hallberg. Spurious diapycnal mixing associated with advection in a z-coordinate ocean model. *Monthly Weather Review*, 128:538 – 564, 2000b.

N. Gruber and J. L. Sarmiento. Global patterns of marine nitrogen fixation and denitrification. *Global Biogeochem. Cycles*, 11(2):235 – 266, 1997.

V. Hormann and P. Brandt. Atlantic equatorial undercurrent and associated cold tongue variability. *Journal of Geophysical Research*, 112(6):1 – 18, 2007.

P. Hughes and E. D. Burton. Stratification and water masses structure in the upwelling area off Northwest Africa in April/May 1969. *Deep-Sea Research*, 21: 611 – 628, 1974.

E. C. Hunke and J. K. Dukowicz. An elastic-viscous-plastic model for sea ice dynamics. *Journal of Physical Oceanography*, 27:1849 – 1867, 1997.

H. E. Huppert. On the stability of a series of double-diffusive layers. *Deep-Sea Research*, 18:1005 – 1021, 1971.

H. E. Hurlburt and P. J. Hogan. Impact of 1/8° to 1/64° resolution on Gulf Stream model-data comparisons in basin-scale subtropical Atlantic Ocean models. *Dynamics of Atmospheres and Oceans*, 32:283 – 329, 2000.

S. Hüttl-Kabus and C. W. Böning. Pathways and variability of the off-equatorial undercurrents in the atlantic ocean. *Journal of Geophysical Research*, 111, 2008.

IPCC. Climate Change 2007: The Physical Science Basis. Contribution of Working Group I to the Fourth Assessment Report of the Intergovernmental Panel on Climate Change [Solomon, S., D. Qin, M. Manning, Z. Chen, M. Marquis, K.B. Averyt, M. Tignor and H.L. Miller (eds.)]. *Cambridge University Press, Cambridge, United Kingdom and New York, NY, USA*, 2007a.

IPCC. Summary for policymakers. In: Climate Change 2007: The Physical Science Basis. Contribution of Working Group I to the Fourth Assessment Report of the Intergovernmental Panel on Climate Change [Solomon, S., D. Qin, M. Manning, Z. Chen, M. Marquis, K.B. Averyt, M. Tignor and H.L. Miller (eds.)]. *Cambridge University Press, Cambridge, United Kingdom and New York, NY, USA*, 2007b.

E. Jansen, J. Overpeck, K. Briffa, J.-C. Duplessy, F. Joos, V. Masson-Delmotte, B. O.-B. D. Olago, W. Peltier, S. Rahmstorf, R. Ramesh, D. Raynaud, D. Rind, O. Solomina, R. Villalba, and D. Zhang. Palaeoclimate. In: Climate Change 2007: The Physical Science Basis. Contribution of Working Group I to the Fourth Assessment Report of the Intergovernmental Panel on Climate Change [Solomon, S., D. Qin, M. Manning, Z. Chen, M. Marquis, K.B. Averyt, M. Tignor and H.L. Miller (eds.)]. *Cambridge University Press, Cambridge, United Kingdom and New York, NY, USA*, 2007.

W. S. Jevons. On the cirrus form of clouds. *Philosophical magazine & Journal of Science*, 14(90):22 – 35, 1857.

G. C. Johnson. Generation and initial evolution of a mode water θ-S anomaly. *Journal of Physical Oceanography*, 36:739 – 751, 2006.

G. C. Johnson and K. A. Kearney. Ocean climate change fingerprints attenuated by salt fingering? *Geophysical Research Letters*, 36, 2009.

C. E. Jones and H. C. Jenkins. Seawater strontium isotopes, oceanic anoxic events, and seafloor hydrothermal activity in the Jurassic and Cretaceous. *Am. J. Sci.*, 301:112 – 149, 2001.

P. G. Jones and A. R. Folkard. Chemical oceanographic observations off the coast of north-west Africa, with special reference to the process off upwelling. *Rapp. P.-v. Run. int. Explor. Mer.*, 159:37 – 60, 1970.

J. Karstensen, L. Stramma, and M. Visbeck. Oxygen minimum zones in the eastern tropical Atlantic and Pacific oceans. *Progress in Oceanography*, 77:331 – 350, 2008.

D. E. Kelley. Effective diffusivities within oceanic thermohaline staircases. *Journal of Geophysical Research*, 89(C6):10484 – 10488, 1984.

D. E. Kelley. Fluxes through diffusive staircases: A new formulation. *Journal of Geophysical Research*, 95(C3):3365 – 3371, 1990.

D. E. Kelley, H. J. S. Fernando, A. E. Gargett, J. Tanny, and E. Özsoy. The diffusive regime of double-diffusive convection. *Progress in Oceanography*, 56:461 – 481, 2003.

R. M. Key, A. Kozyr, C. L. Sabine, K. Lee, R. Wanninkhof, J. L. Bullister, R. A. Feely, F. J. Millero, C. Mordy, and T.-H. Peng. A global ocean carbon climatology: Results from Global Data Analysis Project (GLODAP). *Global Biogeochemical Cycles*, 18:1 – 23, 2004.

A. Kock, A. Freing, S. Gebhardt, M. S. Glessmer, and H. W. Bange. Nitrous oxide distribution in the Eastern Tropical North Atlantic Ocean. *Poster at the Eastern Boundary Upwelling Ecosystems Symposium, 2.-6.6.2008, Las Palmas, Spain*, 2008a.

A. Kock, S. Gebhardt, and H. W. Bange. Methane emissions from the upwelling area off Mauritania (NW Africa). *Biogeosciences*, 5:297–315, 2008b.

J. Kröger, A. J. Busalacchi, J. Ballabrera-Poy, and P. Malanotte-Rizzoli. Decadal variability of shallow cells and equatorial sea surface temperature in a numerical model of the atlantic. *Journal of Geophysical Research*, 110(C12003), 2005.

E. Kunze and J. M. Toole. Tidally driven vorticity, diurnal shear, and turbulence atop fieberling seamount. *Journal of Physical Oceanography*, 27:2663 – 2692, 1997.

M. M. M. Kuypers, G. Lavik, , D. Woebken, , M. Schmid, B. M. Fuchs, R. Amann, B. B. Jørgensen, and M. S. M. Jetten. Massive nitrogen loss from the Benguela upwelling system through anaerobic ammonium oxidation. *Proceedings of the National Academy of Sciences*, 102(18):6478 – 6483, 2005.

W. Large and S. Yeager. Diurnal to decadal global forcing for ocean and sea-ice models: the datasets and flux climatologies. *NCAR technical note*, NCAR/TN-460+STR, CGD division of the National Center for Atmospheric Research. Available on the GFDL CORE web site., 2004.

W. G. Large, J. C. McWilliams, and S. C. Doney. Oceanic vertical mixing: a review and a model with a nonlocal boundary layer parameterization. *Reviews of Geophysics*, 32(4):363 – 403, 1994.

W. G. Large, G. Danabasoglu, and S. C. Doney. Sensitivity to surface forcing and boundary layer mixing in a global ocean model: annual-mean climatology. *Journal of Physical Oceanography*, 27:2418 – 2446, 1997.

J. R. Ledwell, A. J. Watson, and C. S. Law. Evidence for slow mixing across the pycnocline from an open-ocean tracer-release experiment. *Nature*, 364:701 – 703, 1993.

S. Levitus. World Ocean Atlas 1994. *CD-ROM data set documentation, NODC Ocean Climate Laboratory, Washington, DC, Informal Report No. 13*, 1994.

J. R. Luyten, J. Pedlosky, and H. Stommel. The ventilated thermocline. *Journal of Physical Oceanography*, 13:292 – 309, 1983.

G. Madec. NEMO ocean engine. Note du pole de modélisation. *27, Institut Pierre-Simon Laplace, 193 pp.*, 2008.

P. Malanotte-Rizzoli, K. Hedstromb, H. Arangob, and D. B. Haidvogel. Water mass pathways between the subtropical and tropical ocean in a climatological simulation of the North Atlantic ocean circulation. *Dynamics of Atmospheres and Oceans*, 32(3-4):331–371, 2000.

G. Marland, T. A. Boden, and R. J. Andres. Global, regional, and natural CO_2 emissions. in Trends: A compendium of data on global change. *Carbon Dioxide Information Analysis Center, Oak Ridge National Laboratory, U. S. Department of Energy, Oak Ridge, Tenn. USA*, 2007.

G. O. Marmorino and D. R. Caldwell. Heat and salt transport through a diffusive thermohaline interface. *Deep-Sea Research*, 23:59 – 67, 1978.

R. J. Matear and A. C. Hirst. Long-term changes in dissolved oxygen concentrations in the ocean caused by protracted global warming. *Global Biogeochemical Cycles*, 17, 2003.

J. P. McCreary and P. Lu. Interaction between the subtropical and equatorial ocean circulations: The subtropical cell. *Journal of Physical Oceanography*, 24: 466 – 497, 1994.

M. J. McPhaden and D. Zhang. Slowdown of the meridional overturning circulation in the upper Pacific Ocean. *Nature*, 415:603 – 608, 2002.

K. J. Meissner, E. D. Galbraith, and C. Völker. Denitrification under glacial and interglacial conditions: a physical approach. *Paleoceanography*, 20, 2005.

J. Merryfield, G. Holloway, and A. E. Gargett. A global ocean model with double-diffusive mixing. *Journal of Physical Oceanography*, 29(6):1124 – 1142, 1999.

W. G. Metcalf and M. C. Stalcup. Origin of the Atlantic Equatorial Undercurrent. *Journal of Geophysical Research*, 72(20):4959 – 4975, 1967.

J. F. B. Mitchell. The 'greenhouse effect' and climate change. *Reviews of Geophysic*, 27(1):115 – 139, 1989.

E. Mittelstaedt. The upwelling area off Northwest Africa–a description of phenomena related to coastal upwelling. *Progress in Oceanography*, 12:307 – 331, 1983.

E. Mittelstaedt. The ocean boundary along the northwest African coast. Circulation and oceanographic properties at the sea surface. *Progress in Oceanography*, 26: 307 – 355, 1991.

J. M. Molines, B. Barnier, T. Penduff, L. Brodeau, A. M. Treguier, S. Theetten, and G. Madec. Definition of the interannual experiment ORCA025-G70, 1958-2004. *LEGI report, LEGIDRA-2-11-2006, available at http://www.ifremer.fr/lpo/drakkar*, 2006.

W. H. Munk. Abyssal recipes. *Deep-Sea Research*, 13:707 – 730, 1966.

W. H. Munk and C. Wunsch. Abyssal recipes II: energetics of tidal and wind mixing. *Deep-Sea Research*, 45:1977 – 2010, 1998.

R. Najjar and J. C. Orr. Biotic-howto. *Internal OCMIP Report*, 1999.

J. C. Orr, R. Najjar, C. L. Sabine, and F. Joos. Abiotic-howto. *Internal OCMIP report*, 1999.

A. Oschlies. Model-derived estimates of new production: New results point towards lower values. *Deep-Sea Research*, 48:2173 – 2197, 2001.

A. Oschlies. Nutrient supply to the surface waters of the North Atlantic: A model study. *Journal of Geophysical Research*, 107:–, 2002.

A. Oschlies and P. Kähler. Biotic contribution to air-sea fluxes of CO_2 and O_2 and its relation to new production, export production, and net community production. *Global Biogeochemical Cycles*, 18:–, 2004.

A. Oschlies, H. Dietze, and P. Kähler. Salt-finger driven enhancement of upper ocean nutrient supply. *Geophysical Research Letters*, 30(23):2204, 2003.

A. Oschlies, K. G. Schulz, U. Riebesell, and A. Schmittner. Simulated 21st century's increase in oceanic suboxia by CO_2-enhanced biotic carbon export. *Global Biogeochemical Cycles*, 22, 2008.

S. Ould-Dedah, W. J. Wiseman Jr., and R. F. Shaw. Spatial and temporal trends of sea surface temperature in the northwest African region. *Oceanologica Acta*, 22:265 – 279, 1999.

R. C. Pacanowski. MOM 2 documentation, user's guide and reference manual. *Technical Report, GFDL Ocean Group, GFDL, Princeton, USA*, 1995.

W. Park, N. Keenlyside, M. Latif, A. Ströh, R. Redler, E. Roeckner, and G. Madec. Tropical Pacific climate and its response to global warming in the Kiel Climate Model. *Journal of Climate*, 22(1):71–92, 2009.

M. V. Pastor, J. L. Pelegrí, A. Hernandez-Guerra, J. Font, J. Salat, and M. Emelianov. Water and nutrient fluxes off Northwest Africa. *Continental Shelf Research*, 7:915 – 936, 2008.

A. Paulmier and D. Ruiz-Pino. Oxygen Minimum Zones (OMZs) in the modern ocean. *Progress in Oceanography*, pages 2541 – 2547, 2008.

K. L. Polzin, J. M. Toole, J. R. Ledwell, and R. W. Schmitt. Spatial variability of turbulent mixing in the abyssal ocean. *Science*, 276(5309):93 – 96, 1997.

B. Rabe, F. A. Schott, and A. Köhl. Mean circulation and variability of the tropical Atlantic during 1952-2001 in the GECCO assimilation fields. *Journal of Physical Oceanography*, 38:177 – 192, 2008.

S. Rahmstorf. Ocean circulation and climate during the past 120,000 years. *Nature*, 419:207 – 214, 2002.

S. Rahmstorf. Timing of abrupt climate change: A precise clock. *Geophysical Research Letters*, 30, 2003.

S. Rahmstorf. Thermohaline ocean circulation. in: Encyclopedia of quaternary sciences, edited by s. a. elias. *Elsevier, Amsterdam 2006*, 2006.

D. A. Randall, R. A. Wood, S. Bony, R. Colman, T. Fichefet, J. Fyfe, V. Kattsov, A. Pitman, J. Shukla, J. Srinivasan, R. Stouffer, and A. Sumi. Climate models and their evaluation. In: Climate Change 2007: The Physical Science Basis. Contribution of Working Group I to the Fourth Assessment Report of the Intergovernmental Panel on Climate Change [Solomon, S., D. Qin, M. Manning, Z. Chen, M. Marquis, K.B. Averyt, M. Tignor and H.L. Miller (eds.)]. *Cambridge University Press, Cambridge, United Kingdom and New York, NY, USA*, 2007.

E. Roeckner and Coauthors. The atmospheric general circulation model ECHAM5. Part I: Model description. *Max Planck Institute for Meteorology Rep. 349, 127 pp. [Available from MPI for Meteorology, Bundesstr. 53, 20146 Hamburg, Germany.]*, 2003.

B. Rudels, G. Björk, R. D. Muench, and U. Schauer. Double-diffusive layering in the Eurasian Basin of the Arctic Ocean. *Journal of Marine Systems*, 21:3 – 27, 1999.

C. L. Sabine, R. A. Feely, N. Gruber, R. M. Key, K. Lee, J. L. Bullister, R. Wanninkhof, C. S. Wong, D. W. R. Wallace, B. Tilbrook, F. J. Millero, T.-H. Peng, A. Kozyr, T. Ono, and A. F. Rios. The oceanic sink for anthropogenic CO_2. *Science*, 305(5682):367 – 371, 2004.

J. L. Sarmiento and E. T. Sundquist. Revised budget for the oceanic uptake of anthropogenic carbon dioxide. *NATURE*, 356:589 – 593, 1992.

R. W. Schmitt. Form of the temperature-salinity relationship in the central water: Evidence for double-diffusive mixing. *Journal of Physical Oceanography*, 11:1015 – 1026, 1981.

R. W. Schmitt. C-SALT, an investigation of the thermohaline staircase in the western tropical North Atlantic. *Deep-Sea Research*, 34(10A):1655 – 1665, 1987.

R. W. Schmitt. *Mixing in a thermohaline staircase.* Elsevier Oceanography Series, 1988.

F. Schott, J. P. McCreary Jr., and G. C. Johnson. *Shallow overturning circulations of the tropical-subtropical oceans*, pages 261 – 304. AGU Geophysical Monography 'Ocean-atmosphere interactions and climate variability', 2004.

F. A. Schott, M. Dengler, P. Brandt, K. Affler, J. Fischer, B. Bourl'es, Y. Gouriou, R. L. Molinari, and M. Rhein. The zonal currents and transports at 35Â°w in the tropical Atlantic. *Geophysical Research Letters*, 30, 2003.

A. J. Semtner. A model for the thermodynamic growth of sea ice in numerical investigations of climate. *Journal of Physical Oceanography*, 6:379 – 389, 1976.

U. Siegenthaler and J. L. Sarmiento. Atmospheric carbon dioxide and the ocean. *Nature*, 365:119 – 125, 1993.

B. Sinha and A. Yool. Extension of the OCCAM 1 deg ocean general circulation model to include the biogeochemical cycles of carbon and oxygen, Part I: Technical description. *National Oceanography Centre, Southampton. Research & Consultancy Report No. 5*, pages 1 – 78, 2006.

B. M. Sloyan, G. C. Johnson, and W. S. Kessler. The pacific cold tongue: A pathway for interhemispheric exchange. *Journal of Physical Oceanography*, 33: 1027 – 1043, 2003.

W. Soon, S. Baliunas, K. Y. Kondratyev, S. B. Idso, and E. S. Posmentier. Calculating the climatic impacts of increased CO_2: The issue of model validation. *First Eurocongress on The Solar Cycle and Terrestial Climate Tenerife, Spain, September 25-30, 2000*, 2000.

L. St. Laurent and R. W. Schmitt. The contribution of salt fingers to vertical mixing in the North Atlantic Tracer Release Experiment. *Journal of Physical Oceanography*, 29:1404 – 1424, 1999.

D. P. Stevens. On open boundary conditions for three dimensional primitive equation ocean circulation models. *Geophysical Astrophysical Fluid Dynamics*, 51:103 – 133, 1990.

H. Stommel, A. B. Arons, and D. Blanchard. An oceanographic curiosity: the perpetual salt fountain. *Deep-Sea Research*, 3:152 – 153, 1956.

L. Stramma, S. Hüttl, and J. Schafstall. Water masses and currents in the upper tropical northeast Atlantic off northwest Africa. *Journal of Geophysical Research*, 110, 2005.

L. Stramma, P. Brandt, J. Schafstall, F. Schott, J. Fischer, and A. Körtzinger. Oxygen minimum zone in the North Atlantic south and east of the Cape Verde Islands. *Journal of Geophysical Research*, 1111(15), 2008a.

L. Stramma, G. C. Johnson, J. Sprintall, and V. Mohrholz. Expanding oxygen-minimum zones in the tropical oceans. *Science*, 320(655), 2008b.

L. Stramma, M. Visbeck, P. Brand, T. Tanhua, and D. Wallace. Deoxygenation in the oxygen minimum zone of the eastern tropical North Atlantic. *Geophysical Research Letters*, 36, 2009.

P. T. Strub, J. M. Mesías, V. Montecino, J. Rutliant, and S. Salinas. *Chapter 10. Coastal Ocean Circulation off Western South America*, volume 11. John Wiley & Sons, Inc., 1998.

H. U. Sverdrup. On the exploration of oxygen minima and maxima in the ocean. *Journ. du. Conseil*, Vol. XIII:163–172, 1938.

T. Takahashi, R. A. Feely, R. Weiss, R. H. Wanninkhof, D. W. Chipman, S. C. Sutherland, and T. T. Takahashi. Global air-sea flux of CO_2: an estimate based on measurements of sea-air pCO_2 difference. *Proceedings of the National Academy of Science*, 94:8292 – 8299, 1997.

T. Takahashi, S. C. Sutherland, C. Sweeney, A. Poisson, N. Metzl, B. Tilbrook, N. Bates, R. Wanninkhof, R. A. Feely, C. Sabine, J. Olafsson, and Y. Nojiri. Global CO_2 flux based on climatological surface ocean pCO_2, and seasonal biological and temperature effects. *Deep-Sea Research II*, 49:1601 – 1622, 2002.

M.-L. Timmermans, C. Garrett, and E. Carmack. The thermohaline structure and evolution of the deep waters in the Canada Basin, Arctic Ocean. *Deep-Sea Research I*, 50:1305 – 1321, 2004.

M. Tomczak and J. S. Godfrey. *Regional Oceanography: An Introduction.* 2003.

J. S. Turner. The coupled transport of salt and heat across a sharp density interface. *International Journal of Heat and Mass Transfer*, 8:759 – 767, 1965.

P. D. Williams. Modelling climate change: the role of unresolved processes. *Philosophical Transactions of the Royal Society*, 363:2931 – 2946, 2005.

W. S. Wooster, A. Bakun, and D. R. McLain. The seasonal upwelling cycle along the eastern boundary of the North Atlantic. *Journal of Marine Research*, 34:131 – 141, 1976.

C. Wunsch and R. Ferrari. Vertical mixing, energy, and the general circulation of the oceans. *Annual Review of Fluid Mechanics*, 36:281 – 314, 2004.

K. Wyrtki. The oxygen minimum in relation to ocean circulation. *Deep-Sea Research*, 9:11–23, 1962.

A. Yool and B. Sinha. Extension of the OCCAM 1 deg ocean general circulation model to include the biogeochemical cycles of carbon and oxygen, Part II: Initial experiments. *National Oceanography Centre, Southampton. Research & Consultancy Report No. 6*, 2006.

Y. You. A global ocean climatological atlas of the Turner angle: implications for double-diffusion and water-mass structure. *Deep-Sea Research I*, 49:2075 – 2093, 2002.

W. Zenk. On the temperature and salinity structure of the Mediterranean water in the Northeast Atlantic. *Deep-Sea Research*, 17:627 – 631, 1970.

J. Zhang and R. W. Schmitt. The impact of salt fingering on the thermohaline circulation under mixed boundary conditions. *Journal of Physical Oceanography*, 28:1223 – 1231, 2000.

J. Zhang, R. W. Schmitt, and R. X. Huang. Sensitivity of GFDL Modular Ocean Model to parameterization of double-diffusive processes. *Journal of Physical Oceanography*, 28:589 – 605, 1998.

J. Zhang, R. W. Schmitt, and R. X. Huang. The relative influence of diapycnal mixing and hydrologic forcing on the stability of the thermohaline circulation. *Journal of Physical Oceanography*, 29:1096 – 1108, 1999.

Acknowledgments

First and foremost, I would like to thank Andreas Oschlies for his help and encouragement, advice, guidance, seemingly eternal patience and for all the opportunities he gave and gives me to learn exciting things not strictly related to my topic.

I would also like to thank Carsten Eden for his support in running FLAME, for challenging and showing me that I can do a lot of things on my own that I did not know about before.

Many thanks to Andrew Yool, who introduced me to the world of biogeochemical modeling, and always encouraged and supported me.

I am grateful for Arne Biastoch, Olaf Duteil and Wonsun Park providing me with model data, constructive discussions and advice, and for Franziska Schwarzkopf and Erik Behrens training me to the use of all the ORCA-related diagnostics.

My special thanks to Astrid Dispert, Inger Rohr, Janine Flöter and Paul Kähler for proof-reading, and Tim Fischer for constantly doubting the validity of my results.

Many thanks to the ATA3 and JC29 captain, PI, crew and scientists for 3 amazing months at sea with plenty opportunities to look beyond the model ocean, to learn how to measure nitrous oxide and to remember why again I am in oceanography.

And I would like to thank the Seeburg crew: Thank you Julia Getzlaff, Wolfgang Koeve, Heiner Dietze, Iris Kriest and everybody else for a nice working atmosphere, constructive discussions and constant moral support. Working with you in Seeburg was a picturebook example of how a research group should function as a team.

Thank you, my family and friends, for everything!

Funding through DFG-SFB754 and BMBF-SOPRAN is gratefully acknowledged.

Erklärung

Hiermit erkläre ich, dass ich die vorliegende Dissertation - abgesehen von der Beratung durch meine akademischen Lehrer - selbstständig verfasst und keine weiteren Quellen und Hilfsmittel als die in der Einleitung angegebenen verwendet habe.
Diese Arbeit hat weder ganz, noch in Teilen, bereits an anderer Stelle einer Promotionskommission zur Erlangung des Doktorgrades vorgelegen.
Ich erkläre, dass die vorliegende Arbeit gemäß den Grundsätzen zur Sicherung guter wissenschaftlicher Praxis der Deutschen Forschungsgemeinschaft erstellt wurde.

Kiel, den 26.04.2010